METALLATED GRAPHYNE-BASED MATERIALS: SYNTHESIS, CHARACTERIZATION, PROPERTIES AND APPLICATIONS

WANG QIAOLIAN

PhD

The Hong Kong Polytechnic University

2024

The Hong Kong Polytechnic University

Department of Applied Biology and Chemical Technology

Metallated Graphyne-based Materials: Synthesis, Characterization, Properties and Applications

Wang Qiaolian

A thesis submitted in fulfillment

of the requirements for the degree of Doctor of Philosophy

December 2023

CERTIFICATE OF ORIGINALITY

I hereby declare that this thesis is my own work and that, to the best of my knowledge and belief, it reproduces no material previously published or written, nor material that has been accepted for the award of any other degree or diploma, except where due acknowledgement has been made in the text.

_____(Signed)_

WANG Qiaolian (Name of Student)

Abstract

Graphyne-based two-dimensional (2D) carbon allotropes are attracting much attention due to their extraordinary physical and chemical properties. Among them, metallated graphyne (MGY) is a kind of organometallic material that is woven from organic multi-alkyne monomer and metal ion through the bottom-up approaches, thus achieving various frameworks via monomer or metal chromophore design and integrating the advantages of both metal center and graphyne. The highly developed π-conjugated electronic structure is an excellent feature shared by MGY and graphyne, while the combination of organic ligands and metal atoms makes MGY different from graphyne. Such chemical differences enable MGY to possess unique physical properties, including a variety of components, tunable electronic structures, and high exposure to active sites. Nevertheless, the related research on their synthesis, characterizations, properties, and applications is still in its infancy. Reliable methods and comprehensive characterizations are needed to enrich the MGY family and elucidate the underlying mechanisms between their structures and properties.

To start with, a brief introduction to MGY including synthesis methodology, characterization, properties, and applications was presented in Chapter 1.

In Chapter 2, four kinds of mercury graphyne materials, **TEPB-Hg-GY**, **TEPT-Hg-GY**, **NH_2-Hg-GY**, and **F-Hg-GY** were designed and synthesized. Their chemical structures, crystal structures, and electronic structures were studied in detail with

comprehensive experiments and calculation characterizations, such as NMR, MAIDI-TOF, FTIR, PXRD, UV–Vis, UPS, XPS, TEM, SEM-EDS, and DFT calculations. Moreover, the performance of photocatalytic hydrogen peroxide (H_2O_2) production was studied and the influence of heteroatoms and active groups on their performance and their catalytic mechanism were explored.

In Chapter 3, three kinds of platinum graphyne materials, **TEPB-Pt-GY**, **TEPT-Pt-GY**, and **F-Pt-GY** were reported. Similarly, the synthesis method, structural and performance characterizations were conducted to study their chemical structures, crystal structures, and electronic structures as well as the influence of heteroatoms and active groups on their related structures and properties. What's more, their resistive random access memory (RRAM) performance was investigated.

In Chapter 4, four kinds of nickel graphyne materials, **TEPB-Ni-GY**, **TEPT-Ni-GY**, **NH_2-Ni-GY**, and **F-Ni-GY** were examined. The synthesis method, structural and performance characterizations were introduced and the influence of heteroatoms and active groups on their chemical structures, crystal structures, and electronic structures were analyzed. Finally, their performance in the application of photocatalytic carbon dioxide reduction was studied.

Acknowledgments

I would like to extend my deepest gratitude to my dedicated supervisor Prof. Wai-Yeung Wong, Raymond for his instructive advice and insightful criticism throughout my academic studies with his profound knowledge and rich research experience. His knowledge and devotion always trigger me to work harder and get better in my studies.

I would also give my hearty thanks to Dr. Linli Xu and Dr. Yang Wang for their valuable suggestions and encouragement. Their experience in the synthesis and characterization of two-dimensional carbon allotropes gave me huge support during my project.

I would like to show my gratitude to all the group members in Prof. Wong's group: Dr. Limin Zhang, Dr. Peng Tao, Dr. Miao Zhang, Dr. Zelin Sun, Dr. Govardhan Babu, Dr. Zhen Zhang, Dr. Yidi Wang, Dr. Yingying Qin, Dr. He Jiang, Dr. Jibiao Jin, Dr. Shuxin Wang, Dr. Pengfei She, Dr. Yanyan Qin, Dr. Shijie Hou, Dr. Xueqian Zhao, Dr. Dou Luo, Dr. Liyuan Le, Dr. Yuan Kang, Dr. Zishu Sun, Dr. Tao Wang, Dr. Wendong Xing, Dr. Zeling Guo, Dr. Meitong Lau, Dr. Zikang Li, Dr. Bulin Chen, Miss. Jie Zhang, Miss. Yijia Liu, Miss. Xinyu Wang, Miss. Minting Ouyang, Miss. Wenqing Wang, Miss. Huiying Liu, Miss. Xianhong Chen, Miss. Chen Zhang, Miss. Lifen Chen, Miss. Hua Su, Miss. Dan He, Mr. Yingjie Sun, Mr. Xinghao Sheng, Mr. Yuanhui, Zhong, Mr. Fangzhou Yang, Mr. Peixin Gao, Mr. Mude Zhu, and other members for their generous help and support.

Finally, I would like to show my wordless and wholehearted thanks to my parents, Mr. Xuejing Wang and Mrs. Xiaorong Wang. Their full understanding and care are always supporting me.

Thanks are also given to all the technicians for their kind technical support.

Table of Contents

List of Abbreviations and Symbols

Abbreviations

DCM	Dichloromethane
Dioxane	1,4-Dioxane
MeOH	Methanol
THF	Tetrahydrofuran
DIPA	Diisopropylamine
Et_3N	Triethylamine
DI H_2O	Deionized water
N_2	Nitrogen
K_2CO_3	Potassium carbonate
Na_2SO_4	Sodium sulphate
CuI	Copper(I) iodide
$Pd(PhCN)_2Cl_2$	Dichlorodiamminepalladium(II)
$PdCl_2(PPh_3)_2$	Dichlorobis(triphenylphosphine)palladium(II)
$[(t\text{-}Bu)_3PH]BF_4$	Tri-*tert*-butylphosphonium tetrafluoroborate
PPh_3	Triphenylphosphine
TEB	1,3,5-Triethynyl-benzene
TEPB	1,3,5-Tris-(4-ethynylphenyl)-benzene
TEPT	2,4,6-Tris-(4-ethynylphenyl)-1,3,5-triazine

TEBA	2,4,6-Triethynylbenzenamine
TEFB	1,3,5-Triethynyl-2,4,6-trifluoro-benzene
K_2PtCl_4	Potasium tetrachloroplatinate(II)
PBu_3	Tributylphosphine
Trans-$Pt(PBu_3)_2Cl_2$	*Trans*-bis(tri-n-butylphosphine)-dichloro-platinum(II)
NMR	Nuclear magnetic resonance
FTIR	Fourier-transform infrared spectroscopy
MALDI	Matrix-assisted laser desorption ionization
TEM	Transmission electron microscopy
HRTEM	High resolution transmission electron microscopy
STM	Scanning tunneling microscopy
SEM	Scanning electron microscopy
SAED	Selected area electron diffraction
EDX	Energy-dispersive X-ray spectroscopy
PXRD	Powder X-ray diffraction
UV–Vis	Ultraviolet-Visible
UV–Vis DRS	Ultraviolet-Visible diffuse reflection spectroscopy
XPS	X-ray photoelectron spectroscopy
UPS	Ultraviolet photoelectron spectroscopy
M–S	Mott Schottky

TPR	Transient photocurrent response
EIS	Electrochemical impedance spectrometry
TGA	Thermogravimetric analysis
DFT	Density functional theory
AQY	Apparent quantum yield
d	Day
h	Hour
min	Minute
s	Second
μJ	Micro Joule
W	Watt
nm	Nanometer
ppm	Parts per million
cm^{-1}	Reciprocal centimeter
Rct	Charge transfer resistance
℃	Degree Celsius
RT	Room temperature
E	Potential

Chapter 1

Introduction

Metallated graphyne-based materials

Low-dimensional (2D) materials, possessing unique chemical and physical properties, have collected a great deal of interests among researchers in recent years because of their excellent properties and intriguing applications in the field of science[1-3]. Since the first report of graphene in 2004[4], the area of the 2D materials referring to a material in which electrons can only move freely (planar motion) on the nanoscale (1-100 nm) in two dimensions was revolutionized due to their outstanding performance. Such materials include boron nitride (BN), molybdenum disulfide (MoS_2), tungsten disulfide (WS_2), black phosphorus (BP), MXene and silicene[5,6]. Recently, many efforts have been made on graphyne-based materials which are regarded as an allotrope of carbon due to their excellent characteristics[7-9]. Theoretical investigations on graphyne-based materials have been long promoting groundbreaking progress on the relevant experimental synthesis. Baughman[10] and co-workers firstly named "graphyne" with graphyne-based materials in 1987, estimating its periodic structure, mechanism and electronic characteristics. These innovation materials can be divided into graphyne, graphdiyne (GDY) and graphyne-n ($n > 2$) according to the quantity of acetylenic units. Very recently, the first large-area GDY films were prepared successfully through

chemical protocol in 2010[11]. GDY combining two types of carbon atoms of sp^2- and sp-hybridized carbon enables itself unique characteristics from graphene even though it has substantial similarity to graphene in the matter of highly π-conjugated structure, 2D hexagonal scaffold and ordered porous structure. In addition, such flat carbon networks can be constructed containing a variety of micro-structures with different acetylenic ligands, resulting in a broader diversity than 2D inorganic materials[12,13]. As best known, inorganic nanosheets can be exfoliated by using mechanical or chemical means to individual monolayer with thickness of less than 1 nm. In contrast, 2D organic framework such as metal-organic nanosheets (MONs) and covalent organic nanosheets (CONs) which are composed of ionic and molecular units through a bottom-up way are less well established[14-16]. The preparation of molecule-based nanosheets connected by carbon–carbon bond is still a challenge. On the other hand, all-carbon materials also have their own shortcomings, such as single performance and difficulty in refunctionalization because they just possess C element and C atoms are in a saturated state, which limit their performance as well as hinder their further modification.

Given this background, metal elements regarded as a new entity for functionalization can be introduced into the skeleton of GDY. Alkynyl-metal networks formed from metal-acetylide bonds: –C≡C–M–C≡C– (M = metal or metal complexes) were proposed as versatile units to form metallated graphynes (MGYs) due to their intriguing electronic properties[17,18]. With previous investigations, it is known that metal-acetylide bonds are much more stable than metal-aryl bonds with the knowledge

that the M–C bond with sp-hybridized carbon has the largest strength than that with sp^3- and sp^2-hybridized carbon due to the increased properties of carbon based hybrid orbitals[19]. Thus, this prospective network might improve the covalent character of 2D metal-organic materials. In addition, the reaction rate of dehydrohalogenative coupling between metal complex and alkyne hydrogen bond is the lowest among above three type of M–C bonds, allowing MGY to possess more thermally stable structures[20]. Moreover, density functional theory (DFT) indicates that 2D metal-acetylide networks with specific metal ions or functionalized organic ligands are magnetic organic topological insulators, which possess semi-metallic properties. The first principles DFT calculations in previous investigations have demonstrated the mechanical and thermal stability and photoelectric properties of N-, B-, P-, Al-, As-, and Ga-graphyne-based 2D networks[21]. However, related theoretical and experimental investigations on MGYs are still in their infancy. Fabrication of MGY nanosheets was proposed with the bottom-up protocol including on-surface synthesis and interface-assisted synthesis, resulting in metal-assisted MGY nanosheets and free-standing MGY nanosheets, respectively. However, less reported investigations have been made on MGYs successfully with both methods. In this context, significant features of MGYs such as electronic characters, in particular, the bonding nature of the metal–acetylide bonds in MGYs remain almost unexplored.

In light of the above, Sun[22] et al. explored the preparation of 2D –C≡C–Au–C≡C– metallic organic frameworks through high-resolution scanning tunneling

microscope (STM) via the reaction of dehydrohalogenative coupling of alkynyl bromides on Au(111) surface. Besides, Ag-bis-acetylide networks with –C≡C–Ag–C≡C– units were synthesized by Yang on Ag(111), forming a 2D organometallic scaffold[23]. However, with further annealing on Au(111), this 2D organometallic scaffold can be converted into the corresponding GDY, while this network keeps its structure complete on Ag(111) even at a rather high temperature. In addition, Zhang[24] et al. illustrated an organometallic honeycomb alkynyl-silver networks that were prepared with the gas-mediated surface method under ultrahigh vacuum conditions on Ag(111), affording a micrometer domain size. The above studies were all conducted by STM method, by which materials cannot be isolated from the substrates so that it is difficult to explore their physical and chemical properties. Xu[25] et al. reported firstly two free-standing mercurated graphyne nanosheets with chemical experimental protocol through the interface-assisted method and introduced these materials into optical devices directly. Such research is a breakthrough in the field of 2D MGYS because free-standing MGYs synthesized by this method can be easily isolated and thus can be explored thoroughly on their properties. At this stage, little research has been conducted in this field. Therefore, there are still shortcomings such as lack of diversity in chemical structures, unclear crystal structures, and ambiguous mechanisms between structure and performance.

In this project, different kinds of MGYs will be prepared by dehalogenative homocoupling reaction to enrich the category of MGYs to systematically investigative

their structures and potential properties. Factors affecting their structures and properties, such as ligand species, heteroatoms and active groups will also be explored.

1.2 Methodology

Generally, MGYs can be prepared by three chemical methods including the on-surface assisted synthesis, the interfacial synthesis, and the solvothermal synthesis. The on-surface synthesis means that the chemical reaction happens on a substrate which can provide a platform for the reactions, thus resulting in films of good quality but low yield. What's more, it is not easy to transfer the obtained films from the substrate, which make it difficult to do more exploration on the films. For the interfacial synthesis, films can be synthesized on the interface of liquid and liquid or gas and liquid. Such method can result in free-standing films which can be easily studied and applied. The solvothermal synthesis is that reactions can be conducted in a Pyrex tube. This method is easier than the other two methods and can achieve a high yield. Here, three methods will be generally introduced.

1.2.1 On-surface synthesis

On-surface chemistry can also be regarded as 2D chemistry, which can provide a great method to prepare defined structures from bottom-up strategy[26]. Recently, on-surface synthesis has been rapidly advanced with the aim of fabricating covalently interlinked low-dimensional nanostructures, and a number of well-known chemical reactions have been explored on different metal surfaces[27,28]. As shown in Figure 1.1, a commonly adopted protocol of on-surface synthesis is to trigger reactions among pre-

adsorbed monomers on a metal substrate under an ultra-high vacuum (UHV) chambers, whereby the monomers are in equilibrium with the substrate[29]. The metal surface can not only act as a platform for the self-assembly of the absorbates but also sometimes act as a catalyst for the reactions. Recently, a collection of different reactions including imine formation reactions, dehalogenation reactions, and dehydrogenation reactions have been reported to be suitable for the on-surface synthesis[27]. As a result, various carbon or carbon-rich nanostructures have been successfully constructed on surfaces, such as fullerene, graphene nanoribbons, nanographene, polyphenylene chains and other low-dimensional nanostructures[30].

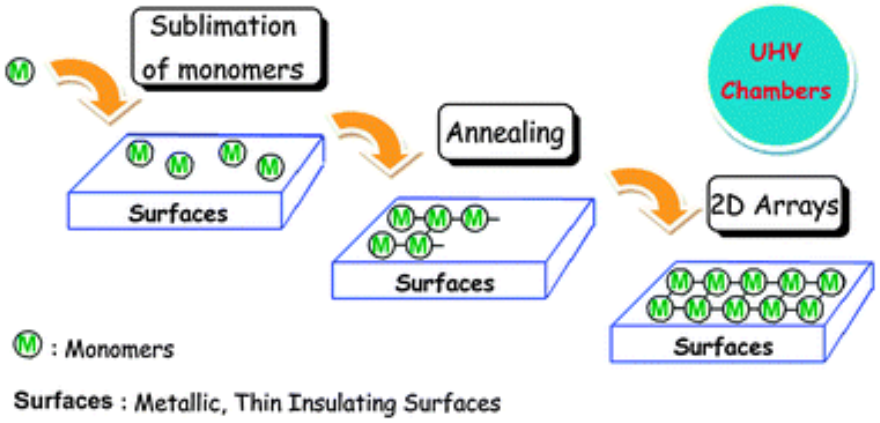

Figure 1.1 Schematic representation of an on-surface synthesis process[29].

Among these reactions, dehalogenation reaction has proven to be one of the most efficient ways to carry out the C−C homocoupling reaction among reactants with predefined C−X groups (X stands for halogens), resulting in controllable formation of different carbon scaffoldings[31]. However, forming extended covalent or 2D organometallic architectures through on-surface process remains challenging. On the one hand, it is mainly limited by the simultaneous multiple reaction channels, which

can cause undesired side reactions at high temperatures[32]. In addition, the irreversibility of the covalent C−C and C−M bond formation precludes the networks from self-ordering. More recently, dehydrogenative homocouplings of terminal alkanes[33], alkenes[34], and alkynes[35] have been demonstrated with on-surface synthesis as dehalogenative homocouplings of alkyl and alkenyl can halogenate the activity of C−H bond. Generally, from the comparison of on-surface dehydrogenative C−C couplings with alkanes, alkenes, and alkynes halides, the last one is more inclined to yield higher selectivity and fewer byproducts because the cleavage of C−X bond in alkynes is relatively facile on metal surface. Therefore, dehalogenative homocouplings of alkynyl (sp^1-carbon) halides on metal surface have been considerate as a promising strategy to form high-ordering MGY frameworks.

Yang[22] et al. reported dehalogenative C−C coupling reactions of terminal alkynyl bromides in 2018. They reported an organometallic Ag–bis-acetylide (–C≡C–Ag–C≡C–) network which is woven from the newly designed 2,4,6-tris(2-bromoethynyl)-1,3,5-triazine (Br-TET) on Ag(111) and revealed a 2D delocalized unoccupied state along the bonds of –C≡C–Ag–C≡C– with the help of STM and DFT calculations. In 2020, another large-area metallated graphyne-based networks were also designed and synthesized by Yang[23] et al. through dehalogenative homocouplings of 1,3,5-tris(2-bromoethynyl)-benzene (Br-TEB) on Ag(111) and they comprehensively studied the growth mechanism of on-surface chemistry, the crystallization, and the electronic properties of the Ag−bis-acetylide networks, which shift a new sight for the formation

of MGYs and their property exploration. What's more, a novel binodal organometallic network was demonstrated by Liu[36] et al. with the stepwise dissymmetric dehalogenative homocoupling reactions of 1,4-dibromo-2,5-diethynylbenzene (2Br-DEB) on Ag(111), which is also an inspiring work to help expand the family of MGYs.

However, it has been proved that the formation of ordered –C≡C–M–C≡C– structures at large scales by dehalogenation homocoupling reactions remains challenging. Herein, Zhang[24] et al. modified the on-surface chemistry and reported the fabrication of –C≡C–Ag–C≡C– bonded honeycomb networks by performing dehydrogenation reactions from 1,3,5-tris(4-ethynylphenyl)-benzene (Ext-TEB) at the micrometer level via a gas-mediated approach on Ag(111). The employed gas-mediated protocol features a low-temperature deprotonation step and the absence of halogens. They also found that molecular O_2 can efficiently deprotonates terminal alkyne groups of Ext-TEB at a low temperature.

These findings supplement the database of on-surface homocoupling reactions with terminal alkynyl bromides or terminal alkyne. More importantly, it may pave the way to the ultimate goal of fabricating MGYs that integrates sp^2 and sp^1-hybridized carbons with metal centers. However, the above 2D MGY-based networks were all proposed on the metal substrates and thus cannot be physically isolated easily from substrates. Therefore, they are very difficult to be used in devices. So, one of the present challenges for the preparation of MGYs is to develop methods which can form free-standing organometallic networks with large-area and high-quality.

1.2.2 Interfacial synthesis

Interfacial synthesis, can also be called “interfacial polymerization”, was initially performed by Huang[37] et al., which can be used as a convenient and versatile template-free process to fabricate pure and uniform low-dimensional materials. In general, interfacial chemistry is performed at the interface of two immiscible phases of hydrophilic and hydrophobic liquids. In such method, two reactants are dissolved in the two phases, respectively, and are confined at the interface to form new product, which is advantageous in terms of improved reaction kinetics, higher yields, and selectivity. What’s more, the liquid/liquid interface formed is stable, thus resulting in controllable synthesis through localized polymerization reaction upon the contact between two reactants. In addition to the liquid/liquid interfacial protocol, others including liquid-solid, vapor-solid, and vapor-liquid interfaces have also been reported and thus the interfacial synthesis can be classified into four types as shown in Figure 1.2.

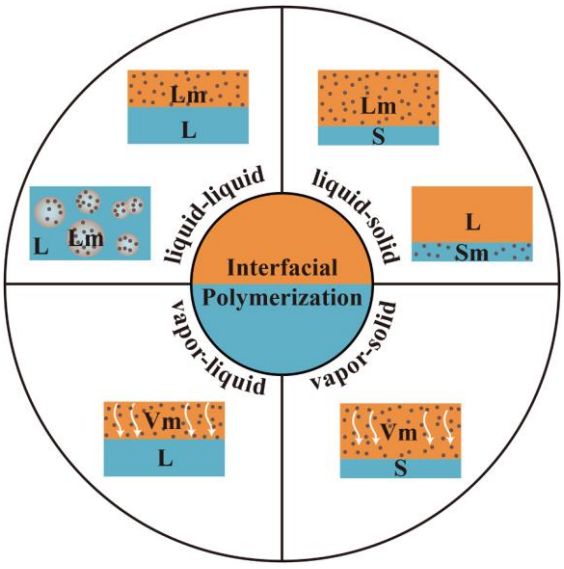

Figure 1.2 Typical interface systems of interfacial synthesis[38].

Interfacial chemistry is an efficient protocol to fabricate a wide variety of bottom-

up nanosheets. Recently, two types of interfacial synthesis including liquid/liquid and gas/liquid interfaces have been reported to lead to the carbon-carbon formation by Matsuoka[39] et al., resulting in a high-ordering crystalline GDY nanosheet. Inspired by this context, Xu et al. demonstrated two new large-area free-standing MGY organometallic nanosheets (MGONs) generated at the liquid/liquid interface of an aqueous solution of $HgCl_2$ and a hexane solution of the organic ligands, as shown in Figure 1.3. The ligands of tris(4-ethynylphenyl)-amine (L1) and 1,3,5-triethynylbenzene (L2) were used to synthesize MGONs (HgL1 and HgL2) by the base-catalyzed dehydrohalogenation reactions. These large-area continuous nanosheets with controllable thickness and high transparency can be transferred on the optical glass and other substrates and can be directly applied as free-standing films in optoelectronic devices. On the other hand, comprehensive characterizations were used to study their chemical structure, morphologies, and properties. For example, FTIR, solid ^{13}C-NMR, XPS, and DFT simulation were performed to study their chemical structures. Furthermore, TEM, SEM images, and AFM were used to display their 2D structures. At last, UV–Vis and PL were used to explore their light absorbance property and band structures.

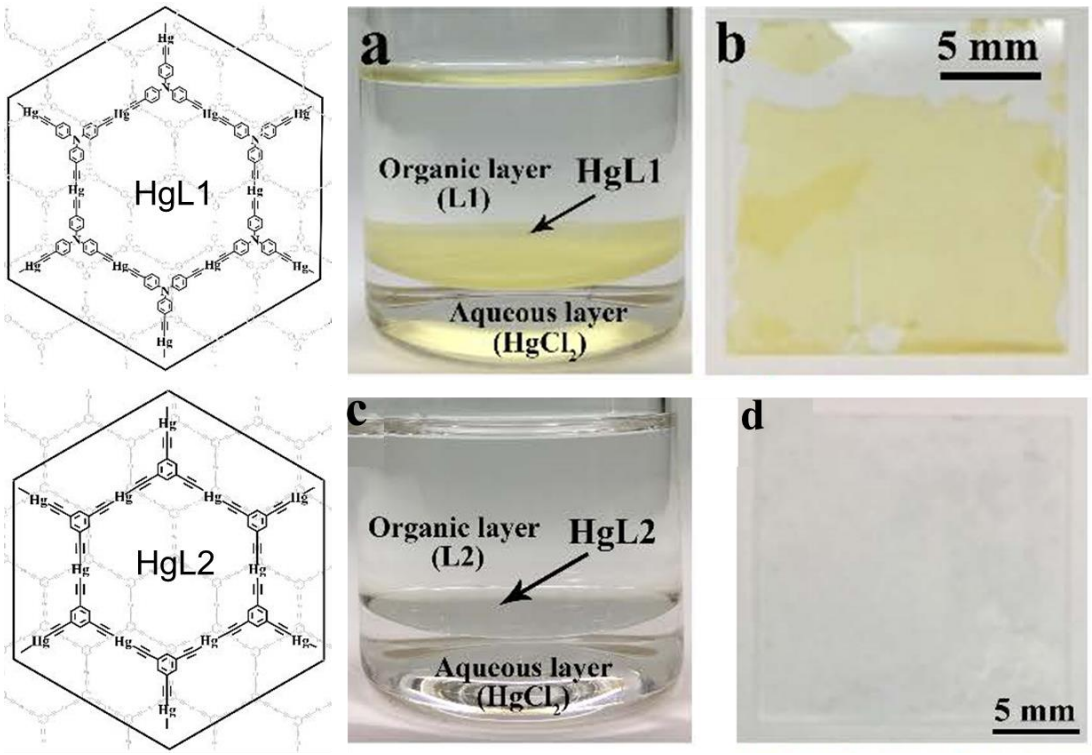

Figure 1.3 Synthesis of HgL1 and HgL2 nanosheets[25]. (a) Multi-layer HgL1 nanosheets generated at the liquid/liquid interface. (b) A photo of HgL1 nanosheets on a slide glass. (c) Multi-layer HgL2 nanosheets generated at the liquid/liquid interface. (d) A photo of HgL2 nanosheets on a slide glass.

In 2022, a series of metalloporphyrin-linked mercurated graphynes nanosheets (Hg-MTPP, M = Mn, Fe, Co, Ni, Cu, and Zn) were reported, which can be synthesized via liquid/liquid and gas/liquid interfacial method, as shown in Figure 1.4. In this work, multilayer nanosheets were synthesized at the interface of dichloromethane solution of the organic ligand of metal-porphyrin (MTPP) and the deionized water solution of $HgCl_2$. For the few-layer nanosheets prepared with gas/liquid interfacial method, the water solution of $HgCl_2$ was added into a vial firstly and then a small amount of dichloromethane solution of the metal-porphyrin (MTPP) was sprinkled gently on the surface of the aqueous phase. Hg-MTPP nanosheets were obtained on the surface after

spontaneous evaporation of the organic solvent. Their chemical structure and morphologies were studied using FTIR, Solid ^{13}C-NMR, Raman, AFM, and TEM image.

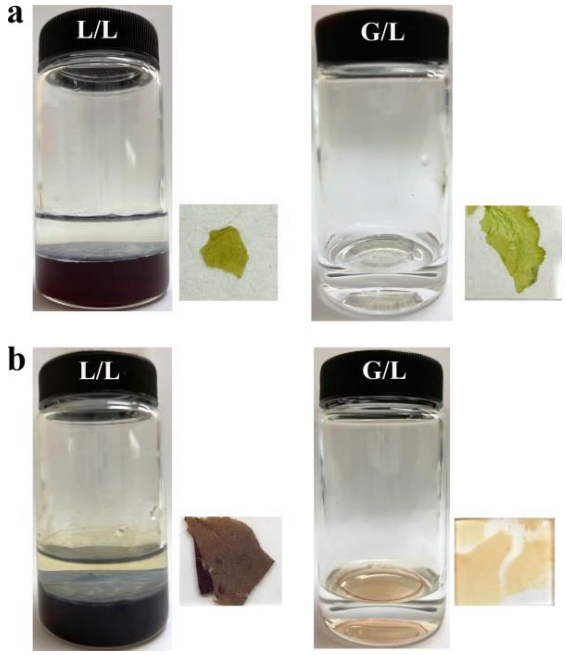

Figure 1.4 Synthesis and the photos of the of Hg-MTPP nanosheets via (a) liquid/liquid (L/L) and (b) gas/liquid (G/L) methods[40].

1.2.3 Solvothermal synthesis

Solvothermal synthesis is initially a method of producing chemical compounds, in which a solvent containing reagents is put under a high pressure and temperature condition in an autoclave[41]. In such conditions, many substances could dissolve better in the same solvent than at standard conditions, which enables reactions that would not otherwise occur and lead to new compounds or polymorphs. Solvothermal synthesis has been used to prepare a wide variety of materials including metal organic frameworks (MOFs)[42], covalent organic frameworks (COFs)[43], titanium dioxide[44], and graphene[45], and other materials. Among them, solvothermal synthesis is the most

preferable method being used in approximately 70% of published works on MOFs and COFs.

In this field, a general synthetic protocol of solvothermal synthesis can be described in Figure 1.5. First, the mixture of appropriate monomers, catalysts, and solvents or mixtures of solvents are placed in a Pyrex tube with an appropriate volume. Subsequently, the mixture is sonicated for a short time, degassed through a freeze-pump-thaw cycle, sealed, and maintained at the appropriate temperature for a certain period. After the reaction is completed, the tube is cooled at room temperature and the products were collected by centrifugation or filtration, followed by washing them with appropriate solvents at room temperature or extraction by Soxhlet to exchange for high boiling point solvents or remove the unreacted monomers or oligomers. Finally, the product was dried under vacuum at 80−120 °C and stored in the dark under nitrogen or argon protection.

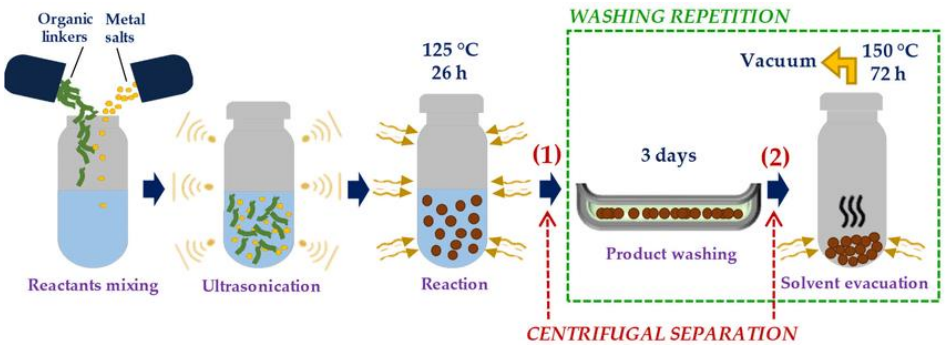

Figure 1.5 Schematic diagram of solvothermal synthesis protocol[46].

Such method is beneficial to modify the crystallinity of porous materials on a large scale. Here, this method will also be adopted in preparation of MGYs. Up to now, just several kinds of MGYs have been reported and explored. Among them, HgL1, HgL2

and Hg-GY MTPP nanosheets reported by Xu et al. have been successfully synthesized via two methods including interfacial method and solvothermal synthesis protocol[40]. For the solvothermal synthesis, the mixture of MeOH solution of $HgCl_2$ and organic ligand in CH_2Cl_2/Et_3N mixed solvent (4:1, v/v) was sealed in a tube after three times of freeze−pump−thaw cycles and was stirred at room temperature for 7 h. The porous products were obtained with a high yield of 93%. Such method can provide high yield of products, which is very beneficial to explore their electronic properties and study their applications.

1.3 Structures and properties

GDYs with the introduction of metal-bis-acetylide bonds, which integrate the advantages of both GDY and metal centers, should theoretically have many intriguing properties including unique layered structure, variety of components, controllable thickness, high exposure of active sites, and flat π-conjugated electronic properties. However, to our knowledge, related research of MGYs is still in its infancy up to now. Just few kinds of MGYs have been successfully designed and reported and there are limited discussions on their properties of MGY nanosheets. Here, we will provide a brief overview on the properties of the existing MGYs. In the very early stages, MGYs were mainly prepared via on-surface chemistry combined STM and DFT calculations. Therefore, only few structures were designed and successfully synthesized, as shown in Figure 1.6.

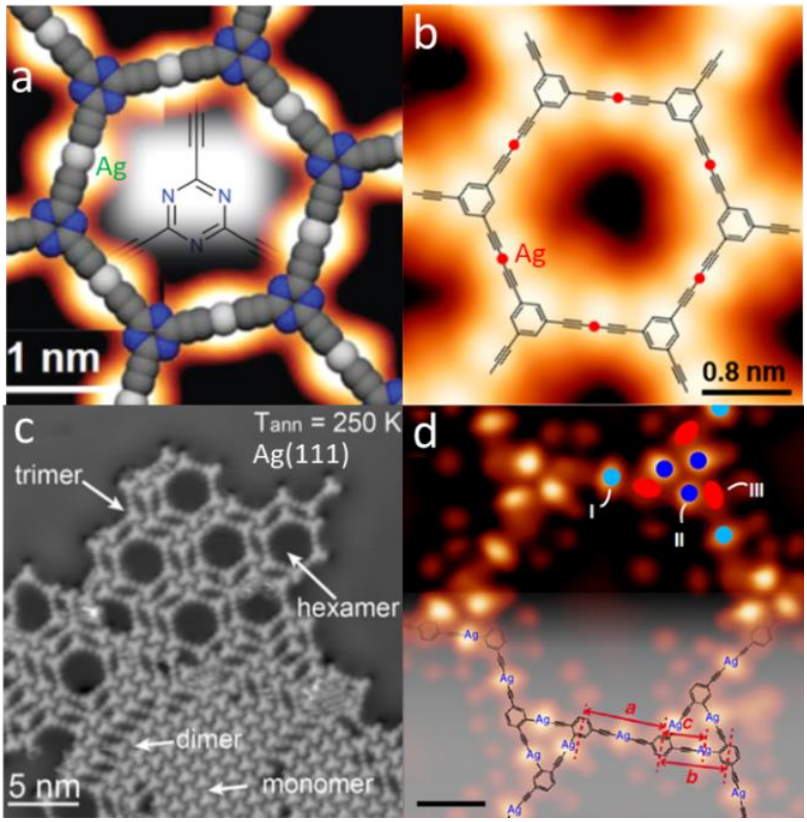

Figure 1.6 Structures of MGYs prepared on the metal surface. (a) Structure of TET-Ag network[22]. (b) Structure of TEB-Ag network[23]. (c) Structure of Ext-TEB-Ag network[24]. (d) Structure of the binodal DEB-Ag network[36].

In general, the chemical structural properties of the resulting MGY nanosheets were mainly discussed, while the electronic properties, in particular, the bonding nature of the involved metal-bis-acetylide bonds on metal surfaces, remained mostly unexplored. The surface chemistry, growth mechanism of metal-bis-acetylide networks on metal surfaces are so far not well studied and hence the suitability of the metal-bis-acetylide networks for application as 2D materials also remained mostly unexplored. Given this background, Yang et al. reported a well-ordered organometallic network with Ag-bis-acetylide (TET-Ag organometallic network) bonds, as displayed in Figure 1.6a and its electronic properties was studied in detail. They found that such networks are

metallic and that the effect of n-doping makes the conduction band (CB) shift below the Fermi energy of Ag(111). What's more, STM and DFT reveal 2D delocalized unoccupied states within the framework along the Ag-bis-acetylide bond, illustrating its characteristics of hybrid covalent and ionic bonding. However, their surface chemistry and growth mechanisms have not been well studied to date. Herin, Yang et al. demonstrated another Ag-bis-acetylide MGY-based framework (TEB-Ag MGY) with high degree of π-conjugation in large-area domain, as shown in Figure 1.6b. In this work, related properties including the crystallization, the topological defects, the delocalized unoccupied electronic states, and the site-specific doping were discussed using STM and DFT calculation. As shown in Figure 1.7, dI/dV spectra (Figure 1.7a) combined STM (Figure 1.7b and 1.7c) clearly displayed the surface state (orange line) and resonate state (S1 and S2) corresponding to the center of the pores and TEB backbones and Ag atoms, respectively, which revealed a delocalization of electronic state along TEB-Ag-TEB bridge. The DFT calculation revealed the band structure of Fermi level and CB positions, which shows an interesting feature that both Both $\pi_{/\!/}$ and $\pi_{\perp}$ bands show Dirac-cone-like crossings with a linear band dispersion around each k point (k point, a bloch vector, is used to sample the Brillouin zone. Converging this sampling is one of the essential tasks in many calculations concerning the electronic minimization.) (Figure 1.7d).

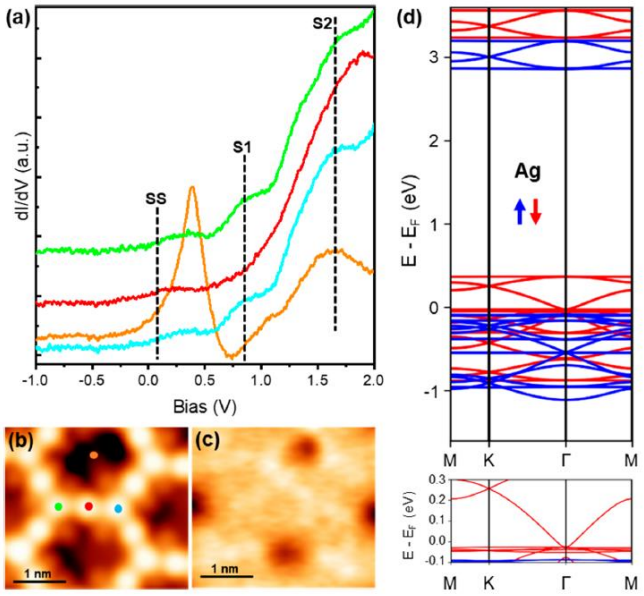

Figure 1.7 Electronic properties of the TEB-Ag organometallic network[23]. (a) dI/dV spectra recorded across the TEB−Ag−TEB bridge as indicated in (b). (b) STM image. (c) the corresponding dI/dV map recorded around the S1 state (U = 1.0 V). (d) Calculated spin-polarized band structures by DFT of the TEB-Ag network. The blue (red) lines show the spin-up (spin-down) bands. The bottom graphs highlight the bands around the Fermi level.

To delve deeper into some other properties, Zhang et al. designed and synthesized a highly regular single-layer honeycomb network with –C≡C–Ag–C≡C– bond in a micrometer domain size via gas-mediated surface reaction, as displayed in Figure 1.6c. In this work, they found that O_2 can efficiently trigger this reaction and confirmed its chemical structure using XPS and DFT calculation. What's more, a novel binodal organometallic network (Figure 1.6d) was designed and synthesized by Liu et al. via a stepwise activation strategy on Ag(111) and the mechanism of stepwise reaction and its electron distribution were studied by STM and DFT. These results demonstrate that asymmetric reactions can be used to control the surface preparation of complex and ordered nanostructures effectively.

Therefore, preparation of the easily exfoliated or free-standing MGYs still faces challenges and needs urgent research. Given this context, scientists have made great efforts to solve this problem and have achieved some accomplishments. Several kinds of free-standing MGYs have been designed and successfully synthesized up to now, as shown in Figure 1.8.

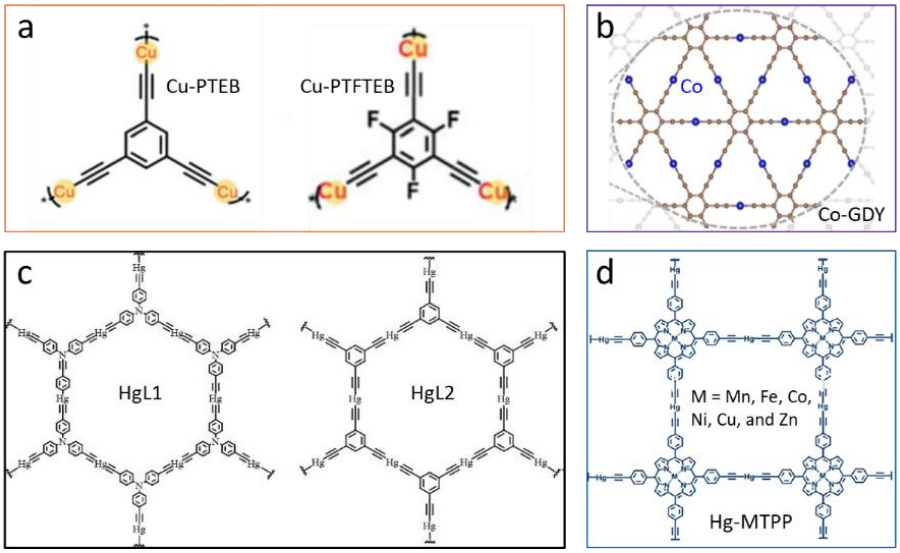

Figure 1.8 Structures of MGYs prepared by interfacial synthesis. (a) Copper-metallated conjugated acetylenic polymers[47]. (b) Cobalt metallated graphdiyne. (c) Mercurated graphyne organometallic nanosheets[48]. (d) Metalloporphyrin-linked mercurated graphynes[40].

To fabricate large domain size of MGYs, Zhang et al. reported a solvent-mediated method of large-area copper (Cu)-metallated GDY by a wet-chemistry on Cu foil surface under ambient conditions. They demonstrated two kinds of Cu-metalation frameworks (Cu-PTEB and Cu-PTFTEB, shown as Figure 1.8a) and confirmed their structures with Raman, FTIR, XPS, and EDX characterizations. The optical absorption and the band structure properties of Cu-PTEB were explored using UV−Vis and UPS characterizations, as shown in Figure 1.9. It is reported that Cu-metalation in the

framework can efficiently enhance its light absorption edge with a narrow band gap. What's more, the electric conductivity can also be significantly improved with Cu-metalation.

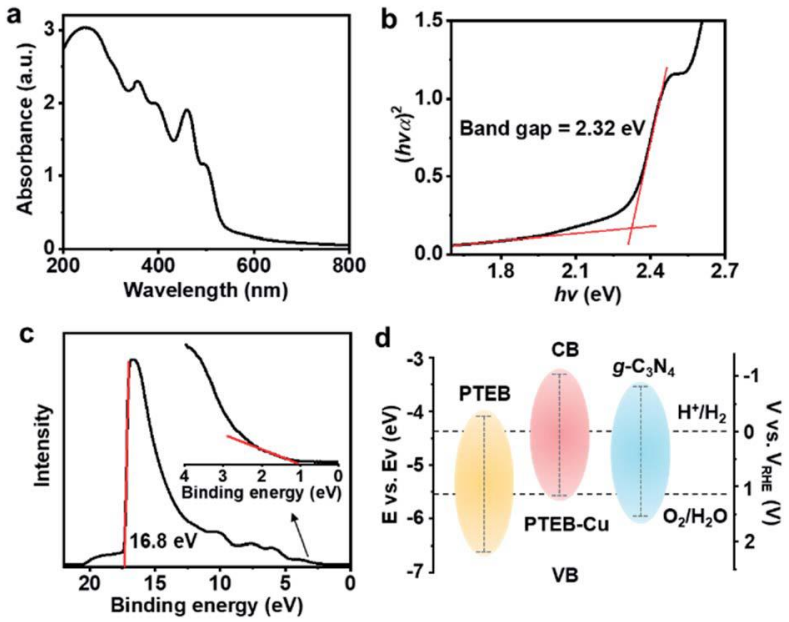

Figure 1.9 Optical absorbance and band structure of Cu-PTEB. (a) UV−Vis absorption spectrum. (b) Tauc's plot. (c) UPS spectrum. (d) Band structure diagram of Cu-PTEB compared with that of PTEB and$g\text{-}C_3N_4$[47].

A free-standing MGY named Co-GDY (Figure 1.8b) was demonstrated by Zhang et al. via an interface-assisted approach, reported such nanosheet as a semi-metallic material, and explored its ferromagnetism from the experimental level combined with DFT calculation. Recently, our group firstly reported a new class of multifunctional 2D mercurated graphyne organometallic nanosheets (HgL1 and HgL2, as shown in Figure 1.8c) and studied their nonlinear optical properties (NLO) and followed by the report on a series of metalloporphyrin-linked MGYs and exploration of their electrochemical properties (Figure 1.8d).

1.4 Applications

1.4.1 Nonlinear optics

Nonlinear optics (NLO) is a branch of modern optics that studies the nonlinear phenomena and applications of media under the action of strong coherent light. Studying NLO is of great significance to the development of laser technology, spectroscopy, and material structure analysis. The research and development of NLO materials has greatly promoted the development of related applications such as data processing, optical switching, and optical communications. It is worth noting that with the rapid development of laser technology, human demand for high-performance optical power limiting (OPL) devices is increasing to deal with the damage of laser pulses to human eyes and sensitive optical components. Additionally, among various OPL mechanisms, reverse saturable absorption (RSA) and two-photon absorption (TPA) are two popular paradigms, and the Z-scan method is the most common technique to study the OPL performance[49]. In this context, metallated polyynes have been proven to be an attractive NLO material because the metals in the conjugated skeletons feature occupied d-orbitals that can enhance their conjugation effect and thus improve the polarizability. In addition, heavy metal effects can enhance the intersystem crossing from S_1 to T_1 states to amplify the NLO response. Herin, Xu et al. designed two kinds of photo-functional MYGs (HgL1 and HgL2) and studied their nonlinear saturable absorption (SA) properties and applied them into the optical device of passively Q-switching (Figure 1.10).

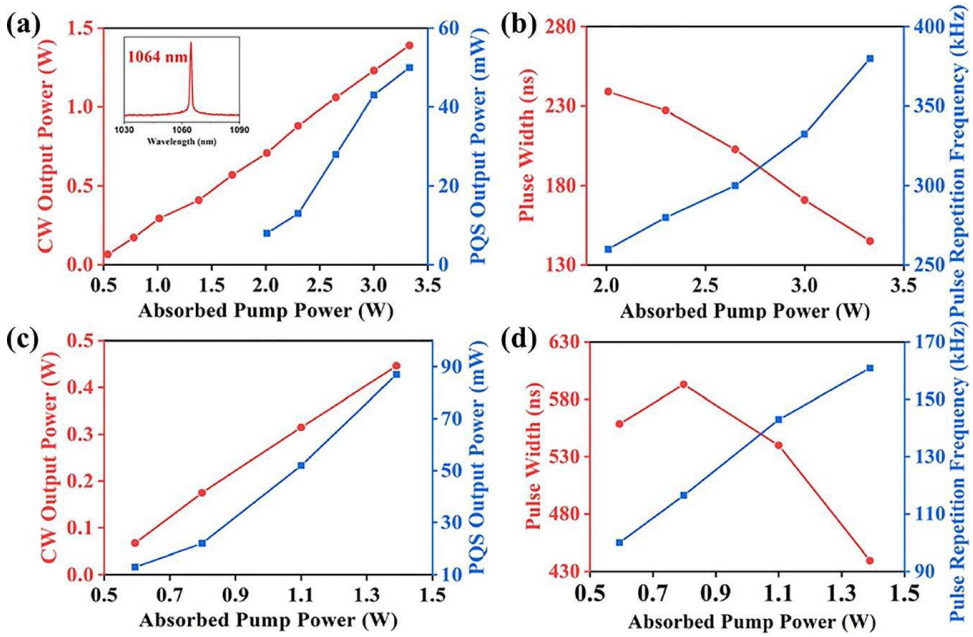

Figure 1.10 Passively Q-switched properties of HgL1 and HgL2[25]. (a) Output power of HgL1 (the inset is the laser emission spectrum). (b) Pulse width and repetition frequency of HgL1. (c) Output power of HgL2. (d) Pulse width and repetition frequency of HgL2.

Q-switching is a technology to generate a pulse with an ultra-short pulse width and a high peak power. In optics, mode-locking is an optic technique by which a laser can be made to produce pulses of light of extremely short duration. Compared with mode-locking, Q-switching can give a laser with a much larger pulse energy. In this work, the NLO properties of the nanosheets were investigated under excitation wavelengths at both 532 and 1064 nm using the Z-scan technique. Interestingly, both nanosheets showed optical switching behavior of SA and HgL2 nanosheets exhibit better pulse properties. This work reveals that MGY materials can not only become a new functional 2D carbon-rich material, but also have fascinating properties and application prospects, which will be helpful in the future design of various optoelectronic materials and devices.

1.4.2 Catalysis

Energy conversion technology has attracted great attention from the scientific community facing the global problem of energy crisis that affects the sustainable development of human society. In the process of energy conversion, catalysis, such as photocatalysis, electrocatalysis and photoelectrocatalysis, plays a decisive role and can effectively convert electrical energy and light energy into chemical energy. It is noted that organometallic polymers have been widely applied in organic light-emitting diode (OLED), organic solar cell (OSC) and organic thermoelectric (OTE) devices, which illustrates the huge applicability of metallization systems in the mutual energy conversion[50]. Accordingly, MGYs have a great potential for catalysis because such materials possess well-defined skeletons and discrete pores with metal ions homogeneously distributed in the skeleton, which has great significance for improving the selectivity of catalytic reactions.

The development of photocatalysts is of great significance for artificial photosynthesis and light energy conversion[51]. In nature, chlorophyll arrays have a well-defined wheel-like structure that efficiently collects light and transfers energy to reaction centers in photosynthetic systems. Inspired by this principle, synthetic chemists design artificial photocatalytic systems by organizing chromophores into ordered extended structures. MGYs are characterized of integrating various π units into extended ordered structures, which are expected to serve as an excellent platform for designing photocatalysts. HgL1, one of the first two free-standing mercurated

graphynes has a strong light absorbance and suitable band structure, while the fast carrier recombination renders its performance for photocatalysis. Therefore, Zhao et al.[52] constructed HgL1 with carbon dots to form a CDs/HgL1 composite to improve its photocatalytic properties and found that such composite achieved a good performance for the H_2O_2 photoproduction with a rate of 800 μmol h^{-1} g^{-1}. The role of CDs for boosting the activity revealed that CDs can change the surface from hydrophobic to hydrophilic and participate in the entire photocatalytic reaction. Besides CDs can accelerate electron-hole separation and migration and improve redox activity, thereby promoting the photocatalytic production of H_2O_2 (Figure 1.11a).

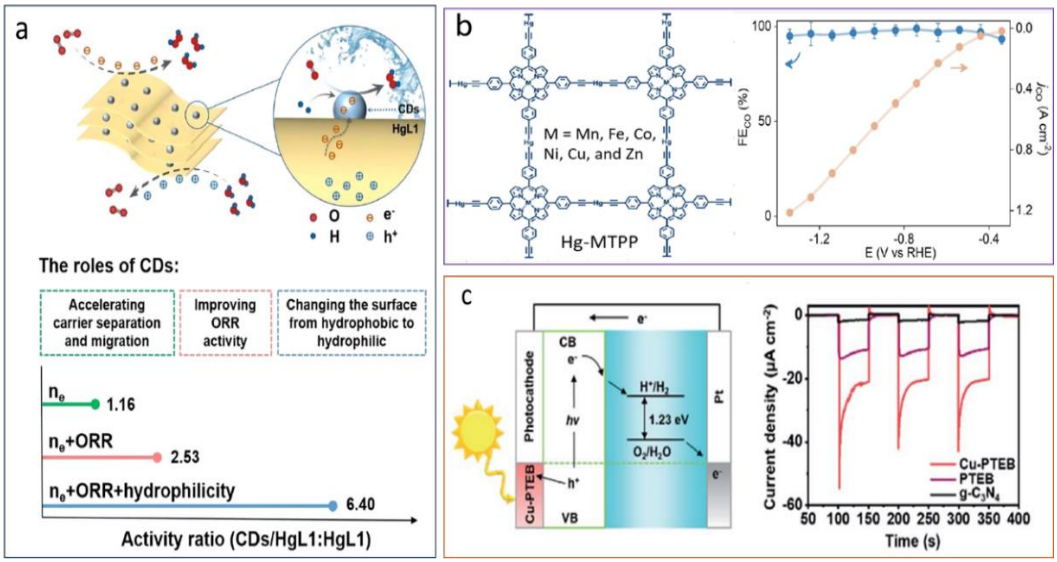

Figure 1.11 Application illustration of MGYs. (a) Photocatalytic H_2O_2 production with CDs/HgL1 composite[52]. (b) electrocatalytic CO_2RR with Hg-CoTPP[40]. (c) PEC-HER with Cu-PTEB photocathode[47].

Electrocatalysis is another way of energy conversion, which is the conversion between electrical energy and chemical energy. The conductivity of electrocatalysts is a key factor in determining the kinetics and efficiency of catalytic systems. Molecular

catalysts provide strategies to modulate catalytic activity by changing the types of metal ions and organic ligands[53,54]. Therefore, MGYs integrating organic ligands and metal ions in a framework can be regarded as a particularly promising electrocatalyst. Fang et al. developed a metalloporphyrin-linked mercurated graphynes with Co active sites with good conductivity. The as-obtained Hg-CoTPP showed a good performance for electroreduction of CO_2 to CO (CO_2RR) with the CO faraday efficiency (FE) of 95.6% at −0.76 V and CO FE of over 90% even at −1.26 V in an H-type cell (Figure 1.11b). What's more, the DFT calculations revealed that Co as the metal center act as the active site for CO_2RR and the introduction of mercurated graphyne block into Hg-MTPP can effectively improve selectivity because it helps reduce the overpotential of CO_2RR but increases the overpotential of hydrogen evolution reaction (HER). This study provides a feasible approach to design electrocatalysts at the molecular level to achieve high FE and high current density.

Since a photoelectrochemical (PEC) system using TiO_2 as an electrode to split water was reported by Fujishima and Honda, photoelectrochemistry has increasingly been recognized as a leading method for converting solar energy into energy[55]. So far, there have been some breakthroughs in the PEC HER through enhancing light absorption, charge transfer, and charge separation in PEC devices[56]. However, less attention has been paid to designing photoelectrocatalysts at the atomic level to promote catalytic reactions on the photoelectrode surface[57]. The lack of mechanism research at this level has largely hindered the improvement of the overall light energy conversion

efficiency of the PEC system. In this case, Zhang et al.[47] designed a conjugated 2D Cu-metalated materials and reported that Cu-PTEB with an enhanced conductivity of 8.7 x10^{-5} S cm^{-1} can achieve a high hydrogen-evolution photocurrent density of 22 mA cm^{-2} at 0.3 V (Figure 1.11c). This work reveals that metal atoms help tune the intrinsic electronic properties of carbon-rich materials, which will be expected to enrich their potential applications in different fields, not only for photocatalysis but also for the study of their optoelectronic devices.

1.5 Target of work

Based on the research background, in this project, different kinds of MGYs will be prepared by base-catalyzed dehydrohalogenation reactions to enrich the category of MGYs so as to systematically investigate their potential properties and applications. Factors affecting its structure and properties, such as ligand types and heteroatoms are also explored.

Firstly, transition metals (such as Hg, Pt, and Ni) as metal functional units will be introduced into the skeleton of GDYs to obtain a series of novel MGYs that integrate both the advantages of metal centers and graphynes. Secondly, heteroatoms (such as N, F, Cl, etc.) with selected organic ligands are proposed to be introduced into the frameworks of MGYs to adjust their related properties. Finally, their applications in photocatalysis, electrocatalysis, and memory devices will be explored.

The catalytic activity and selectivity of MGYs may be regulated by organic ligands, heteroatoms, and metal units, resulting in the adjustment of the energy level of

molecular orbital. Moreover, the π-π interaction between layers of MGYs as well as the carrier mobility will also be investigated. With the help of in-situ characterization technology and theoretical simulation calculation, the relationship between the catalytic performance and the interfacial mass transfer, charge dynamics process, the coordination structure and electronic state structure of catalytic center will be explored. It is expected that the combination of such unique chemical structure with improved mechanical processability and intriguing photoelectric properties are beneficial for the future design and application of MGYs.

References

1. Casola, F., Van Der Sar, T. & Yacoby, A. Probing Condensed Matter Physics with Magnetometry based on Nitrogen-vacancy Centres in Diamond. *Nat. Rev. Mater.* **3**, 1–13 (2018).
2. Fang, H. & Hu, W. Photogating in Low Dimensional Photodetectors. *Adv. Sci.* **4**, 1700323 (2017).
3. Yan, Y. & Zhao, Y. Organic Nanophotonics: from Controllable Assembly of Functional Molecules to Low-Dimensional Materials with Desired Photonic Properties. *Chem. Soc. Rev.* **43**, 4325–4340 (2014).
4. Novoselov, K. S. et al. Electric Field Effect in Atomically Thin Carbon Films. *Science.* **306**, 666–669 (2004).
5. Tan, C., Cao, X., Wu, X. J., He, Q., Yang, J., Zhang, X. & Zhang, H. Recent Advances in Ultrathin Two-Dimensional Nanomaterials. *Chem. Rev.* **117**, 6225–6331 (2017).
6. Zeng, M., Xiao, Y., Liu, J., Yang, K. & Fu, L. Exploring Two-Dimensional Materials Toward the Next-Generation Circuits: from Monomer Design to Assembly Control. *Chem. Rev.* **118**, 6236–6296 (2018).
7. Sakamoto, R., Fukui, N., Maeda, H., Matsuoka, R., Toyoda, R., & Nishihara, H. The Accelerating World of Graphdiynes. *Adv. Mater.* **31**, 1804211 (2019).
8. Kang, J., Wei, Z. & Li, J. Graphyne and Its Family: Recent Theoretical Advances. *ACS Appl. Mater. Interfaces* **11**, 2692–2706 (2018).
9. Li, Y., Xu, L., Liu, H. & Li, Y. Graphdiyne and Graphyne: From Theoretical Predictions to Practical Construction. *Chem. Soc. Rev.* **43**, 2572–2586 (2014).
10. Baughman, R., Eckhardt, H. & Kertesz, M. Structure‐Property Predictions for New Planar Forms of Carbon: Layered Phases Containing sp^2 and sp Atoms. *J. Chem. Phys* **87**, 6687–6699 (1987).
11. Li, G., Li, Y., Liu, H., Guo, Y., Li, Y., & Zhu, D. Architecture of Graphdiyne Nanoscale films. *Chem. Commun.* **46**, 3256–3258 (2010).

12. Bunz, U. H. F., Rubin, Y. & Tobe, Y. Polyethynylated Cyclic π-Systems: Scaffoldings for Novel Two and Three-Dimensional Carbon Networks. *Chem. Soc. Rev.* **28**, 107–119 (1999).
13. Huang, C., Li, Y., Wang, N., Xue, Y., Zuo, Z., Liu, H., & Li, Y. Progress in Research into 2D Graphdiyne-Based Materials. *Chem. Rev.* **118**, 7744–7803 (2018).
14. Colson, J. W. & Dichtel, W. R. Rationally Synthesized Two-Dimensional Polymers. *Nat. Chem.* **5**, 453–465 (2013).
15. Rodríguez-San-Migu, D., Amo-Ochoa, P. & Zamora, F. MasterChem: Cooking 2D-Polymers. *Chem. Commun.* **52**, 4113–4127 (2016).
16. Sakamoto, R., Takada, K., Pal, T., Maeda, H., Kambe, T., & Nishihara, H. Coordination Nanosheets (CONASHs): Strategies, Structures and Functions. *Adv. Mater.* **53**, 5781–5801 (2017).
17. Zheng, J., Hao, J., Ling, F., Jing, H., Chen, Y., Zhou, T., ... & Zhou, M. Two-Dimensional Au-1, 3, 5 triethynylbenzene Organometallic Lattice: Structure, Half-Metallicity, and Gas Sensing. *J. Chem. Phys* **149** (2018).
18. Chen, Y. & Sun, Q. Magnetic Two-Dimensional Organic Topological Insulator: Au–1, 3, 5-triethynylbenzene Framework. *J. Chem. Phys.* **147,** (2017).
19. Kung, H., Lee, L., Wu, S., Cheng, H. & Chiang, C. Sluggish σ-Bond Formation Between sp-Hybridized Carbons: Acetylide Coupling on Ag(111). *J. Am. Chem. Soc.* **129**, 1028–1029 (2007).
20. Long, M., Tang, L., Wang, D., Li, Y. & Shuai, Z. Electronic Structure and Carrier Mobility in Graphdiyne Sheet and Nanoribbons: Theoretical Predictions. *ACS Nano* **5**, 2593–2600 (2011).
21. Mortazavi, B., Shahrokhi, M., Madjet, M. E., Hussain, T., Zhuang, X. & Rabczuk, T. N-, B-, P-, Al-, As-, and Ga-Graphdiyne/Graphyne Lattices: First-Principles Investigation of Mechanical, Optical and Electronic Properties. *J. Mater. Chem. C* **7**, 3025–3036 (2019).

22. Yang, Z., Gebhardt, J., Schaub, T. A., Sander, T., Schönamsgruber, J., Soni, H. & Maier, S. Two-Dimensional Delocalized States in Organometallic Bis-Acetylide Networks on Ag (111). *Nanoscale* **10**, 3769–3776 (2018).

23. Yang, Z., Sander, T., Gebhardt, J., Schaub, T. A., Schonamsgruber, J., Soni, H. R. & Maier, S. Metalated Graphyne-Based Networks as Two-Dimensional Materials: Crystallization, Topological Defects, Delocalized Electronic States, and Site-Specific Doping. *ACS Nano* 14, 16887–16896 (2020).

24. Zhang, Y. Q., Paintner, T., Hellwig, R., Haag, F., Allegretti, F., Feulner, P. & Klappenberger, F. Synthesizing Highly Regular Single-Layer Alkynyl-Silver Networks at the Micrometer Scale via Gas-Mediated Surface Reaction. *J. Am. Chem. Soc.* **141**, 5087–5091 (2019).

25. Xu, L., Sun, J., Tang, T., Zhang, H., Sun, M., Zhang, J. & Wong, W. Y. Metallated Graphynes as a New Class of Photofunctional 2D Organometallic Nanosheets. *Angew. Chem. Int. Ed.* **60**, 11326–11334 (2021).

26. Mendez, J., Lopez, M. F. & Martin-Gago, J. A. On-Surface Synthesis of Cyclic Organic Molecules. *Chem. Soc. Rev.* **40**, 4578–4590 (2011).

27. Held, P. A., Fuchs, H. & Studer, A. Covalent-Bond Formation via On-Surface Chemistry. *Chemistry* **23**, 5874–5892 (2017).

28. Kudernac, T., Lei, S., Elemans, J. A. A. W. & De Feyter, S. Two-Dimensional Supramolecular Self-Assembly: Nanoporous Networks on Surfaces. *Chem. Soc. Rev.* **38**, 402–421 (2009).

29. Franc, G. & Gourdon, A. Covalent Networks through On-surface Chemistry in Ultra-High Vacuum: State-of-the-Art and Recent Developments. *Phys. Chem. Chem. Phys.* **13**, 14283–14292 (2011).

30. Sun, Q., Zhang, R., Qiu, J., Liu, R. & Xu, W. On-Surface Synthesis of Carbon Nanostructures. *Adv. Mater.* **30**, e1705630 (2018).

31. Grill, L., Dyer, M., Lafferentz, L., Persson, M., Peters, M. V. & Hecht, S. Nano-Architectures by Covalent Assembly of Molecular Building Blocks. *Nat.*

Nanotechnol. **2**, 687–691 (2007).

32. Gao, H. Y., Wagner, H., Zhong, D., Franke, J. H., Studer, A. & Fuchs, H. Glaser Coupling at Metal Surfaces. *Angew. Chem., Int. Ed.* **14**, 4024–4028 (2013).
33. Zhong, D., Franke, J. H., Podiyanachari, S. K., Blömker, T., Zhang, H., Kehr, G. & Chi, L. Linear Alkane Polymerization on a Gold Surface. *Science.* **334**, 213–216 (2011).
34. Sun, Q., Cai, L., Ding, Y., Xie, L., Zhang, C., Tan, Q. & Xu, W. Dehydrogenative Homocoupling of Terminal Alkenes on Copper Surfaces: A Route to Dienes. *Angew. Chem., Int. Ed.* **127**, 4632–4635 (2015).
35. Liu, J., Chen, Q., Xiao, L., Shang, J., Zhou, X., Zhang, Y. & Wu, K. Lattice-Directed Formation of Covalent and Organometallic Molecular Wires by Terminal Alkynes on Ag Surfaces. *ACS Nano* **9**, 6305–6314 (2015).
36. Liu, J., Chen, Q., Cai, K., Li, J., Li, Y., Yang, X. & Wu, K. Stepwise On-surface Dissymmetric Reaction to Construct Binodal Organometallic Network. *Nat. Commun.* **10**, 2545 (2019).
37. Huang, J. & Kaner, R. B. A General Chemical Route to Polyaniline Nanofibers. *J. Am. Chem. Soc.* **126**, 851–855 (2004).
38. Gao, N., Yu, J., Chen, S., Xin, X. & Zang, L. Interfacial Polymerization for Controllable Fabrication of Nanostructured Conducting Polymers and Their Composites. *Synth. Met.* **273,** 116693 (2021).
39. Matsuoka, R., Sakamoto, R., Hoshiko, K., Sasaki, S., Masunaga, H., Nagashio, K. & Nishihara, H. Crystalline Graphdiyne Nanosheets Produced at a Gas/Liquid or Liquid/Liquid Interface. *J. Am. Chem. Soc.* **139**, 3145–3152 (2017).
40. Fang, M., Xu, L., Zhang, H., Zhu, Y. & Wong, W. Y. Metalloporphyrin-Linked Mercurated Graphynes for Ultrastable CO_2 Electroreduction to CO with nearly 100% Selectivity at a Current Density of 1.2 A cm^{-2}. *J. Am. Chem. Soc.* **144**, 15143–15154 (2022).
41. Demazeau, G. Solvothermal Reactions: An Original Route for the Synthesis of

Novel Materials. *J. Mater. Sci.* **43**, 2104–2114 (2008).

42. Farha, O. K. & Hupp, J. T. Rational Design, Synthesis, Purification, and Activation of Metal−Organic Framework Materials. *Acc. Chem. Res.* **43**, 1166–1175 (2010).
43. Yaghi, O. M., Kalmutzki, M. J. & Diercks, C. S. Introduction to Reticular Chemistry: Metal-Organic Frameworks and Covalent Organic Frameworks. (John Wiley & Sons, 2019).
44. Ong, W. J., Tan, L., Chai, S. P., Yong, S. T. & Mohamed, A. R. Highly Reactive {001} Facets of TiO_2-Based Composites: Synthesis, Formation Mechanism and Characterization. *Nanoscale* **6**, 1946–2008 (2014).
45. Xiang, Q., Yu, J. & Jaroniec, M. Graphene-Based Semiconductor Photocatalysts. *Chem. Soc. Rev.* **41**, 782–796 (2012).
46. Kamal, K., Bustam, M. A., Ismail, M., Grekov, D., Mohd Shariff, A. & Pré, P. Optimization of Washing Processes in Solvothermal Synthesis of Nickel-Based MOF-74. *Mater.* **13,** 2741 (2020).
47. Zhang, T., Xu, S., Hou, Y., Chai, G., Olianas, D., Liao, Z. & Feng, X. Solvent-Mediated Engineering of Copper-Metalated Acetylenic Polymer Scaffolds with Enhanced Photoelectrochemical Performance. *J. Mater. Chem. A* **9**, 9729–9734 (2021).
48. Zhan, X., Kang, H., Qian, F., Xu, L., Zheng, Y. & Huang, Z. Magnetic Investigation on the Two-Dimensional Metallated Graphdiyne Nanosheets. *J. Alloys Compd.* **940,** 168693 (2023).
49. Zhou, G. & Wong, W. Y. Organometallic Acetylides of Pt^{II}, Au^{I} and Hg^{II} as New Generation Optical Power Limiting Materials. *Chem. Soc. Rev.* **40**, 2541–2566 (2011).
50. Zhang, C., Xu, L. & Wong, W. Y. Polymetallaynes and Molecular Metallaynes Containing Platinum, Mercury and Gold for Optoelectronic and Magnetic Applications. *Chin. J. Chem.* **41**, 2159–2178 (2023).
51. Medina, D. D., Sick, T. & Bein, T. Photoactive and Conducting Covalent Organic

Frameworks. *Adv. Energy Mater.* **7**, 1700387 (2017).

52. Zhao, Y., Xu, L., Wang, X., Wang, Z., Liu, Y., Wang, Y. & Kang, Z. A Comprehensive Understanding on the Roles of Carbon Dots in Metallated Graphyne Based Catalyst for Photoinduced H_2O_2 Production. *Nano Today* **43,** 101428 (2022).
53. Lin, S., Diercks, C. S., Zhang, Y. B., Kornienko, N., Nichols, E. M., Zhao, Y. & Chang, C. J. Covalent Organic Frameworks Comprising Cobalt Porphyrins for Catalytic CO_2 Reduction in water. *Science.* **349**, 1208–1213 (2015).
54. Göttle, A. J. & Koper, M. T. M. Determinant Role of Electrogenerated Reactive Nucleophilic Species on Selectivity During Reduction of CO_2 Catalyzed by Metalloporphyrins. *J. Am. Chem. Soc.* **140**, 4826–4834 (2018).
55. Fujishima, A. & Honda, K. Electrochemical Photolysis of Water at a Semiconductor Electrode. *Nat.* **238**, 37–38 (1972).
56. Zhao, E., Du, K., Yin, P. F., Ran, J., Mao, J., Ling, T. & Qiao, S. Z. Advancing Photoelectrochemical Energy Conversion through Atomic Design of Catalysts. *Adv. Sci.* **9**, e2104363 (2022).
57. Ling, T., Jaroniec, M. & Qiao, S. Z. Recent Progress in Engineering the Atomic and Electronic Structure of Electrocatalysts via Cation Exchange Reactions. *Adv. Mater.* **32**, 2001866 (2020).

Chapter 2

Synthesis and Properties of Mercury Graphynes and Application Studies in the H_2O_2 Photoproduction

2.1 Introduction

Graphyne-based materials have been revolutionized since the successful isolation of graphdiyne (GDY) in 2010[1,2]. Such materials characterized by a porous two-dimensional (2D) structure possess sufficient surface for the anchoring of single atoms, which is beneficial to improve the selectivity and activity of catalytic performance[3-7]. However, the controllable preparation of GDY-based materials confining single atoms remains a huge challenge due to the inhomogeneous structures and unstable active sites, thus a comprehensive understanding of the catalytic mechanism at the atomic level from an experimental perspective is still lacking[8]. In recent years, scientists found that the transition metal elements as a new form of molecular functionality can be introduced into the skeleton of GDY to form metallated graphynes (MGYs) that feature definite metal-bis-acetylide bonds (–C≡C–M–C≡C–), which can achieve controllable distribution of single metal atoms[9-12]. Subsequently, a series of MGYs (M = Au, Ag, Hg, Cu, and Co) have been successfully explored and proven to be a novel class of functional 2D materials integrating the advantages both of graphyne and metal centers, thus gaining a wide range of applications in room temperature ferromagnetism[13], optical devices[14], and catalysis[15-17].

Among these MGYs, a variety of mercury graphynes (Hg-GYs) have been

prepared with large scale as efficient electro- and photo-catalysts. It is noted that tris(4-ethynylphenyl)amine-linked Hg-GYs combined with carbon dots can achieve an efficient photocatalytic H_2O_2 production by oxygen reduction reaction (ORR)[16]. In addition, the blocks of Hg(II)-alkynes in metalloporphyrin-linked Hg-GYs exhibit an obvious inhibition of hydrogen evolution, thus effectively improving the selectivity of the catalytic reaction[17]. However, the overall H_2O_2 ORR and water oxidation reaction (WOR) without additives is regarded as a more competitive research because it is a green catalytic process that can achieve 100% utilization efficiency of atoms and energy with O_2 and H_2O[18-21]. Therefore, it is imperative to rationally design MGYs to achieve overall H_2O_2 photoproduction and reveal its detailed catalytic mechanism.

Based on such previous research, we proposed to utilize different kinds of organic ligands to expand the variety of Hg-GYs. On the other hand, utilization of selected organic ligands is an effective way to introduce heteroatoms or active groups into the framework of Hg-GYs. It is understood that the introduction of heteroatoms and active groups can optimize the electronic properties in terms of electron distribution and charge migration by adjusting the conjugation and bonding environment. For instance, several studies have shown that heteroatoms (N, F, B, or S)[22-24] or amino groups[25-27] co-doped graphene has surprising catalytic activities. Such proposals are expected to effectively enrich the family of Hg-GYs and their properties and applications. However, a comprehensive understanding of how specific structural features affect each step in photocatalytic H_2O_2 production with MGYs is still unexplored, especially how to

achieve controllable charge migration during the catalytic process, while such information is vital for the rational design of efficient solar-driven H_2O_2 production systems.

Herein, we reported a series of Hg-GYs (**TEPB-Hg-GY**, **TEPT-Hg-GY**, **NH_2-Hg-GY**, and **F-Hg-GY**) and studied their chemical structures, crystal structures, and electronic structures and explore their performance toward H_2O_2 photoproduction. It was found that the introduction of heteroatoms or active groups has little effect on their morphologies but has a great impact on crystallinity and electronic properties. At last, we found that the aminated mercury graphynes (**NH_2-Hg-GY**) bearing suitable band structures and separated redox centers. **NH_2-Hg-GY** exhibits a high efficiency toward photocatalytic H_2O_2 production via the dual-channel pathway under visible-light irradiation ($\lambda \geq 420$ nm) in pure water and open air. Notably, comprehensive experiments combined with density functional theory (DFT) calculations indicate that controllable charge carrier migration is achieved during multiple catalytic processes and illustrate that the two-step $2e^-$ ORR occurred on the benzene ring while the one-step $2h^+$ WOR occurred on the acetylene. As a result, **NH_2-Hg-GY** exhibits an H_2O_2 yield of 1276.4 μmol h^{-1} g^{-1} from pure water and air atmosphere and even achieves a higher yield of 2112.6 μmol h^{-1} g^{-1} in a saturated O_2 atmosphere. In contrast, the comparative catalyst without amino groups (**TEB-Hg-GY**) shows no activity for the same photocatalysis. In addition, DFT calculation reveals that the amino group and Hg(II) ions can efficiently alter the energy landscape, in which the amino groups are

very helpful in accelerating the separation of photogenerated electron-hole (e^-– h^+) pairs and the Hg(II)-alkyne blocks can suppress the hydrogen revolution efficiently. This work reveals the mechanism involving of MGY for the overall photocatalytic H_2O_2 production, providing a general guidance for the design of more competitive photocatalysts.

2.2 Synthesis and characterization of mercury graphynes

2.2.1 Synthesis of organic ligands

The synthetic routes of the designed organic ligand (**TEPB**, **TEPT**, **TEBA**, and **TEFB**) as shown in Figure 2.1.

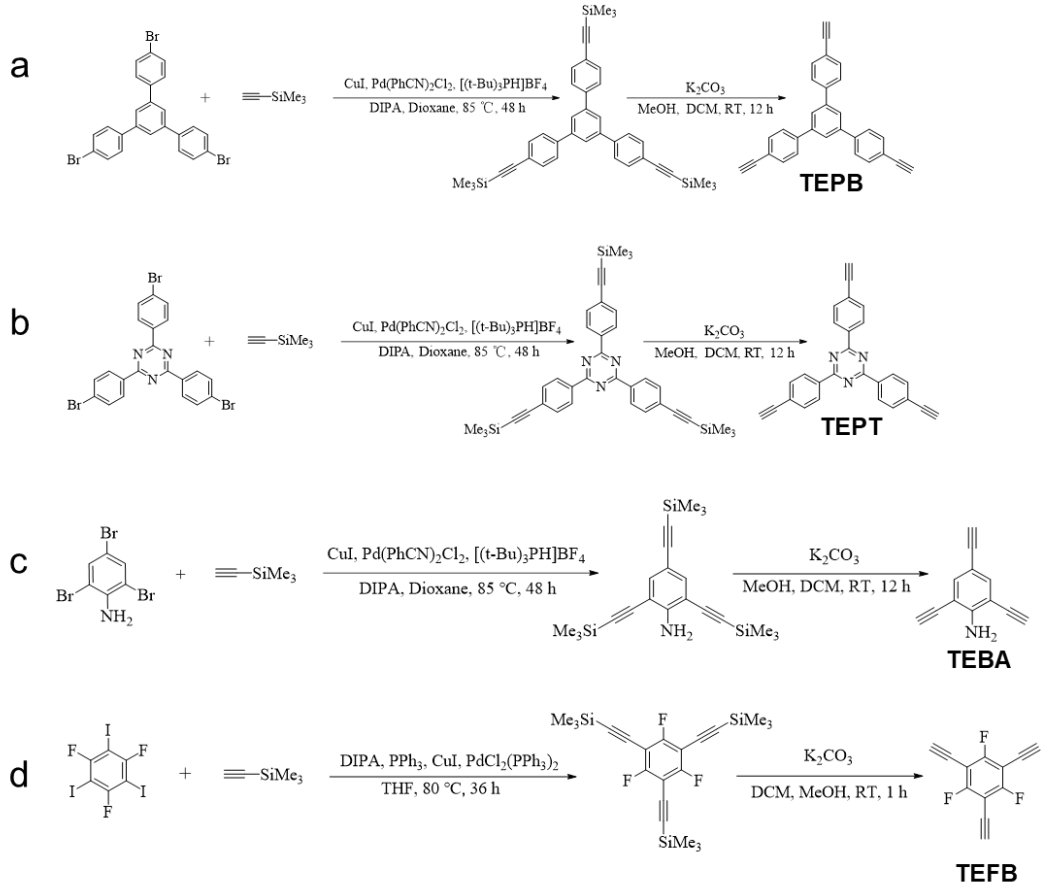

Figure 2.1 Synthetic routes of the organic ligands of (a) **TEPB**, (b) **TEPT**, (c) **TEBA**, and (d) **TEFB**.

For the ligands of **TEPB**, **TEPT**, **TEBA**, and **TEFB**, their synthetic routes are almost the same. For the **TEPB**, the ligand of 1,3,5-tris[4-(trimethylsilyl)ethynyl]phenyl]benzene was synthesized from the reaction of 1,3,5-tris(4-bromophenyl)benzene and trimethylsilylacetylene according to the modified Sonogashira coupling reaction[28]. Then the trimethylsilyl group was then removed to form the as-designed ligand of 1,3,5-triethynyltriphenylbenzene **(TEPB)**. Similarly, the ligands of 2,4,6-tris(4-ethynylphenyl)-1,3,5-triazine **(TEPT)**, 2,4,6-triethynylbenzenamine **(TEBA)**, and 1,3,5-triethynyl-2,4,6-trifluoro-benzene **(TEFB)** were synthesized using the same method. The structures of **TEPB**, **TEPT**, **TEBA**, and **TEFB** were characterized by ^{1}H NMR, ^{13}C NMR, and MS (the details are shown in Chapter 5).

2.2.2 Synthesis of mercury graphynes

The synthetic routes of the mercury graphynes are shown in Figure 2.2. **TEPB-Hg-GY**, **TEPT-Hg-GY**, **TEBA-Hg-GY**, and **TEFB-Hg-GY** were synthesized from the ligands of **TEPB**, **TEPT**, **TEBA**, and **TEFB**, respectively via the base-catalyzed dehydrohalogenation reactions for 72 h according to the previous literature method[14] (the details are shown in Chapter 5).

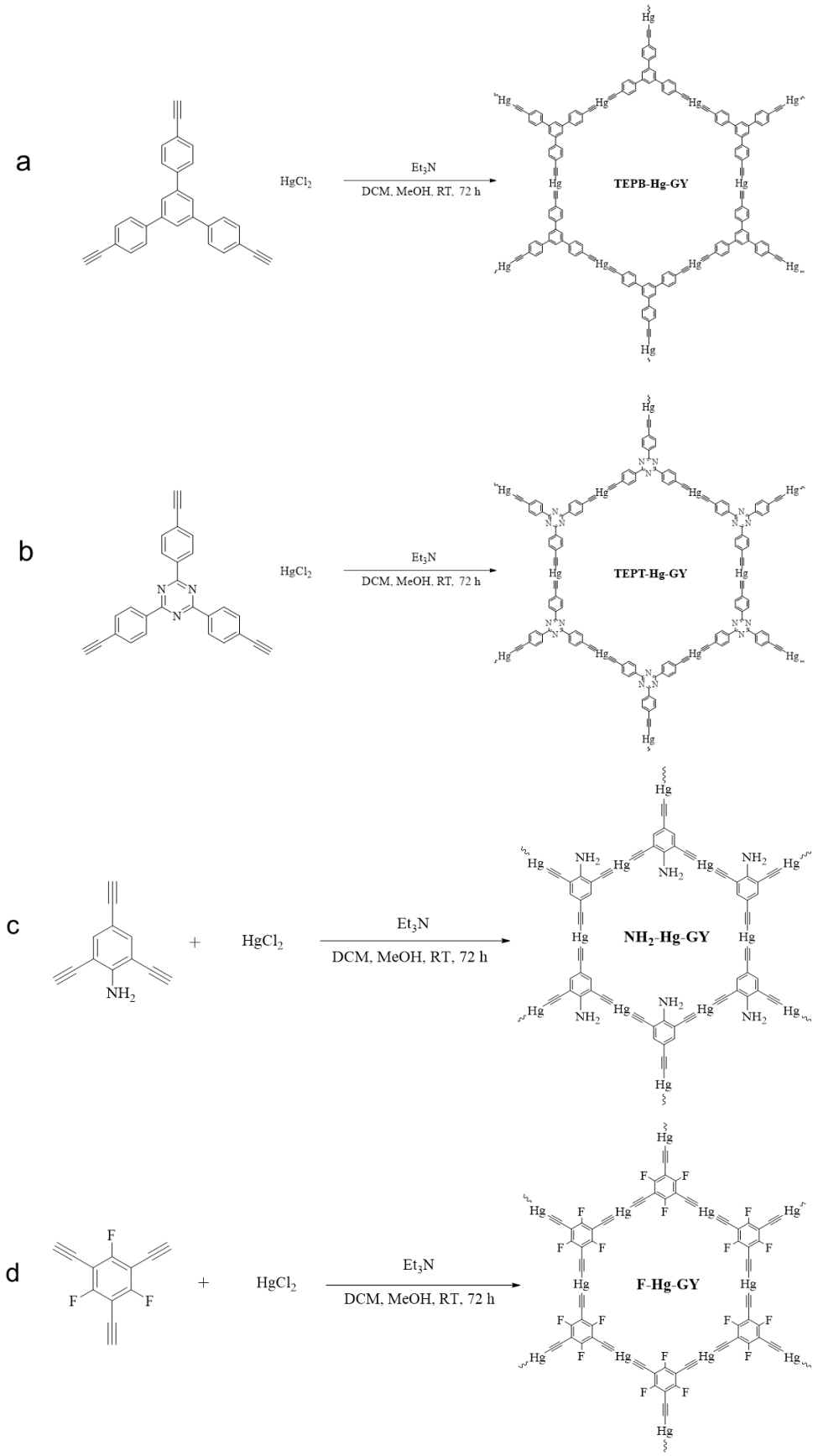

Figure 2.2 Synthetic routes of the Hg-GYs of (a) **TEPB-Hg-GY**, (b) **TEPT-Hg-GY**, (c) **NH_2-Hg-GY**, and (d) **F-Hg-GY**.

2.2.3 Characterization of mercury graphynes

The chemical structures of four Hg-GYs were characterized by FTIR, solid-^{13}C NMR and XPS spectroscopy as well as their crystal structures were characterized by the PXRD pattern, and their morphologies were characterized by TEM technique. FTIR spectra of **TEPB-Hg-GY**, **TEPT-Hg-GY**, **NH2-Hg-GY**, and **F-Hg-GY** and their corresponding organic ligands of **TEPB**, **TEPT**, **TEBA**, and **TEFB** were measured and are shown in Figure 2.3.

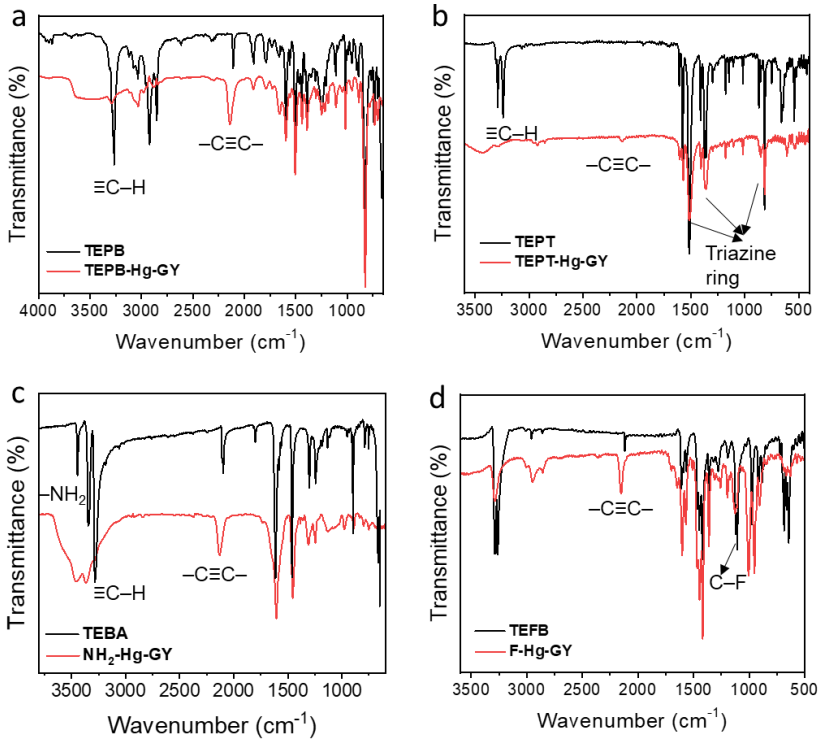

Figure 2.3 FTIR spectra of (a) **TEPB-Hg-GY**, (b) **TEPT-Hg-GY**, (c) **NH_2-Hg-GY**, and (d) **F-Hg-GY**.

It can be seen from all the FTIR spectra that the peaks at about 2133 cm^{-1} in the FTIR spectra of Hg-GYs showed the presence of –C≡C– bond. What's more, the sharp peaks at 3310–3070 cm^{-1} in the FTIR spectra of the organic ligands that were assigned to the ≡C–H stretching vibrations disappeared, which indicated that the metal alkynylation reactions occurred in the reaction[14]. In addition, for the **TEPT-Hg-GY**, the peaks corresponding to the stretching (1516 cm^{-1}), breathing (1359 cm^{-1}), and out-of-plane

ring bending (820 cm^{-1}) modes of the triazine ring are retained[29] (Figure 2.3b). The peaks at 3300-3400 cm^{-1} in the FTIR spectra of the **NH_2-Hg-GY** can be assigned to the typical absorption peaks of amine groups for its symmetrical and asymmetrical stretching vibration[30] (Figure 2.3b). For the **F-Hg-GY**, the semi-ionic C–F bond[31] was found at 1110 cm^{-1}. The above assignments indicated that the as-designed MGYs were successfully synthesized.

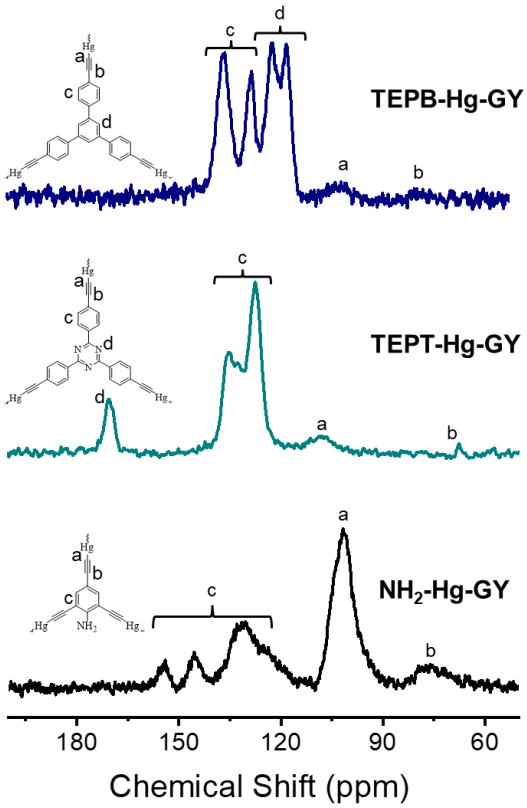

Figure 2.4 Solid-state ^{13}C NMR spectra of **TEPB-Hg-GY**, **TEPT-Hg-GY**, and **NH_2-Hg-GY**.

Furthermore, the ^{13}C cross-polarization magic-angle spinning NMR spectra of **TEPB-Hg-GY**, **TEPT-Hg-GY**, and **NH_2-Hg-GY** also confirmed their chemical structures, as shown in Figure 2.4. For all the Hg-GYs, the peaks at ≈ 75 and ≈ 105 ppm can be assigned to the carbon atoms in the –C≡C–Hg–C≡C– moieties[32]. What's more, the peaks in the range of 110–140 ppm of **TEPB-Hg-GY** can be attributed to the phenyl groups (Figure 1b)[33]. For **TEPT-Hg-GY**, the peak of 170.3 ppm can be assigned to the

triazine groups[29], while the peaks in the range of 120–160 ppm can be attributed to the amino-substituted aromatic ring[34]. The chemical states of the existing elements of **TEPB-Hg-GY**, **TEPT-Hg-GY**, **NH_2-Hg-GY**, and **F-Hg-GY** were confirmed by X-ray photoelectron spectra (XPS), as shown in Figure 2.5. It can be seen from all the full-range spectra that the binding energy of 101.88, 284.09, 360.86, and 380.76 eV can be ascribed to Hg(II) 4f, C 1s, and Hg(II) 3d, respectively[14]. In addition, the binding energy of 400.53 eV indicated the presence of the N 1s in **TEPT-Hg-GY** and **NH_2-Hg-GY** (Figure 2.5b and 2.5c)[34,35] and the binding energy of 687.68 eV in the curve of **F-Hg-GY** confirmed the element of F 1s (Figure 2.5d)[36]. Such assignments further proved the accurate structure of the four Hg-GYs.

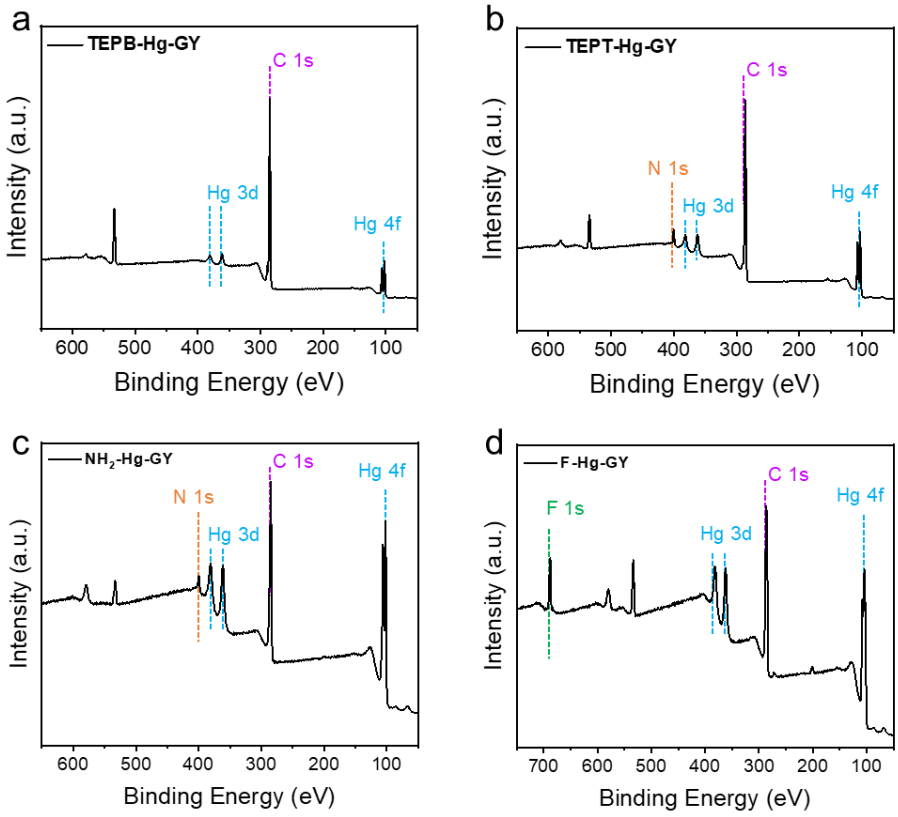

Figure 2.5 XPS curves of (a) **TEPB-Hg-GY**, (b) **TEPT-Hg-GY**, (c) **NH_2-Hg-GY**, and (d) **F-Hg-GY**.

To gain a deep understanding about the nature of **TEPB-Hg-GY**, **TEPT-Hg-GY**, **NH_2-Hg-GY**, and **F-Hg-GY**, their crystal structures were revealed by using powder X-ray diffraction (PXRD). As shown in Figure 2.6, **TEPB-Hg-GY** and **TEPT-Hg-GY** possess the same crystal form and the diffraction peaks at the 2θ angles of 5.6°, 10.6° were assigned to (100), (200) facets, respectively. **NH_2-Hg-GY** and **F-Hg-GY** possess another same crystal form and the diffraction peak at the 2θ angles of 10° can be assigned to (220) facet, which indicated that the organic ligands can have a big effect on the type of Hg-GY crystals. In addition, we can also see from the spectra that the intensity of patterns changes a lot, which reveals that the organic ligands can also have a big influence on their crystallinity. On the other hand, all the XRD patterns possess the same diffraction peak at the 2θ angle of ≈ 26° that can be assigned to the (001) facet[34], which corresponded to the interlayer distance of these Hg-GY crystals and indicated a long-range order of π-π stacking between the individual layers, which also showed that the organic ligands have similar interlayer distance.

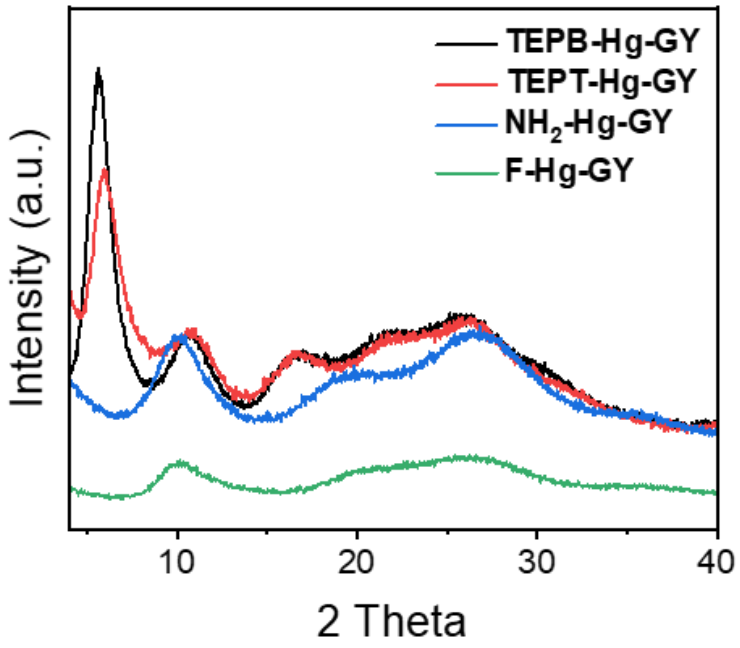

Figure 2.6 PXRD patterns of **TEPB-Hg-GY**, **TEPT-Hg-GY**, **NH_2-Hg-GY**, and **F-Hg-GY**.

The morphologies of **TEPB-Hg-GY**, **TEPT-Hg-GY**, **NH_2-Hg-GY**, and **F-Hg-GY** were confirmed by TEM images, as shown in Figure 2.7, which indicated that all Hg-GYs possess a layered structure. In addition, high resolution TEM (HRTEM) images (Figure 2.8) revealed that the interlayer distance of these Hg-GYs is ~3.40 Å, which matches well with the results from XRD diffraction peak corresponding to the (001) facet.

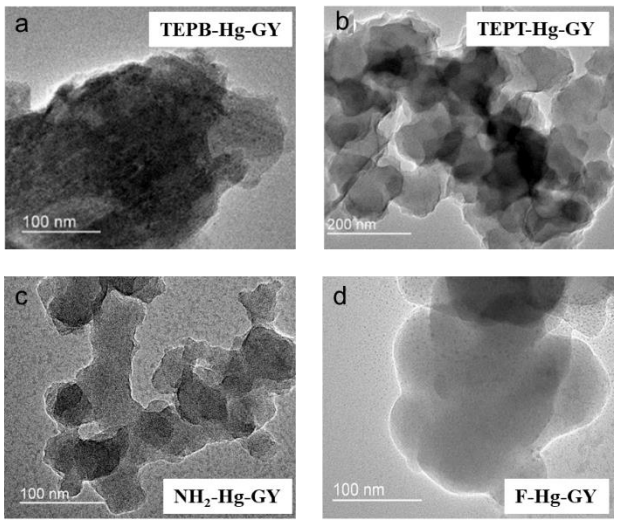

Figure 2.7 Large-scale TEM images of (a) **TEPB-Hg-GY**, (b) **TEPT-Hg-GY**, (c) **NH_2-Hg-GY**, and (d) **F-Hg-GY**.

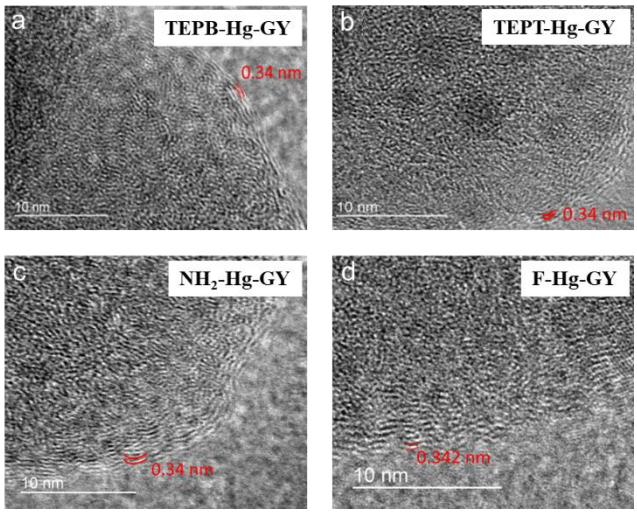

Figure 2.8 HRTEM images of (a) **TEPB-Hg-GY**, (b) **TEPT-Hg-GY**, (c) **NH_2-Hg-GY**, and (d) **F-Hg-GY**.

The thermal stability of **TEPB-Hg-GY**, **TEPT-Hg-GY**, **NH_2-Hg-GY**, and **F-Hg-GY** was analyzed by thermogravimetry analysis (TGA), as shown in Figure 2.9. The onset decomposition temperature of **TEPB-Hg-GY**, **TEPT-Hg-GY**, and **F-Hg-GY** is about 270 °C, indicating their good thermal stability, while that of **NH_2-Hg-GY** is slightly lower at about 240 °C.

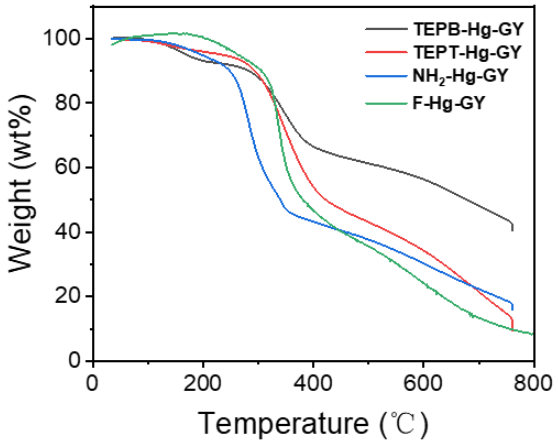

Figure 2.9 TGA curves of **TEPB-Hg-GY**, **TEPT-Hg-GY**, **NH_2-Hg-GY**, and **F-Hg-GY**.

2.3 Property studies of mercury graphynes

It is noted that the photocatalytic performance of materials is closely related to the type of semiconductor material and its valence band structure, which has an important role in their optical properties. Herein, we performed UV–Vis DRS, UPS, and M–S electrochemical measurements to investigate their semiconductor types and the band structures of **TEPB-Hg-GY**, **TEPT-Hg-GY**, **NH_2-Hg-GY**, and **F-Hg-GY**. As shown in Figure 2.10a, UV–Vis spectra showed that the introduction of reactive groups and heteroatoms can help improve the light absorption capability of Hg-GYs. What's more, the light absorption capacity of the four Hg-GYs follows the order **F-Hg-GY** < **TEPB-**

Hg-GY < **TEPT-Hg-GY** < **NH_2-Hg-GY**, which demonstrats that the amino groups and N heteroatoms can enhance the light absorption capacity while the amino groups can enhance even more, but F atoms slightly weaken its light absorption ability. Correspondingly, the Tauc's plots showed the optical band gap (E_g) of **TEPB-Hg-GY**, **TEPT-Hg-GY**, **NH_2-Hg-GY**, and **F-Hg-GY** is 3.52, 3.31, 2.67, and 3.55 eV, respectively (Figure 2.10b).

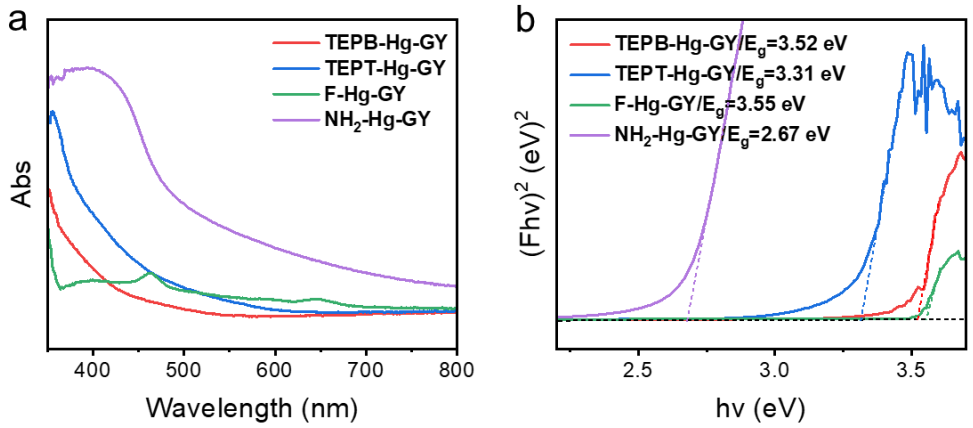

Figure 2.10 (a) UV−Vis spectra and (b) Tauc's plots of **TEPB-Hg-GY**, **TEPT-Hg-GY**, **NH_2-Hg-GY**, and **F-Hg-GY**.

Furthermore, UPS was conducted to study their valence band (VB) and conduction band (CB) positions (Figure 2.11). Combined with E_g calculated from UV−Vis DRS, E_{VBM} and E_{CBM} can be calculated by the following equations:

$$\Phi = E_{cutoff} - hv \quad (1)$$

$$E_{VBM} = \Phi - E_{edge} \quad (2)$$

$$E_g = E_{CBM} - E_{VBM} \quad (3)$$

where Φ is the work function, hv = 21.22 eV. As a result, the E_{CBM} of **TEPB-Hg-GY**, **TEPT-Hg-GY**, **NH_2-Hg-GY**, and **F-Hg-GY** were calculated to be –0.35, –0.7, –0.7, and –0.6 eV (vs. RHE), respectively. Meanwhile, their Corresponding E_{VBM} position is

3.17, 2.61, 1.96 and 2.95 eV (vs. NHE), respectively. Therefore, the corresponding band energy levels are displayed in Figure 2.12, which indicates that the introduction of active groups and heteroatoms can greatly reduce the potential of VB and slightly increase the potential of CB.

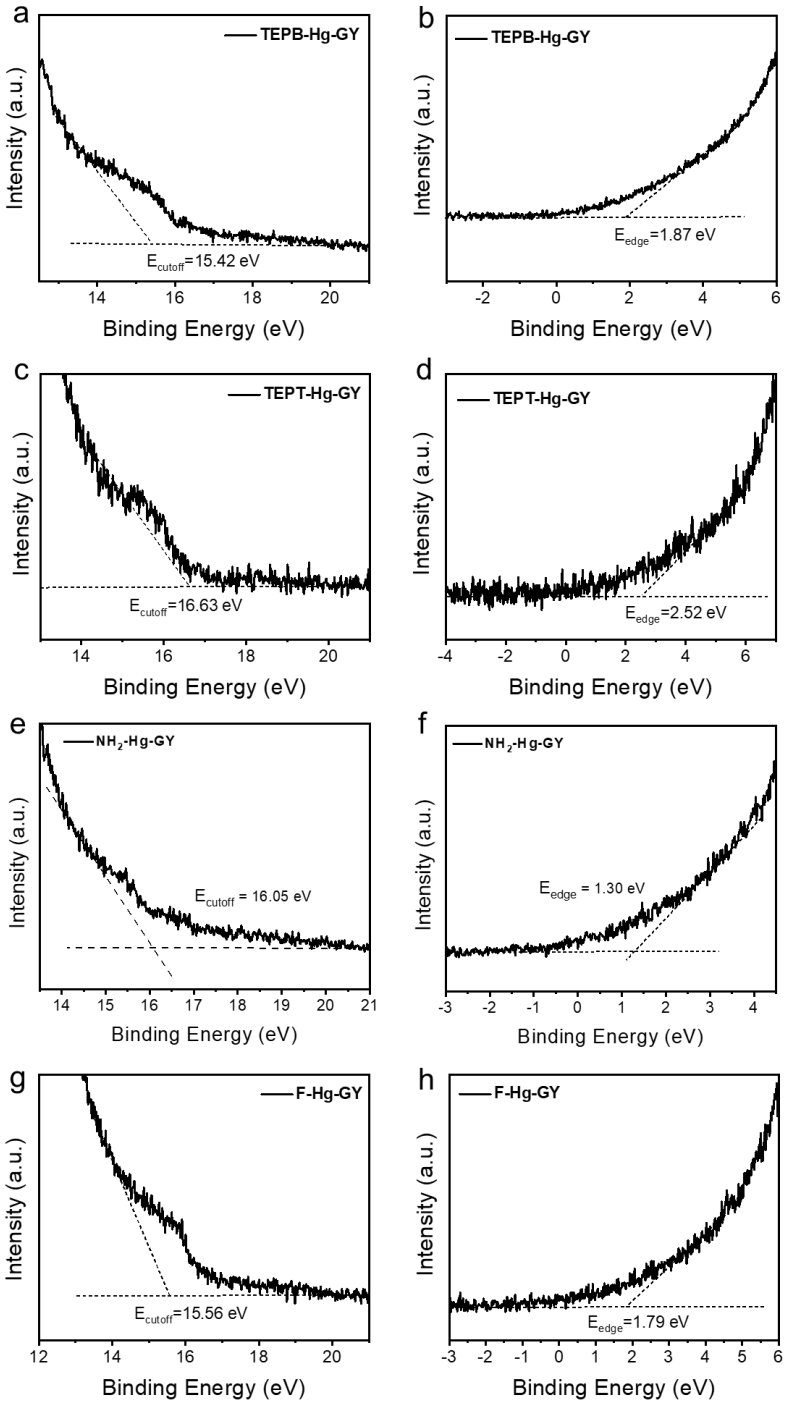

Figure 2.11 UPS of **TEPB-Hg-GY**, **TEPT-Hg-GY**, **NH_2-Hg-GY**, and **F-Hg-GY**.

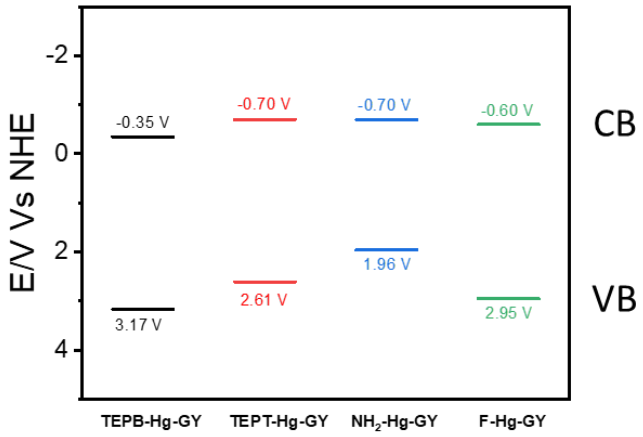

Figure 2.12 VB and CB positions of **TEPB-Hg-GY**, **TEPT-Hg-GY**, **NH_2-Hg-GY**, and **F-Hg-GY**.

M–S electrochemical measurements were performed to study their semiconductor types and further verified the energy level positions (Figure 2.13), which indicates that all the Hg-GYs are n-type semiconductor and their calculated CB potentials are consistent with that from UPS.

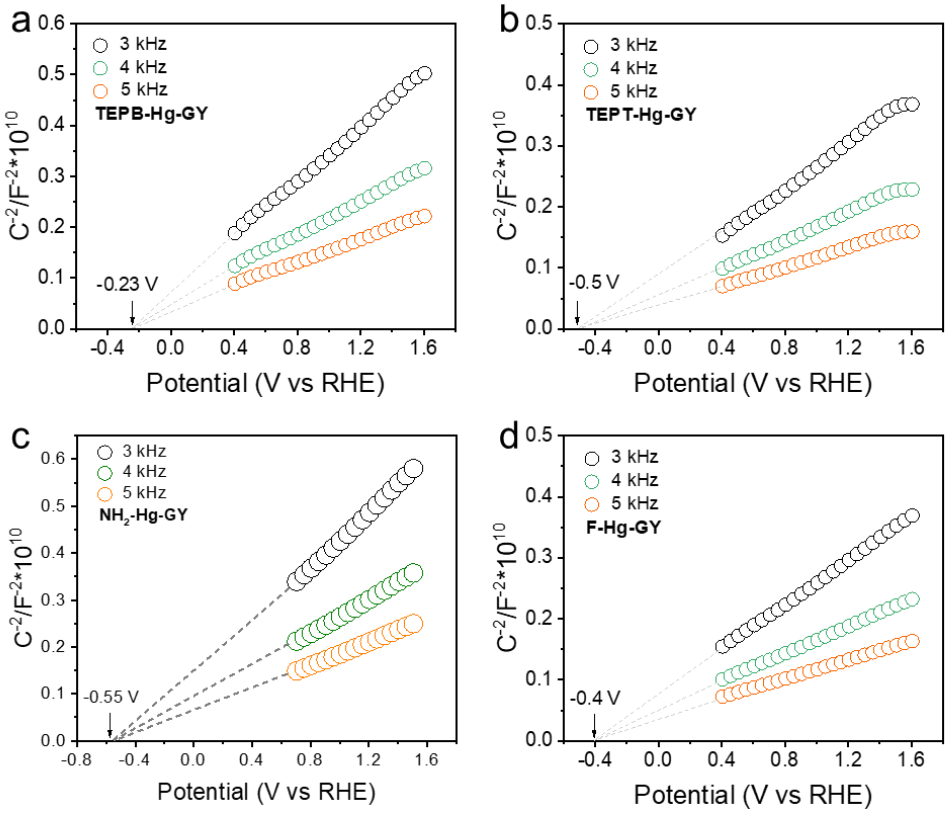

Figure 2.13 M–S curves of (a) **TEPB-Hg-GY**, (b) **TEPT-Hg-GY**, (c) **NH_2-Hg-GY**, and (d) **F-Hg-GY**.

To explore their optical and electrical properties, the transient-photocurrent-response (TPR) and electrochemical impedance spectroscopy (EIS) were conducted. TPR studies (Figure. 2.14a) showed that **NH_2-Hg-GY** and **TEPT-Hg-GY** have higher current intensity, indicating the more efficient electron-hole separation generation[37]. On the contrary, **TEPB-Hg-GY** and **F-Hg-GY** have almost no photo-response, perhaps because the band gaps of these two samples are too large. Moreover, it was found from EIS that **TEPT-Hg-GY**, **NH_2-Hg-GY**, and **F-Hg-GY** have superior electronic conductivity with smaller semicircles in the Nyquist plot than that of **TEPB-Hg-GY**, showing an enhanced charge transfer rate[38] and the fitting charge transfer rate (R_{ct}) of **TEPB-Hg-GY**, **TEPT-Hg-GY**, **NH_2-Hg-GY**, and **F-Hg-GY** is 49.63, 44.02, 35.27, and 40.05, respectively. (Figure. 2.14b). These results provide a solid evidence that the introduction of amino groups and heteroatoms can improve their photo-electric properties, which are closely related to the high efficiency of photocatalytic H_2O_2 production.

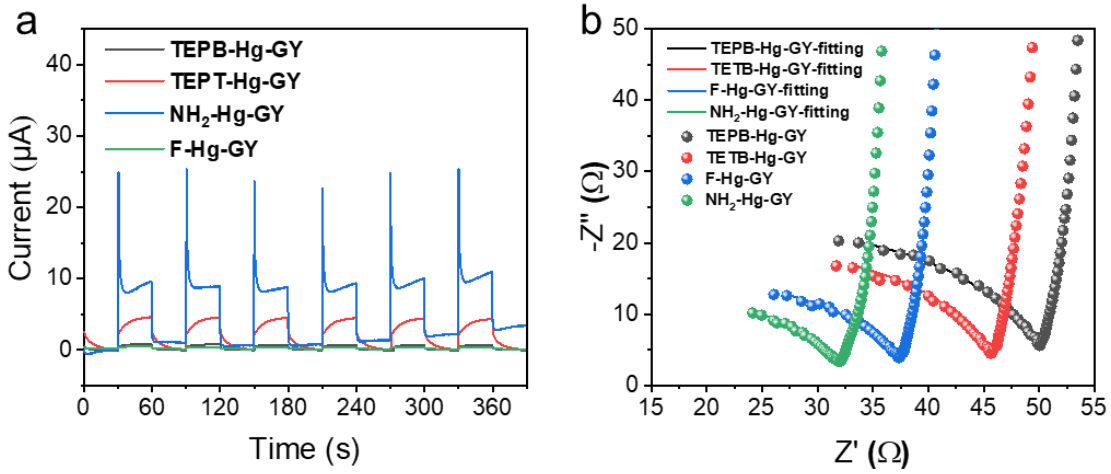

Figure 2.13 TPR and EIS curves of **TEPB-Hg-GY**, **TEPT-Hg-GY**, **NH_2-Hg-GY**, and **F-Hg-GY**.

2.4 Photocatalytic H_2O_2 production performance

We carried out photocatalytic experiments with pristine **TEPB-Hg-GY**, **TEPT-Hg-GY**, **NH_2-Hg-GY**, and **F-Hg-GY** in the pure-water and open-air condition under visible-light irradiation ($\lambda > 420$ nm) and found that only **NH_2-Hg-GY** exhibits a good performance for H_2O_2 photoproduction, which is consistent with their band structure. It can be known from DRS that **TEPB-Hg-GY**, **TEPT-Hg-GY**, and **F-Hg-GY** possess large band gaps so that the visible-light cannot excite them to participate in the photocatalytic reaction. To explore the mechanism of the entire photocatalytic H_2O_2 production, comprehensive characterizations were conducted with **NH_2-Hg-GY** and the control sample (**TEB-Hg-GY**) that has been reported in the previous literature[14]. As displayed in Figure 2.14a, no H_2O_2 was detected with TEB-Hg-GY catalyst, while **NH_2-Hg-GY** exhibited an outstanding photocatalytic yield. Remarkably, the concentration of H_2O_2 gradually increased in 24 h, showing a linear relationship with the first 12 h and the concentration reached up to nearly 425 μM h^{-1}. Hence, it is noted that the amino group plays a remarkable role in boosting the activity of H_2O_2 generation. Besides, the apparent quantum yield (AQY) of the photocatalysis of H_2O_2 was measured to be 3.26% at 365 nm and 1.86% at 420 nm, respectively (Figure 2.14b). Moreover, **NH_2-Hg-GY** exhibited good stability in photocatalytic performance toward photocatalytic H_2O_2 production during the cyclic tests (Figure 2.14c).

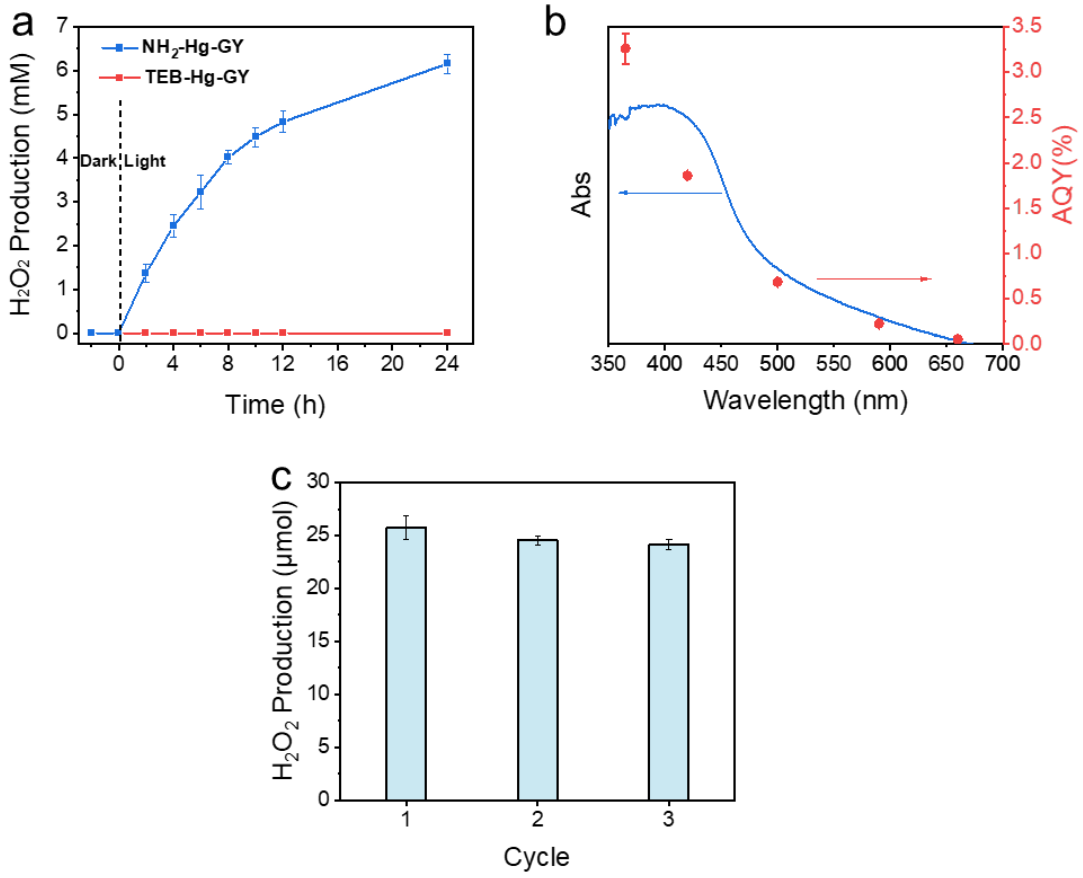

Figure 2.14 (a) Time-dependent H_2O_2 photogeneration using visible light for **NH_2-Hg-GY** and **TEB-Hg-GY**. (b) UV–Vis spectrum of **NH_2-Hg-GY** and AQY for H_2O_2 generation. (c) Repeatability performance of **NH_2-Hg-GY**.

To shed insights into the overall reaction process for H_2O_2 generation, a series of control experiments have been executed under different conditions (Figure 2.15a). The photocatalytic standard experiment was firstly conducted with air and showed that H_2O_2 can be generated in pure water. Then, the oxygen (O_2) control experiment with a higher yield of H_2O_2 indicated that the ORR pathway happened. On the other hand, the nitrogen (N_2) control experiment can prove that the WOR pathway happened. Otherwise, the residual oxygen would only produce a very small amount of H_2O_2. Moreover, it can also be concluded that there was still the ORR pathway in the N_2

control experiment because it's difficult to remove all the O_2 from the reaction system, which can also be shown from Figure 2.15b that O_2 was detected before the N_2 control experiment and the amount of the O_2 decreased after the experiment. Therefore, the electrons participated in the ORR. Finally, to rigorously determine whether a dual-channel process will occur, the $AgNO_3$ (Ag^+ as the electron acceptor) sacrificial agent experiment and the ethylenediaminetetraacetic acid (EDTA, as the hole acceptor) sacrificial agent experiment were conducted and the results verified that both the WOR and ORR process could occur with **NH_2-Hg-GY.** Accordingly, we can conclude that **NH_2-Hg-GY** can generate H_2O_2 through both ORR and WOR processes. Noteworthily, the yield of H_2O_2 in saturated O_2 can reach up to 2112.6 μmol h^{-1} g^{-1}, which is superior to the previous porous crystalline photocatalysts to date (listed in Table 2.1).

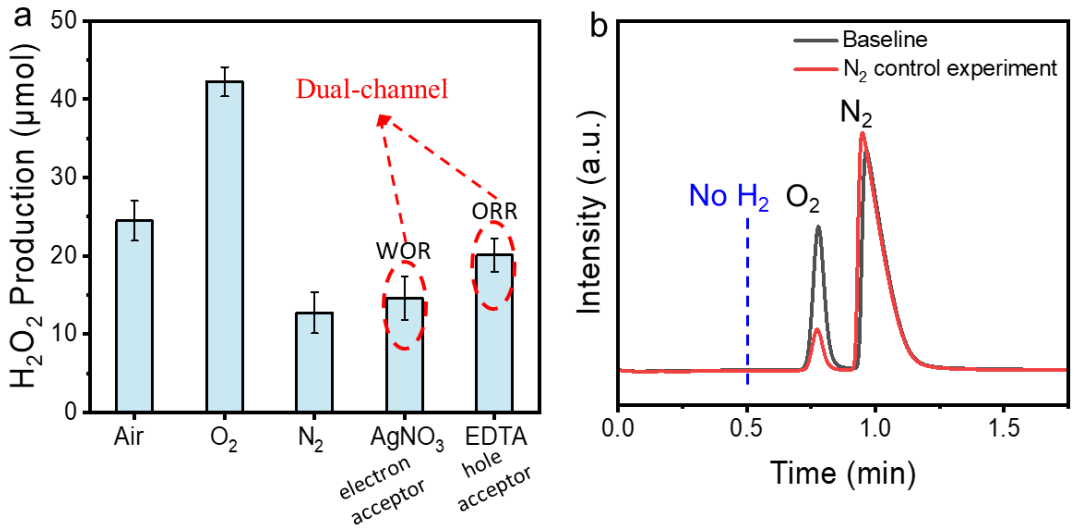

Figure 2.15 (a) H_2O_2 photogeneration using visible light for **NH_2-Hg-GY** under different conditions. (b) Gas chromatography of N_2 control experiment with **NH_2-Hg-GY**.

Table 2.1 Summary of the dual-channel pathway over semiconductors for H_2O_2 production.

Photocatalyst	Reaction and irradiation conditions	Catalyst dosage	H_2O_2 activity	Ref.
CN/PI composite	H_2O (O_2) Vis (λ > 420 nm)	50 mg/50 ml	1200 μmol h^{-1} g^{-1}	39
g-C_3N_4/CuO	H_2O (Bubbled O_2) Vis (400–800 nm)	200 mg/200 ml	1100 μmol h^{-1} g^{-1}	40
MoO_3/SnS_2	H_2O (O_2) Solar simulator	50 mg/100 ml	1200 μmol h^{-1} g^{-1}	41
OCN	H_2O (Bubbled O_2) Vis (400–800 nm)	200 mg/200 ml	633 μmol h^{-1} g^{-1}	42
Carbon-supported oxygen vacancy-rich Co_3O_4	H_2O (O_2-equilibrium) Vis (λ > 420 nm)	20 mg/20 ml	3784.5 μmol $h^{-1}g^{-1}$	43
WO_3/TiO_2	H_2O (O_2) with $AgNO_3$ or $Mn(NO_3)_2$ Simulated solar	10 mg/10 ml	1.67 μmol h^{-1} g^{-1}	44
CTF-BPDCN	H_2O (O_2) Vis (λ > 420 nm)	30 mg/50 ml	97.2 μmol h^{-1} g^{-1}	45
$Bi_4O_5Br_2$/g-C_3N_4	H_2O (O_2-equilibrium) Vis (λ > 420 nm)	50 mg/50 ml	124 μmol h^{-1} g^{-1}	46
ZIF-8/g-C_3N_4	H_2O (O_2) Vis (400–700 nm)	10 mg/15 ml	2641 μmol h^{-1} g^{-1}	47
ZnPPc/NBCN	H_2O (O_2) 400–800 nm	10 mg/20 ml	114 μmol h^{-1} g^{-1}	48
Covalent triazine frameworks (NMT400)	H_2O (O_2) Vis (λ > 420 nm)	20 mg/50 ml	270.9 μmol h^{-1} g^{-1}	49
COF-TpBpy	H_2O (Air) λ > 420 nm	5 mg/10 ml	2084 μmol h^{-1} g^{-1}	50
CHF-DPDA	H_2O (O_2) Vis (λ > 420 nm)	40 mg/20 ml	1725 μmol h^{-1} g^{-1}	51
NH_2-Hg-GY	H_2O (O_2) Vis (λ > 420 nm)	10 mg/15 ml	2112.6 μmol $h^{-1}g^{-1}$	This work

To further explore the mechanism of the reaction pathways of H_2O_2 photoproduction with **NH_2-Hg-GY**, *in-situ* electron paramagnetic resonance (EPR) spectroscopy was characterized with 5,5-dimethylpyrroline N-oxide (DMPO) as a free

radical spin-trap agent to detect the intermediates of superoxide radicals (•OOH) or hydroxyl radicals (•OH)[52]. As displayed in Figure. 2.15a, the typical characteristic signals of DMPO-•OOH were obviously observed in **NH_2-Hg-GY** under light irradiation and the intensity kept increasing over time. Thus, it can be concluded that the ORR pathway for H_2O_2 photoproduction is a two-step $2e^-$ process. By contrast, DMPO-•OH spin adducts were not detected, declaring that the two-step $2h^+$ process for WOR pathway is excluded (Figure 2.15b). DFT calculations and *in-situ* diffuse reflectance infrared Fourier transform spectroscopy (DRIFTS) measurements were further used to confirm the reaction pathways and active sites in the framework of **NH_2-Hg-GY**[53,54]. According to the above results, *OOH intermediate species are generated in the ORR pathway and their formation is the rate-determined step. As shown in Figure. 2.15c, the benzene ring showed the most favorable Gibbs free energy change (ΔG) than the other sites, indicating that the benzene ring has the biggest possibility to be the active site for the ORR pathway. Furthermore, *in-situ* DRIFTS displayed that the benzene ring vibrations (1588, 1485, 1420 cm^{-1})[55] of **NH_2-Hg-GY** occurred after 30 min absorption with O_2 and D_2O vapor and kept increasing with irradiation time, thus confirming that the benzene ring act as the adsorption site for O_2 and the reaction site for ORR pathway (Figure 2.15e). On the other side, DFT calculations indicated that the acetylene moiety exhibits the smallest ΔG to form *OH compared to the other sites (Figure 2.15d). Similarly, *in-situ* DRIFTS (Figure 2.15f) showed that the stretching vibration of the –C≡C– bond at 2150 cm^{-1} emerged after 30 min absorption of argon

and H_2O vapor and maintained increasing over time, which proves the hypothesis that the acetylene moiety is the reaction site of the WOR pathway[56].

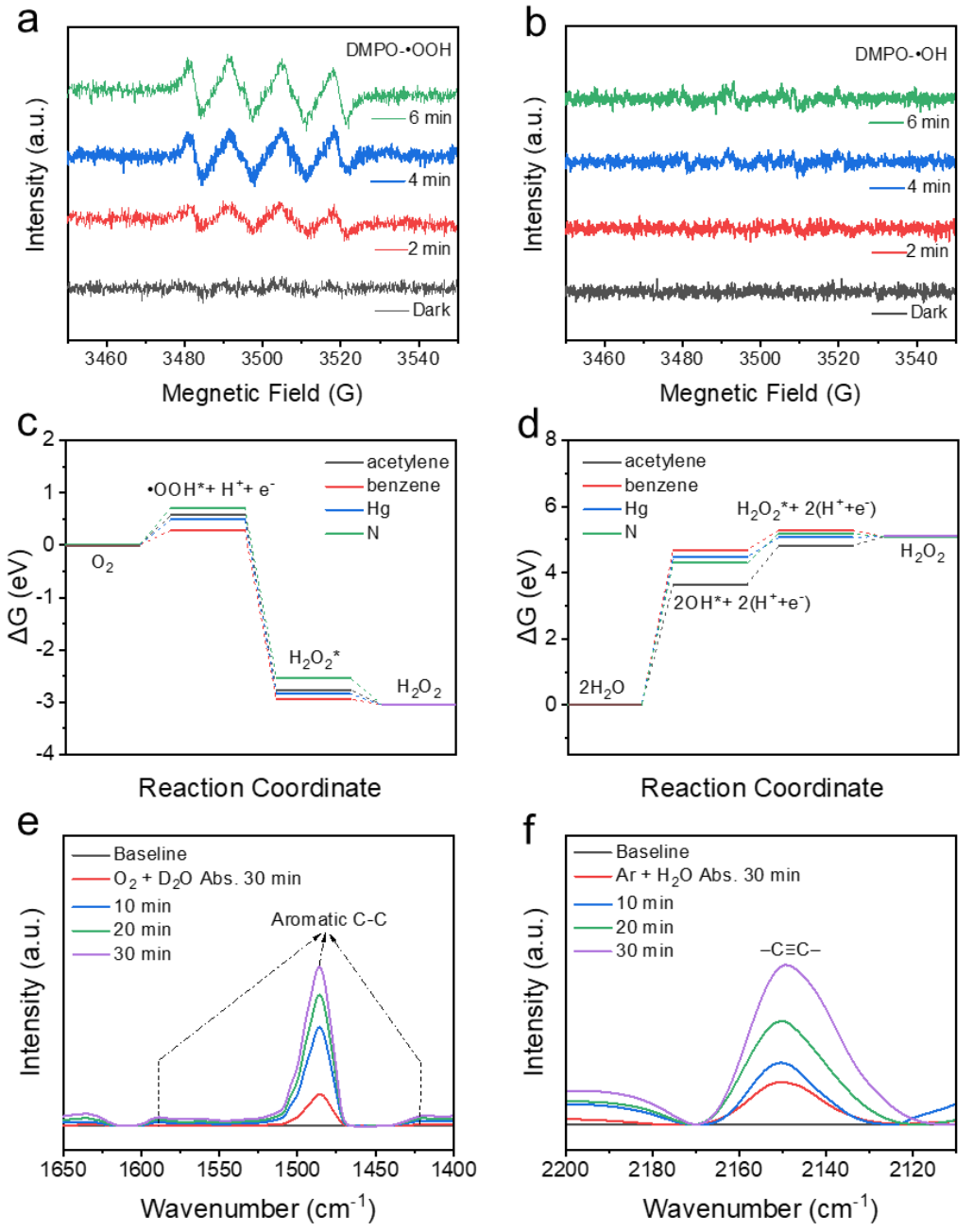

Figure 2.15 (a) *In-situ* EPR signals of DMPO-•OOH under the dark and visible light illumination with **NH_2-Hg-GY**. (b) *In-situ* EPR signals of DMPO-•OH under the dark and visible light illumination with **NH_2-Hg-GY**. (c) Calculated free energy diagrams of ORR pathway toward H_2O_2 production on different active sites in **NH_2-Hg-GY**. (d) Calculated free energy diagrams of WOR pathway toward H_2O_2 production on different active sites in **NH_2-Hg-GY**. (e) *In-situ* DRIFT spectra of ORR pathway during

photocatalytic H_2O_2 evolution. (f) *In-situ* DRIFT spectra of WOR pathway during photocatalytic H_2O_2 evolution.

Together with the improved light absorption, the enhanced photocatalytic activity of the **NH_2-Hg-GY** sample may originate from the controllable charge migration of efficient charge separation and surface trapping[57,58]. To study the excited state dynamics, femtosecond transient absorption spectroscopy (fs-TA) was carried out. At 360 nm excitation (upper panel in Figures 2.16a and 2.16b), both TA spectra exhibited a broad photoinduced absorption (PA) band with a quite long lifetime, covering most of the visible and entire near-infrared (Vis-NIR) regions. The overall PA band intensity for **NH_2-Hg-GY** was higher than that of TEB-Hg-GY, indicating more efficient population of trapped carriers are generated in **NH_2-Hg-GY** even at very earlier stage[59]. In addition, **NH_2-Hg-GY** showed a relatively weak positive $\Delta T/T$ signal at the bandgap region, which represented a reduced probability of band-to-band recombination of the photoexcited carriers, thus achieving more efficient photogenerated charge separation in **NH_2-Hg-GY**[60]. Interestingly, the PA band changed its shape in the visible spectral range, while kept almost unchanged in the infrared range (Figure 2.16a and 2.16b). This phenomenon indicated the existence of at least two distinct populated states after photoexcitation, which implies a dual-channel separated mechanism (volume separation and surface separation) of the photogenerated charges[61-63].

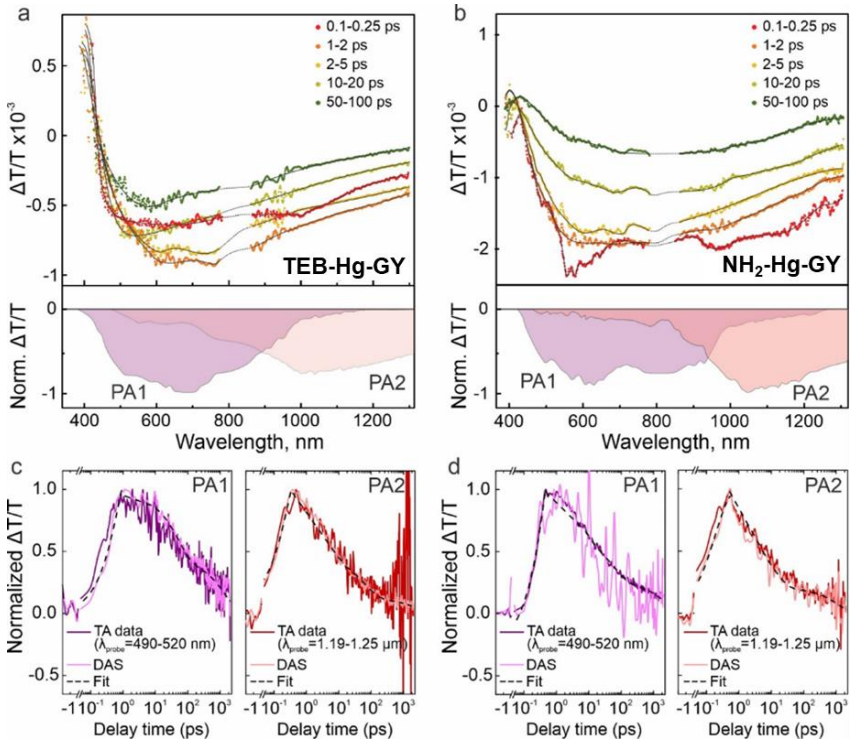

Figure 2.16 Vis-NIR transient absorption studies of (a, c) **TEB-Hg-GY** and (b, d) **NH_2-Hg-GY**. (a, b) Transient absorption spectra collected at different delay times after photoexcitation (upper panel) and decay-associated spectra (DAS) obtained through SVD of the entire spectral range (bottom panel). (c, d) TA kinetics probed at the maxima of PA1 and PA2 bands (data), obtained from decay-associated spectra (DAS), and their fit with tri-exponential function.

Comprehensive fitting and TA kinetics studies were performed to reveal the underlying attributes of the two distinct populated states and charge migration. The TA spectra (bottom panels in Figure 2.16a and 2.16b) returned two PA sub-bands (denoted as PA1, $\lambda_{max} \approx 700$ nm and PA2, $\lambda_{max} \approx 1050$ nm) in the Vis-NIR regions. In addition, TA kinetics probed at 490–520 nm and 1190–1250 nm ranges also matched well with the kinetics extracted from SVD (Figure 2.16c and 2.16d). What's more, the kinetics revealed that the build-up time (τ_{rise}) for the PA1 band is noticeably longer than that of the PA2 band, allowing us to attribute the PA1 band to the photoexcited carriers trapping

on surface defects because the amplitude of PA1 sub-band is positively correlated with photocatalytic performance and such carriers play a crucial role in the catalytic reaction, while the PA2 band can be attributed to the carriers trapping on volume defects which may be presented in the area between the stacked nanosheets[63,64] (Table 1). On the other hand, the fitting of PA sub-bands decay with a bi-exponential function of fast (τ_{decay1}) and slow (τ_{decay2}) components for the PA sub-bands (Table1). For the PA1 band, the τ_{decay1} component can be attributed to a decrease in the population of trapped surface carriers due to their participation in photocatalytic reaction, while the τ_{decay2} component corresponds to the overall lifetime of the trapped carriers (before they either recombine to the valence band or transfer to the surrounding species). Additionally, the **NH_2-Hg-GY** sample demonstrated much faster τ_{decay1} than that of Hg-GY, which clearly stated that **NH_2-Hg-GY** possessed a higher surface charge transfer rate, matching well with the result of EIS. For the PA2 band, the decay can be governed by two processes: the relaxation of the carriers trapped between stacked nanosheets back to the valence band or their transfer to the surface state. Although the latter process is less common in photocatalysis as the control of dual-channels modification separation is hard to be achieved[58,63], the TA kinetics showed that the τ_{decay1} component of PA2 band corresponded well with the formation time of the PA1 band, indicating the possibility of the latter process[65-67]. Such investigations of dual-channel separation mechanisms can shift a new sight in the study of controllable carrier migration. The comparison of the rates and lifetimes estimated for **TEB-Hg-GY** and **NH_2-Hg-GY** samples proves

that the introduction of amino groups into mercury graphyne framework is beneficial to generate extra carrier trapping sites, controllable charge migration, and enhanced charge separation efficiency to facilitate H_2O_2 photoproduction.

Table 1. The fitted parameters for TA kinetics probed in the spectral ranges corresponding to the ground-state bleach (GSB), and photoinduced absorption bands (PA1 and PA2).

Band/probe range	Fitted parameter	**TEB-Hg-GY**	**NH_2- Hg-GY**
PA1 (490-520 nm)	τ_{rise}, ps	1.17±0.01	0.84±0.01
	τ_{decay1}, ps (Rel Amp)	47.2±3 (51.9%)	18.72±0.6 (57.9%)
	τ_{decay2}, ps (Rel Amp)	1375±90 (42.7%)	1414±70 (31.2%)
PA2 (1190-1250 nm)	τ_{rise}	0.38±0.01	0.52±0.01
	τ_{decay1}, ps (Rel Amp)	7.36±0.3 (67.2%)	5.45±0.4 (56.7%)
	τ_{decay2}, ps (Rel Amp)	531±30 (26.6%)	836±80 (23.3%)
GSB (380-420 nm)	τ_{rise}	NA	NA
	τ_{decay}, ps	>2000	>2000

To explore the origins of superior performance of **NH_2-Hg-GY** toward photoproduction of H_2O_2, three models of **TEB-Hg-GY**, **NH_2-Hg-GY**, and **NH_2-GY** were built to conduct DFT calculation on their band structure, density of states (DOS), and excited charge distribution. Calculated band structures ((Figures 2.17a–2.17c) clearly revealed that compared to **TEB-Hg-GY** and **NH_2-GY**, **NH_2-Hg-GY** had the most suitable band energy landscape covering both energy potential of $O_2/\bullet O_2^-$ and H_2O/H_2O_2, indicating that both amino groups and Hg(II) ions effectively optimize the energy level of framework. Furthermore, DOS calculation (Figure 2.17d–2.17f) revealed clearly that the amino group mostly contributes to VB and reduces its potential, while mercury affects the CB and increases its potential. Charge distribution images

further declared that excited electrons are concentrated in the benzene ring while the holes are mostly localized on the acetylene moiety in the excited state, demonstrating that the amino group improves the controllability of charge migration and charge separation efficiency in **NH_2-Hg-GY**. In addition, one can also see that Hg(II) ions can effectively break the electron delocalization on acetylene. The above characteristics may originate from the induction effect of amino groups as auxochromes and the conjugation effect of the blocks of Hg(II) alkynyl. Accordingly, we can conclude that amino groups and Hg(II) ions can effectively modify the electronic structure of **NH_2-Hg-GY** and lead to the improvement of photoinduced activities toward H_2O_2 photoproduction.

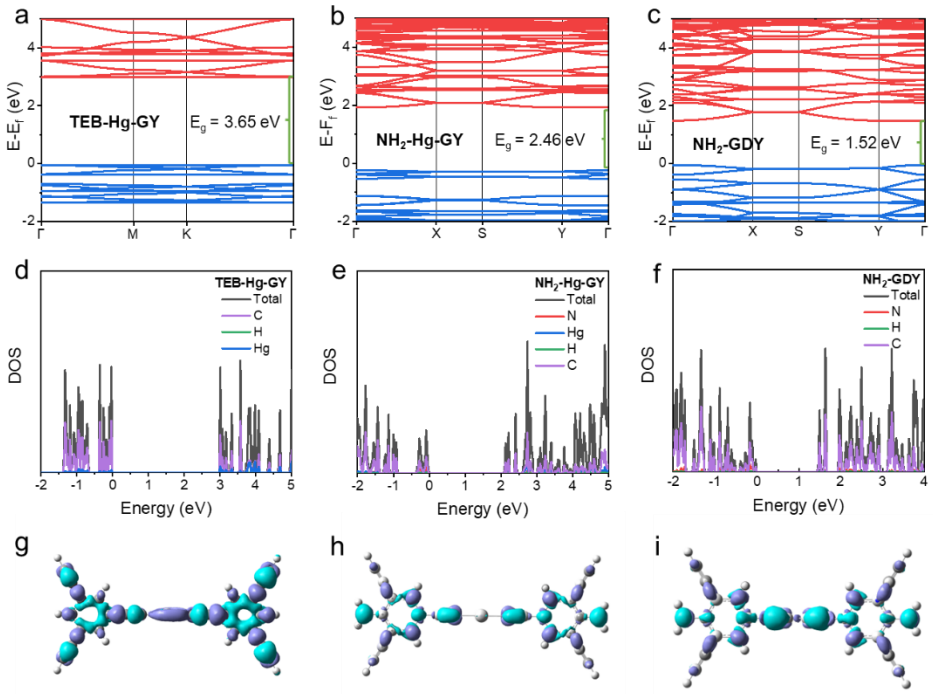

Figure 2.17 Band structure of (a) **TEB-Hg-GY**, (b) **NH_2-Hg-GY**, and (c) **NH_2-GY** model**.** Density of states (DOS) of (d) **TEB-Hg-GY**, (e) **NH_2-Hg-GY**, and (f) **NH_2-GY** model. The excited charge distribution of (g) **TEB-Hg-GY**, (h) **NH_2-Hg-GY**, and (i) **NH_2-GY** model.

Finally, we proposed a possible mechanism of the photocatalytic H_2O_2 production with **NH_2-Hg-GY**, as illustrated in Figure 2.18. Photogenerated electrons and holes are generated in the **NH_2-Hg-GY** catalyst with the characteristics of dual-channels separation dynamics. Upon transferring to surface defects, electrons then gather in the benzene ring, while holes accumulate on the acetylene bond. Finally, they participate in the ORR and WOR processes on the benzene ring and acetylene bond, respectively.

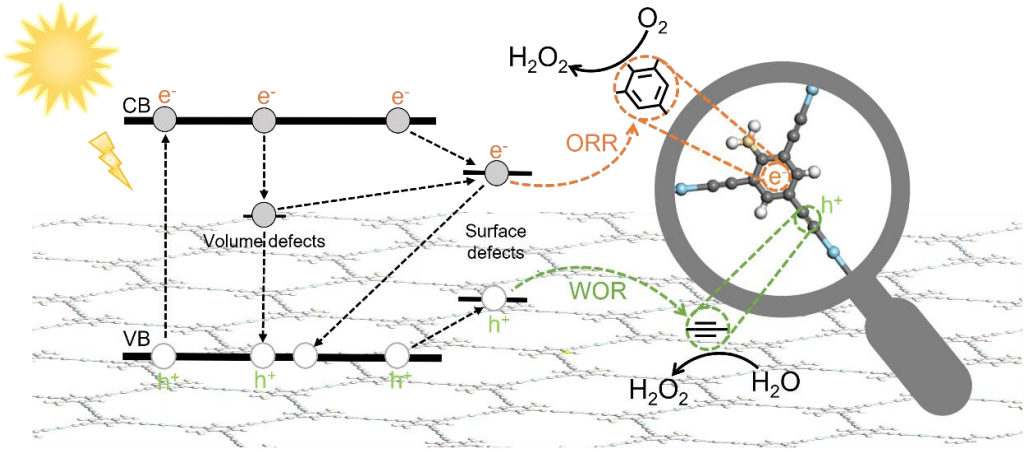

Figure 2.18 Schematic illustration of the proposed mechanism of photocatalytic H_2O_2 production in **NH_2-Hg-GY**.

2.5 Conclusion

In summary, a series of Hg-GYs of **TEPB-Hg-GY**, **TEPT-Hg-GY**, **NH_2-Hg-GY**, and **F-Hg-GY** were successfully synthesized. Firstly, their chemical structures were characterized by the FTIR, solid-state ^{13}C-NMR and XPS spectroscopy, indicating that the selected functional groups and elements were introduced in the MGY frameworks as designed. Secondly, the crystal structure details and morphologies were demonstrated from PXRD patterns and TEM images. Therefore, it can be concluded that these four Hg-GY materials have layered structures. Thirdly, their optical properties,

electronic properties, and band structures were characterized by using UV–Vis DRS, UPS, M–S electrochemical measurements, TPR, and EIS, which revealed that the introduction of active groups and heteroatoms can efficiently adjust their electronic properties. Finally, we conducted photoinduced H_2O_2 production experiments and found that the **NH_2-Hg-GY** integrate both ORR and WOR active sites toward overall photoinduced H_2O_2 production. It is worth mentioning that it can reach a relatively high production rate of 2112.6 μmol h^{-1} g^{-1} for the photoproduction of H_2O_2 in pure water without sacrificial agents. Such rational design enables **NH_2-Hg-GY** to possess a higher ability for visible-light adsorption, a good controllability of charge migration, and a suitable redox potential toward H_2O_2 production, which have been confirmed by both experiments and theoretical calculations. Interestingly, comprehensive investigations on the dynamic of the photoexcited carriers reveal a possible dual-channel separation pathway, providing a new perspective to future research. These results may be derived from the synergy of the inductive effect of the amino group and the conjugation effect of the blocks of Hg(II) alkynyl. This is the first work about MGYs that can achieve overall photocatalytic H_2O_2 production, shedding fresh light on the rational design of efficient photocatalysts. We believe that MGYs have a great potential to be developed into a class of functional semiconductors in artificial photosynthesis or some other optoelectronic devices.

References

1. Li, G., Li, Y., Liu, H., Guo, Y., Li, Y. & Zhu, D. Architecture of Graphdiyne Nanoscale Films. *Chem. Commun.* **46**, 3256–3258 (2010).
2. Li, Y., Xu, L., Liu, H. & Li, Y. Graphdiyne and Graphyne: From Theoretical Predictions to Practical Construction. *Chem. Soc. Rev.* **43**, 2572–2586 (2014).
3. Hui, L., Xue, Y., Yu, H., Liu, Y., Fang, Y., Xing, C. & Li, Y. Highly Efficient and Selective Generation of Ammonia and Hydrogen on a Graphdiyne-Based Catalyst. *J. Am. Chem. Soc.* **141**, 10677–10683 (2019).
4. Wang, L., Qi, L., Zhang, Q., Xue, B., Zheng, Z., Yin, P. & Li, Y. Scalable Synthesis of Soluble Crystalline Ionic-Graphdiyne by Controlled Ion Expansion. *Chem. Sci.* **14**, 4612–4619 (2023).
5. Shi, G., Xie, Y., Du, L., Fu, X., Chen, X., Xie, W. & Wang, M. Constructing Cu−C Bonds in a Graphdiyne-Regulated Cu Single-Atom Electrocatalyst for CO_2 Reduction to CH_4. *Angew. Chem. Int. Ed.* **134**, e202203569 (2022).
6. Guo, M., Ji, M. & Cui, W. Theoretical Investigation of HER/OER/ORR Catalytic Activity of Single Atom-Decorated Graphyne by DFT and Comparative DOS Analyses. *Appl. Surf. Sci.* **592**, 153237 (2022).
7. Fan, T., Chen, H. & Ji, Y. Graphdiyne Supported Single-Atom Cobalt Catalyst for Oxygen Reduction Reaction: The Role of the Co-Adsorbates. *Chem. Phys. Lett.* **804**, 139805 (2022).
8. Wang, Y., Mao, J., Meng, X., Yu, L., Deng, D. & Bao, X. Catalysis with Two-

Dimensional Materials Confining Single Atoms: Concept, Design, and Applications. *Chem. Rev.* **119**, 1806–1854 (2018).

9. Yang, Z., Gebhardt, J., Schaub, T. A., Sander, T., Schönamsgruber, J., Soni, H. & Maier, S. Two-Dimensional Delocalized States in Organometallic Bis-Acetylide Networks on Ag (111). *Nanoscale* **10**, 3769–3776 (2018).
10. Yang, Z., Sander, T., Gebhardt, J., Schaub, T. A., Schonamsgruber, J., Soni, H. R. & Maier, S. Metalated Graphyne-Based Networks as Two-Dimensional Materials: Crystallization, Topological Defects, Delocalized Electronic States, and Site-Specific Doping. *ACS Nano* **14,** 16887–16896. (2020).
11. Zhang, Y. Q., Paintner, T., Hellwig, R., Haag, F., Allegretti, F., Feulner, P. & Klappenberger, F. Synthesizing Highly Regular Single-Layer Alkynyl-Silver Networks at the Micrometer Scale via Gas-Mediated Surface Reaction. *J. Am. Chem. Soc.* **141**, 5087–5091 (2019).
12. Liu, J., Chen, Q., Cai, K., Li, J., Li, Y., Yang, X. & Wu, K. Stepwise On-surface Dissymmetric Reaction to Construct Binodal Organometallic Network. *Nat. Commun.* **10**, 2545 (2019).
13. Zhan, X., Kang, H., Qian, F., Xu, L., Zheng, Y. & Huang, Z. Magnetic Investigation on the Two-Dimensional Metallated Graphdiyne Nanosheets. *J. Alloys Compd.* **940,** 168693 (2023).
14. Xu, L., Sun, J., Tang, T., Zhang, H., Sun, M., Zhang, J. & Wong, W. Y. Metallated Graphynes as a New Class of Photofunctional 2D Organometallic Nanosheets.

Angew. Chem. Int. Ed. **60**, 11326–11334 (2021).

15. Zhang, T., Xu, S., Hou, Y., Chai, G., Olianas, D., Liao, Z. & Feng, X. Solvent-Mediated Engineering of Copper-Metalated Acetylenic Polymer Scaffolds with Enhanced Photoelectrochemical Performance. *J. Mater. Chem. A* **9**, 9729–9734 (2021).
16. Zhao, Y., Xu, L., Wang, X., Wang, Z., Liu, Y., Wang, Y. & Kang, Z. A Comprehensive Understanding on the Roles of Carbon Dots in Metallated Graphyne Based Catalyst for Photoinduced H_2O_2 Production. *Nano Today* **43,** 101428 (2022).
17. Fang, M., Xu, L., Zhang, H., Zhu, Y. & Wong, W. Y. Metalloporphyrin-Linked Mercurated Graphynes for Ultrastable CO_2 Electroreduction to CO with nearly 100% Selectivity at a Current Density of 1.2 A cm^{-2}. *J. Am. Chem. Soc.* **144**, 15143–15154 (2022).
18. Bai, J., Sun, Y., Li, M., Yang, L., Li, J. & Hu, S. "Two Channel" Photocatalytic Hydrogen Peroxide Production Using g-C_3N_4 Coated CuO Nanorod Heterojunction Catalysts Prepared via a Novel Molten Salt-Assisted Microwave Process. *New J. Chem.* **42**, 13529–13535 (2018).
19. Wang, H., Guan, Y., Hu, S., Pei, Y., Ma, W. & Fan, Z. Hydrothermal Synthesis of Band Gap-Tunable Oxygen-Doped g-C_3N_4 with Outstanding "Two-Channel" Photocatalytic H_2O_2 Production Ability Assisted by Dissolution–Precipitation Process. *Nano* **14,** 1950023 (2019).

20. Yang, L., Dong, G., Jacobs, D. L., Wang, Y., Zang, L. & Wang, C. Two-Channel Photocatalytic Production of H_2O_2 Over g-C_3N_4 Nanosheets Modified with Perylene Imides. *J. Catal.* **352**, 274–281 (2017).

21. Zeng, X., Liu, Y., Hu, X. & Zhang, X. Photoredox Catalysis over Semiconductors for Light-Driven Hydrogen Peroxide Production. *Green Chem.* **23**, 1466–1494 (2021).

22. Chen, W. *Phosphorus and Nitrogen Dual-doped Graphene Oxide as Metal-free Catalyst for Hydrogen Evolution Reaction*. National Central University (2020).

23. Luo, S., Hu, J., Guo, S., Yu, D., Dong, P., Xu, M. & Zhang, Y. Ionic Liquid-Derived Fe, N, S, F Multiple Heteroatom-Doped Carbon Materials for Enhanced Oxygen Reduction Reaction. *Nanotechnol.* **32**, 395701 (2021).

24. Witomska, S., Liu, Z., Czepa, W., Aliprandi, A., Pakulski, D., Pawluć, P. & Samorì, P. Graphene Oxide Hybrid with Sulfur–Nitrogen Polymer for High-Performance Pseudocapacitors. *J. Am. Chem. Soc.* **141**, 482–487 (2018).

25. Song, X., Johnson, A. & Foley, J. 7-Azabicyclo [2.2.1] Heptane as a Unique and Effective Dialkylamino Autochrome Moiety: Demonstration in a Fluorescent Rhodamine Dye. *J. Am. Chem. Soc.* **130**, 17652–17653 (2008).

26. Lv, X., Gao, C., Han, T., Shi, H. & Guo, W. Improving the Quantum Yields of Fluorophores by Inhibiting Twisted Intramolecular Charge Transfer Using Electron-Withdrawing Group-Functionalized Piperidine Auxochromes. *Chem. Commun.* **56**, 715–718 (2020).

27. Jedrzejewska, B., Skotnicka, A., Laurent, A. D., Pietrzak, M., Jacquemin, D. & Ośmiałowski, B. Influence of the Nature of the Amino Group in Highly Fluorescent Difluoroborates Exhibiting Intramolecular Charge Transfer. *J. Org. Chem.* **83**, 7779–7788 (2018).

28. Arumugasamy Elangovan, Yu-Hsiang Wang & Ho., T.-I. Sonogashira Coupling Reaction with Diminished Homocoupling. *Org. Lett.* **5**, 1841–1844 (2003).

29. Kulkarni, R., Huang, J., Trunk, M., Burmeister, D., Amsalem, P., Müller, J. & Bojdys, M. J. Direct Growth of Crystalline Triazine-Based Graphdiyne using Surface-Assisted Deprotection-Polymerisation. *Chem. Sci.* **12**, 12661–12666 (2021).

30. Huang, C., Li, A., Li, L. & Chen, Z. Synthesis of Quinolines from Aniline and Propanol over Modified USY Zeolite: Catalytic Performance and Mechanism Evaluated by In Situ Fourier Transform Infrared Spectroscopy. *RSC Adv.* **7**, 24950–24962 (2017).

31. Sato, Y., Itoh, K., Hagiwara, R., Fukunaga, T. & Ito, Y. On the So-Called "Semi-ionic" C–F Bond Character in Fluorine–GIC. *Carbon* **42**, 3243–3249 (2004).

32. Borovik, A. S., Bott, S. G. & Barron, A. R. Arene-Mercury Complexes Stabilized Aluminum and Gallium Chloride: Synthesis and Structural Characterization. *J. Am. Chem. Soc.* **123**, 11219–11228 (2001).

33. Wang, L., Wan, Y., Ding, Y., Wu, S., Zhang, Y., Zhang, X. & Xu, H. Conjugated Microporous Polymer Nanosheets for Overall Water Splitting Using Visible Light.

Adv. Mater. **29,** 1702428 (2017).

34. Wang, F., Zuo, Z., Li, L., Li, K., He, F., Jiang, Z. & Li, Y. Large-Area Aminated-Graphdiyne Thin Films for Direct Methanol Fuel Cells. *Angew. Chem. Int. Ed.* **58**, 15010–15015 (2019).

35. Yang, Z., Liu, R., Wang, N., He, J., Wang, K., Li, X. & Huang, C. Triazine-Graphdiyne: A New Nitrogen-Carbonous Material and Its Application as an Advanced Rechargeable Battery Anode. *Carbon* **137**, 442–450 (2018).

36. Xing, C., Xue, Y., Huang, B., Yu, H., Hui, L., Fang, Y. & Li, Y. Fluorographdiyne: A Metal-Free Catalyst for Applications in Water Reduction and Oxidation. *Angew. Chem. Int. Ed.* **58**, 13897–13903 (2019).

37. Kofuji, Y., Ohkita, S., Shiraishi, Y., Sakamoto, H., Tanaka, S., Ichikawa, S. & Hirai, T. Graphitic Carbon Nitride Doped with Biphenyl Diimide: Efficient Photocatalyst for Hydrogen Peroxide Production from Water and Molecular Oxygen by Sunlight. *ACS Catal.* **6**, 7021–7029 (2016).

38. Shiraishi, Y., Takii, T., Hagi, T., Mori, S., Kofuji, Y., Kitagawa, Y. & Hirai, T. Resorcinol-Formaldehyde Resins as Metal-Free Semiconductor Photocatalysts for Solar-to-Hydrogen Peroxide Energy Conversion. *Nat. Mater.* **18**, 985–993 (2019).

39. Zatryb G. & Klak M M. On the Choice of Proper Average Lifetime Formula for an Ensemble of Emitters Showing Non-Single Exponential Photoluminescence Decay. *J. Phys. Condens. Matter.* **32**, 415902 (2020).

40. Bai, J., Sun, Y., Li, M., Yang, L., Li, J. & Hu, S. “Two Channel” Photocatalytic

Hydrogen Peroxide Production Using gC_3N_4 Coated CuO Nanorod Heterojunction Catalysts Prepared via a Novel Molten Salt-Assisted Microwave Process. *New J. Chem*. **42**, 13529-13535 (2018).

41. Zhang, Y. & Park, S. J. Formation of Hollow MoO_3/SnS_2 Heterostructure Nanotubes for Efficient Light-Driven Hydrogen Peroxide Production. *J. Mater. Chem. A* **6**, 20304-20312 (2018).

42. Wang, H., Guan, Y., Hu, S., Pei, Y., Ma, W. & Fan, Z. Hydrothermal Synthesis of Band Gap-Tunable Oxygen-Doped g-C_3N_4 with Outstanding "Two-Channel" Photocatalytic H_2O_2 Production Ability Assisted by Dissolution–Precipitation Process. *Nano* **14**, 1950023 (2019).

43. Zhu, C., Zhu, M., Sun, Y., Zhou, Y., Gao, J., Huang, H., Liu, Y. & Kang, Z. Carbon-Supported Oxygen Vacancy-Rich Co_3O_4 for Robust Photocatalytic H_2O_2 Production via Coupled Water Oxidation and Oxygen Reduction Reaction. *ACS Appl. Energy Mater.* **2**, 8737-8746 (2019).

44. Liu, Y., Zeng, X., Easton, C. D., Li, Q., Xia, Y., Yin, Y., Hu, X., Hu, J., Xia, D., McCarthy, D. T., Deletic, A., Sun, C., Yu, J. & Zhang, X. An In Situ Assembled WO_3–TiO_2 Vertical Heterojunction for Enhanced Z-Scheme Photocatalytic Activity. *Nanoscale*, **12**, 8775-8784 (2020).

45. Chen, L., Wang, L., Wan, Y., Zhang, Y., Qi, Z., Wu, X. & Xu, H. Acetylene and Diacetylene Functionalized Covalent Triazine Frameworks as Metal-Free Photocatalysts for Hydrogen Peroxide Production: a New Two‐Electron Water

Oxidation Pathway. *Adv. Mater.* **32**, 1904433 (2020).

46. Zhao, X., You, Y., Huang, S., Wu, Y., Ma, Y., Zhang, G. & Zhang, Z. Z-Scheme Photocatalytic Production of Hydrogen Peroxide over $Bi_4O_5Br_2$/g-C_3N_4 Heterostructure under Visible Light. *Appl. Catal. B.* **278**, 119251 (2020).

47. Zhao, Y., Liu, Y., Cao, J., Wang, H., Shao, M., Huang, H., Liu, Y. & Kang, Z. Efficient Production of H_2O_2 via Two-Channel Pathway over ZIF-8/C_3N_4 Composite Photocatalyst Without any Sacrificial Agent. *Applied Catalysis B: Environmental*. **278**, 119289 (2020).

48. Ye, Y. X., Pan, J., Xie, F., Gong, L., Huang, S., Ke, Z. & Ouyang, G. Highly Efficient Photosynthesis of Hydrogen Peroxide in Ambient Conditions. *Proc. Natl. Acad. Sci.* **118**, e2103964118 (2021).

49. Yang, C., Wan, S., Zhu, B., Yu, J. & Cao, S. Calcination - Regulated Microstructures of Donor-Acceptor Polymers Towards Enhanced and Stable Photocatalytic H_2O_2 Production in Pure Water. *Angew. Chem. Int. Ed.* **61**, e202208438 (2022).

50. Kou, M., Wang, Y., Xu, Y., Ye, L., Huang, Y., Jia, B., Li, H., Ren, J., Deng, Y., Chen, J., Zhou, Y., Lei, K., Wang, L., Liu, W., Huang, H. & Ma, T. Molecularly Engineered Covalent Organic Frameworks for Hydrogen Peroxide Photosynthesis. *Angew. Chem. Int. Ed.* **61**, e202200413 (2022).

51. Cheng, H., Lv, H., Cheng, J., Wang, L., Wu, X. & Xu, H. Rational Design of Covalent Heptazine Frameworks with Spatially Separated Redox Centers for

High-Efficiency Photocatalytic Hydrogen Peroxide Production. *Adv. Mater.* **34**, 2107480 (2022).

52. Wang, X., Han, Z., Yu, L., Liu, C., Liu, Y. & Wu, G. Synthesis of Full-Spectrum-Response $Cu_2(OH)PO_4$/g-C_3N_4 Photocatalyst with Outstanding Photocatalytic H_2O_2 Production Performance via a "Two Channel Route". *ACS Sustainable Chem. Eng.* **6**, 14542–14553 (2018).

53. Chen, L., Wang, L., Wan, Y., Zhang, Y., Qi, Z., Wu, X. & Xu, H. Acetylene and Diacetylene Functionalized Covalent Triazine Frameworks as Metal-Free Photocatalysts for Hydrogen Peroxide Production: A New Two-Electron Water Oxidation Pathway. *Adv. Mater.* **32**, e1904433 (2020).

54. Wang, H., Yang, C., Chen, F., Zheng, G. & Han, Q. A Crystalline Partially Fluorinated Triazine Covalent Organic Framework for Efficient Photosynthesis of Hydrogen Peroxide. *Angew. Chem. Int. Ed.* **61**, e202202328 (2022).

55. Wang, L., Wan, Y., Cheng, H., Qi, Z., Zheng, X., Wu, X. & Xu, H. Unraveling the Photocatalytic Water Dissociation Pathways on Two-Dimensional Conjugated Polymers. *ChemCatChem* **11**, 6236–6243 (2019).

56. Cheng, H., Lv, H., Cheng, J., Wang, L., Wu, X. & Xu, H. Rational Design of Covalent Heptazine Frameworks with Spatially Separated Redox Centers for High-Efficiency Photocatalytic Hydrogen Peroxide Production. *Adv. Mater.* **34**, 2107480 (2022).

57. Tachibana, Y., Vayssieres, L. & Durrant, J. R. Artificial Photosynthesis for Solar

Water-Splitting. *Nat. Photonics* **6**, 511–518 (2012).

58. He, T., Wu, J., Li, Y., Wei, K., Liu, Y., Huang, H. & Kang, Z. A Step-by-Step Design for Dual Channel Metal-Free Photocatalysts Towards High Yield H_2O_2 Photo-Production from Air and Water. *Chem. Eng. J.* **451,** 138551 (2023).
59. Miao, T. & Tang, J. Characterization of Charge Carrier Behavior in Photocatalysis using Transient Absorption Spectroscopy. *J. Chem. Phys.* **152**, 194201 (2020).
60. Zhang, J., Zhu, B., Zhang, L. & Yu, J. Femtosecond Transient Absorption Spectroscopy Investigation into the Electron Transfer Mechanism in Photocatalysis. *Chem. Commun.* **59**, 688–699 (2023).
61. Guidetti, G., Pogna, E. A., Lombardi, L., Tomarchio, F., Polishchuk, I., Joosten, R. R. & Montalti, M. Photocatalytic Activity of Exfoliated Graphite-TiO_2 Nanoparticle Composites. *Nanoscale* **11**, 19301–19314 (2019).
62. Kaniyankandy, S., Achary, S. N., Rawalekar, S. & Ghosh, H. N. Ultrafast Relaxation Dynamics in Graphene Oxide: Evidence of Electron Trapping. *J.Phys. Chem. C* **115**, 19110–19116 (2011).
63. Yuan, H., Shi, W., Lu, J., Wang, J., Shi, Y., Guo, F. & Kang, Z. Dual-Channels Separated Mechanism of Photo-Generated Charges over Semiconductor Photocatalyst for Hydrogen Evolution: Interfacial Charge Transfer and Transport Dynamics Insight. *Chem. Eng. J.* **454,** 140442 (2023).
64. He, X., Zhao, L., Zhou, Z., Zhang, S., Pan, H., Chen, J. & Xu, J. Near Unity Charge Separation Efficiency Leads to Pure Ultraviolet Emission in Few Layer Graphene

Nanosheets. *Nanotechnol.* **30**, 295201 (2019).

65. Guo, F., Chen, Z., Shi, Y., Cao, L., Cheng, X., Shi, W. & Lin, X.A Ragged Porous Hollow Tubular Carbon Nitride Towards Boosting Visible-Light Photocatalytic Hydrogen Production in Water and Seawater. *Renewable Energy* **188**, 1–10 (2022).

66. Guo, F., Shi, W., Li, M., Shi, Y. & Wen, H. 2D/2D Z-Scheme Heterojunction of $CuInS_2$/g-C_3N_4 for Enhanced Visible-Light-Driven Photocatalytic Activity Towards the Degradation of Tetracycline. *Sep. Purif. Technol.* **210**, 608–615 (2019).

67. Wang, H., Liang, Y., Liu, L., Hu, J. & Cui, W. Highly Ordered TiO_2 Nanotube Arrays Wrapped with g-C_3N_4 Nanoparticles for Efficient Charge Separation and Increased Photoelectrocatalytic Degradation of Phenol. *J. Hazard. Mater.* **344**, 369–380 (2018).

Chapter 3

Synthesis and Properties of Platinum Graphynes and Application Studies in the Resistive Random Access Memory

3.1 Introduction

Resistive random access memory (RRAM) is a non-volatile memory (NVM) device that records and stores data information based on resistance changes. In recent years, NVM devices have played a pivotal role in the development of memory due to their high density, high scalability, low power consumption, and compatibility with complementary metal-oxide-semiconductor (CMOS) technology[1-5]. Silicon-based flash memory as a traditional NVM device, has been widely used in removable memory applications[6-8]. However, bottlenecks such as insufficient working life, read and write speed, high voltage in write operations, and the inability to continue to shrink the size have restricted the further development of flash memory in many ways[9,10]. As an alternative, a variety of emerging devices have received widespread attention in the industry as next-generation NVM devices[11,12], including RRAM, ferroelectric random access memory (FeRAM)[13], magnetic random access memory (MRAM)[14], and phase change random access memory (PRAM)[15], etc. However, both FeRAM and MRAM have difficulties in further reducing their size. Under such circumstances, RRAM devices have caused a widespread research and development boom in recent years because of their considerable miniaturization prospects.

For the future development of artificial-general-intelligence, artificial vision

system which is characterized by in-sensor multi-task learning has attracted much attention and the related opto-resistive random access memory (ORRAM) and opto-synaptic devices closely have emerged as promising candidates because they not only directly respond to optical stimulation but also allow temporary memory and real-time processing of visual information[16-18]. Compared to von Neumann architectures featuring separation of storage and computation, artificial opto-synaptic systems inspired by biological visions usually integrate photoreceptors, storage units, and processing units together, achieving efficient neuromorphic computing[19,20]. However, the current artificial visions still have certain shortcomings. For example, compared with the human visual system, it generates a large amount of redundant data, and the processing and storage units cannot directly respond to the optical stimulation, resulting in high energy consumption and low efficiency[21-23]. Therefore, there is an urgent demand to develop multifunctional opto-electronic devices integrating sensing, storage, and processing functions to achieve more efficient artificial vision systems. Significant efforts have been made to emulate the synaptic function of the human retina for efficient in-sensor multi-task learning. At present, traditional RRAM devices are mainly based on oxides, including oxide insulators (TiO_x, and TaO_x)[24], composite oxides ($SrTiO_3$)[25], and high-energy dielectrics (AlO_x and HfO_x)[26]. Therefore, new functional materials for RRAM devices should be explored to overcome the limitations of low reproducibility, high formation voltage, and poor scalability of oxide memristors. 2D materials, as new functional materials with distinctive band structures and intriguing electrical properties,

have been explored for the application of RRAM devices, such as organic materials of MOFs[27] and COFs[28] and inorganic materials of graphene[29], MoS_2[30], WS_2[31], h-BN[32], and black phosphorus[33].

Metallated graphynes (MGYs), afforded by the introduction of single metal atoms into the frameworks of graphdiynes, have been considered as a new class of functional materials with metal-acetylenic bonds in the skeleton and explored as efficient photo- and electro-2D devices recently due to their highly ordered pores, high π-conjugation, tunable structure, and large surface area[34].What's more, a series of MGYs (M = Au, Ag, Hg, Cu, and Co)[34-38] have been successfully explored, while platinum-based graphyne (Pt-GYs) has not been reported yet. In another aspect, since the first synthesis of platinum(II)-acetylene compounds by Hagihara[39], polymetallic compounds of group 10 have been extensively studied in applications such as electronics, photonics, and optical sensing. Wong[40-43] et al., conducted extensive research in the field of transition metal polyyne polymers, especially in the field of platinum(II)-acetylide complexes and polymers. Moreover, Dong[44] et al. reported three new porphyrinated platinum(II)-based polymers and utilized them as the active layer for memory devices. What's more, the linear geometry and unsaturated nature of platinum-alkyne units make them very promising structural building blocks, and their alkynyl units can be bonded to various carbocyclic and heteroaromatic ring systems to form 2D platinum-alkyne materials[45]. However, 2D platinum-polyyne networks, which can be regarded as platinum graphynes (Pt-GYs), have never been reported. In addition, to the best of our knowledge,

the application of MGYs in RRAM devices has not yet been studied. Besides, the working principle of RRAM devices based on two-dimensional materials is still controversial. Systematic study of the behavior of current changes with voltage in the same series of 2D materials is conducive to a deep understanding of the resistive switching (RS) mechanism of RRAM.

In this work, we proposed to use suitable organic ligands (**TEPB**, **TEPT**, **and TEFB**) to coordinate with Pt(II)-complex to prepare a series of Pt-GYs (**TEPB-Pt-GY**, **TEPT-Pt-GY**, and **F-Pt-GY**) and study their structures and basic photoelectric properties comprehensively. Furthermore, we utilized them as the active layer in RRAM devices with a two-terminal structure of **Pt/PMMA+Pt-GYs/ITO** (PMMA, poly(methyl methacrylate); ITO, indium tin oxide) and investigated their RS characteristics. It was found that the devices with structure of **Pt/PMMA+TEPB-Pt-GY/ITO** exhibit a typical and stable NVM within the applied voltage. Furthermore, **Pt/PMMA+TEPB-Pt-GY/ITO** RRAM also displayed a light-tunable synaptic behavior, which can be applied as ORRAM, showing a great application potential in the field of in-sensor computing and artificial intelligence (AI) network. Experimental results revealed that the introduction of heteroatoms into the framework of Pt-GYs causes different memory behaviors among devices. It is supposed that valence change may be the memory mechanism based on the experiments and DFT calculations. This work may provide a new sight for scientists to design more efficient ORRAM devices based on 2D organic materials.

3.2 Synthesis and characterization of platinum graphynes

3.2.1 Synthesis of the organic ligands

The synthetic routes of the designed organic ligands (**TEPB**, **TEPT**, and **TEFB**) were described in Chapter 2, which are no longer displayed here. While the platinum precursor of ***trans*-Pt(PBu$_3$)$_2$Cl$_2$** was prepared from the reaction of K_2PtCl_4 and tributylphosphine (PBu_3) and the synthetic routes are shown in Figure 3.1. The chemical structure of ***trans*-Pt(PBu$_3$)$_2$Cl$_2$** was characterized by ^{1}H NMR and ^{31}P NMR (the details are shown in Chapter 5)

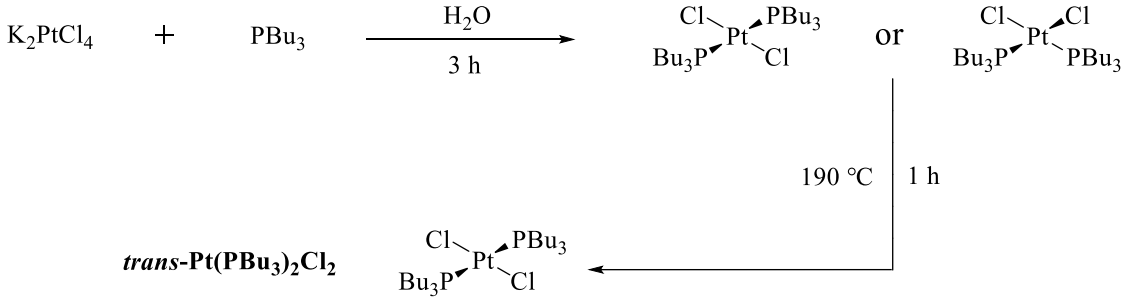

Figure 3.1 Synthetic routes of ***trans*-Pt(PBu$_3$)$_2$Cl$_2$**.

3.2.2 Synthesis of the platinum graphynes

As displayed in Figure 3.2, **TEPB-Pt-GY**, **TEPT-Pt-GY**, and **F-Pt-GY** were synthesized via the base-catalyzed dehydrohalogenation reactions between the ligands of **TEPB**, **TEPT**, and **TEFB** and ***trans*-Pt(PBu$_3$)$_2$Cl$_2$**, respectively according to the previous literature[43] (the details are shown in Chapter 5). What's more, it was found that **TEPT-Pt-GY** can be obtained with a high yield at room temperature (RT) while the yields of **TEPB-Pt-GY** and **F-Pt-GY** are lower at RT, which indicated that **TEPT** is easier to coordinate with *trans*-Pt(PBu$_3$)$_2$Cl$_2$ than **TEPB** and **TEFB**.

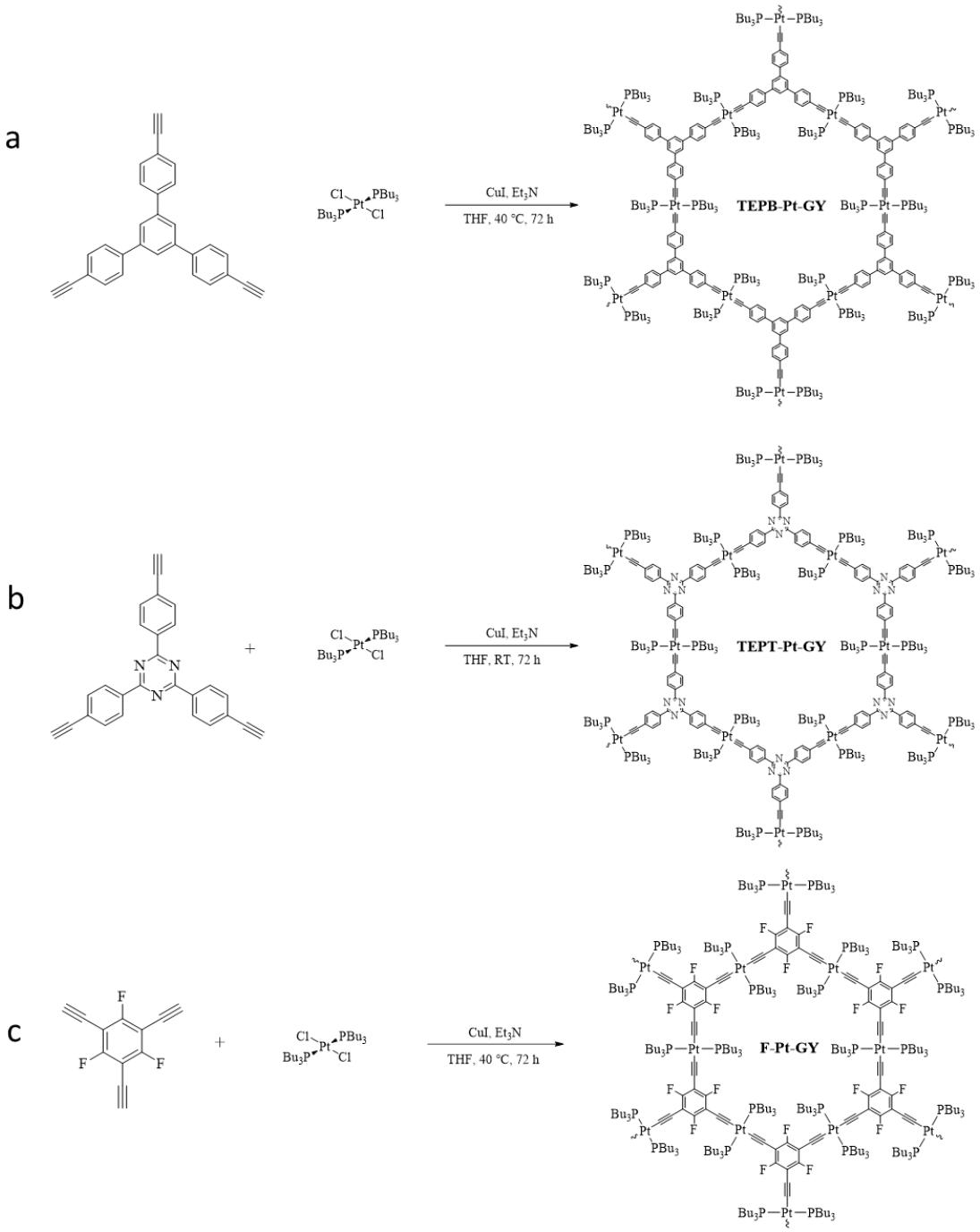

Figure 3.2 Synthetic routes of the platinum graphynes of (a) **TEPB-Pt-GY**, (b) **TEPT-Pt-GY**, and (c) **F-Pt-GY**.

3.2.3 Characterization of the platinum graphynes

Comprehensive characterizations were conducted to identify the chemical structure of **TEPB-Pt-GY**, **TEPT-Pt-GY**, and **F-Pt-GY**, such as FTIR, solid-state ^{13}C NMR, XPS, and XRD pattern. What's more, their morphologies were displayed by

TEM. As shown in Figure 3.3, FTIR spectra of **TEPB-Pt-GY**, **TEPT-Pt-GY**, and **F-Pt-GY** showed that the sharp peaks at about 3200 cm^{-1} for the ≡C–H stretching vibrations disappeared compared to their corresponding organic ligand of **TEPB**, **TEPT**, and **TEFB**, indicating that the base-catalyzed dehydrohalogenation reactions were completed. In addition, the characteristic absorption peaks at about 2950 cm^{-1}, 2920 cm^{-1} and 2860 cm^{-1} in all spectra correspond to the saturated C–H stretching vibrations of butyl group[46] and indicated that ***trans*-$Pt(PBu_3)_2Cl_2$** coordinated successfully with the as-designed organic ligands. For **TEPT-Pt-GY**, the peaks at 1516 cm^{-1}, 1359 cm^{-1}, and 820 cm^{-1} in Figure 3.3b can be assigned to the triazine ring[47]. For **F-Pt-GY**, the peak at 1110 cm^{-1} can be assigned to the semi-ionic C–F bond[48]**.** The above assignments revealed that **TEPB-Pt-GY**, **TEPT-Pt-GY**, and **F-Pt-GY** were successfully synthesized.

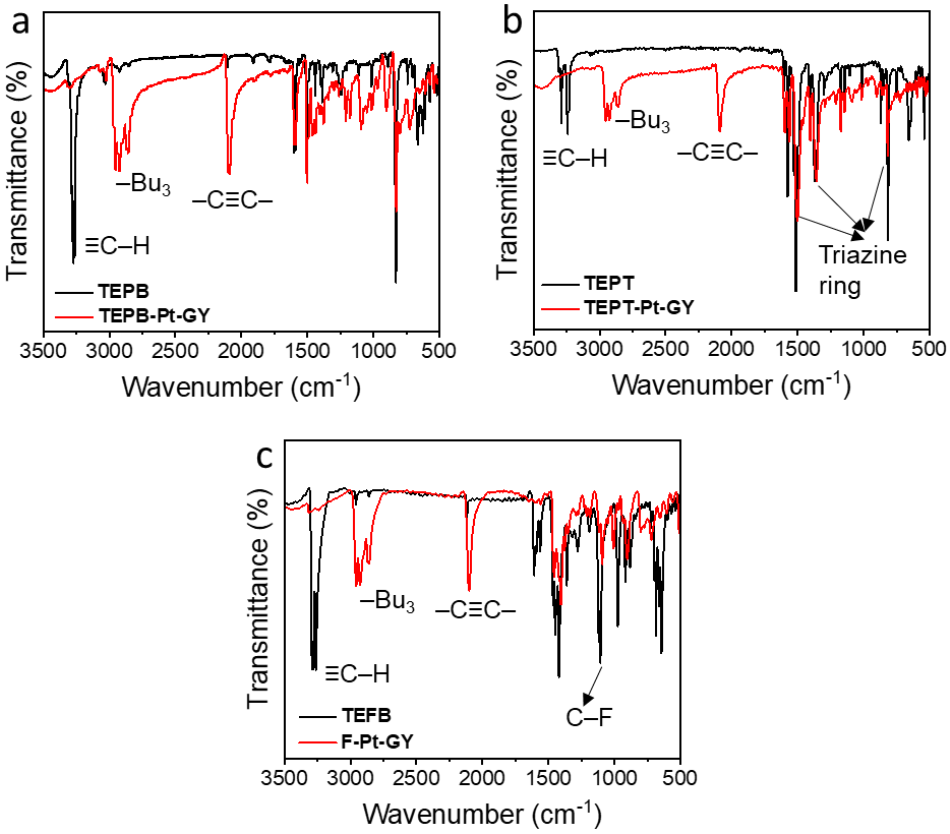

Figure 3.3 FTIR spectra of the platinum graphynes of (a) **TEPB-Pt-GY**, (b) **TEPT-Pt-GY**, and (c) **F-Pt-GY**.

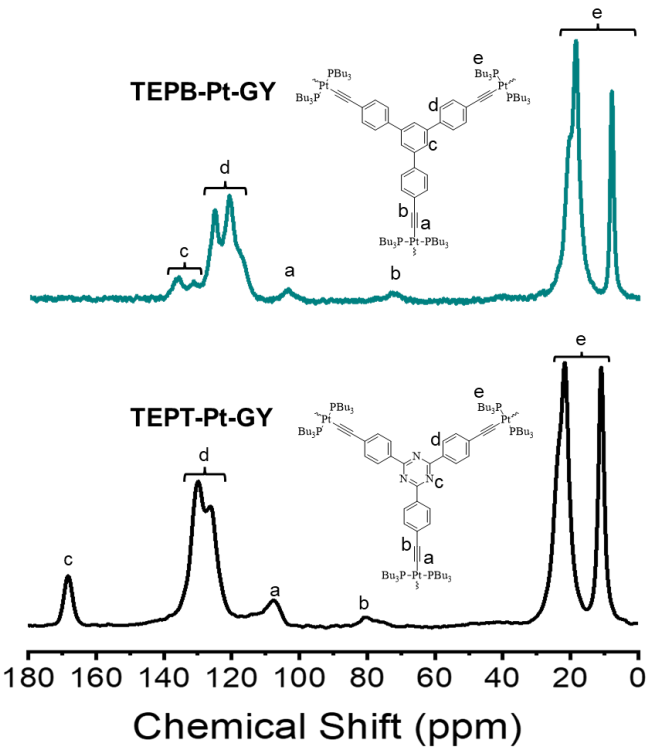

Figure 3.4 Solid-state ^{13}C NMR spectra of **TEPB-Pt-GY** and **TEPT-Pt-GY**.

To further confirmed the chemical structures of platinum graphynes, the solid-state ^{13}C CPMAS NMR were also performed, as shown in Figure 3.4. The peaks at ≈8 and ≈19 ppm in both solid-state ^{13}C NMR spectra showed the presence of the butyl groups[49,50] in the frameworks of Pt-GYs and the peaks at ≈80 and ≈110 ppm can be assigned to the carbon atoms in the –C≡C–Pt–C≡C– moiety[51]. In addition, the peaks in the range of 120–140 ppm in the top spectra can be attributed to the phenyl groups in **TEPB-Pt-GY**[52]. What' more, the peak at ≈170 ppm in the bottom spectra can be assigned to the triazine groups in **TEPT-Pt-GY**[47]. XPS spectra shown in Figure 3.5 were further conducted to illustrate the chemical states of the existing elements in **TEPB-Pt-GY**, **TEPT-Pt-GY**, and **F-Pt-GY**, respectively. For the full-XPS spectrum of **TEPB-Pt-GY**, the binding energy of 285.88, 190.37, 132.24, 333.79, 316.01, 103.85, 77.41 and 74.13 eV can be ascribed to C 1s, P 2s, P 2p, Pt 4d, Pt 5s, Pt $4f_{5/2}$ and Pt $4f_{7/2}$, respectively[53] (Figure 3.5a). For the full spectrum of **TEPT-Pt-GY**, the binding energy of N 1s is 399.74 eV and the binding energy of C 1s, P 2s, P 2p, Pt 4d, Pt 5s, Pt $4f_{5/2}$ and Pt $4f_{7/2}$ is 285.58, 190.38, 132.12, 333.33, 315.89, 103.59, 77.78, and 73.81 eV, respectively (Figure 3.5b). For the **F-Pt-GY,** the full XPS spectrum showed that the binding energy of 399.74 eV is assigned to F 1s and the binding energy of C 1s, P 2s, P 2p, Pt 4d, Pt 5s, Pt $4f_{5/2}$ and Pt $4f_{7/2}$ is 285.28, 187.92, 131.33, 332.93, 316.86, 103.39, and 75.81, and 72.66 eV, respectively (Figure 3.5c). The comparison among the three XPS spectra showed that the introduction of heteroatoms hardly affects the chemical states of the existing elements.

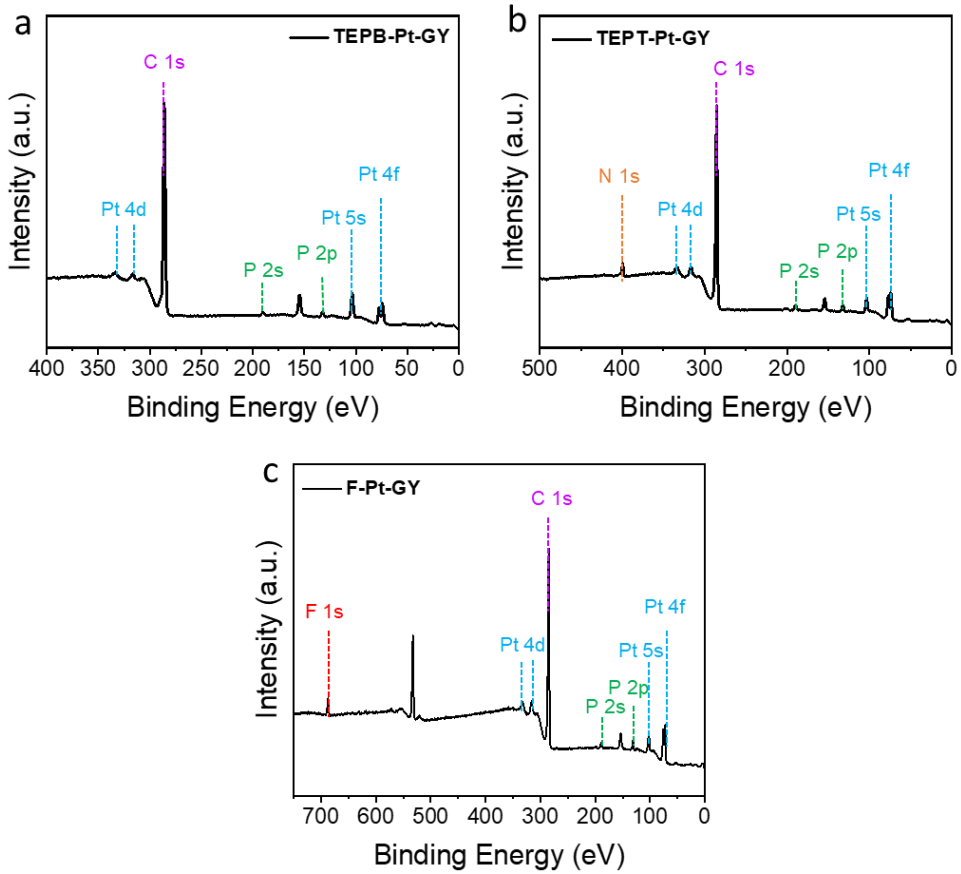

Figure 3.5 The full XPS spectra of (a) **TEPB-Pt-GY**, (b) **TEPT-Pt-GY**, and (c) **F-Pt-GY**.

The crystal structures of **TEPB-Pt-GY**, **TEPT-Pt-GY**, and **F-Pt-GY** were characterized by PXRD, as shown in Figure 3.6. It can be seen that **TEPB-Pt-GY** and **TEPT-Pt-GY** show the same peaks at the 2θ angles of 10°, 16°, and 20°, which indicated that they possessed the same crystal form. **F-Pt-GY** just shows two peaks at the 2θ angles of 10° and 20°, indicating a different form of crystal, which revealed that the organic ligands have an influence on the crystal types of Pt-GYs. In addition, for the same type of crystal, **TEPT-Pt-GY** showed an enhanced intensity than **TEPB-Pt-GY**, revealing that the introduction of triazine ring into the framework can improve the crystallinity of Pt-GYs, which may be because triazine can make the molecular plane flatter, thereby improving crystallinity. Furthermore, Pt-GYs have poor crystallinity

compared to that of Hg-GYs, which may be caused by the presence of butyl groups.

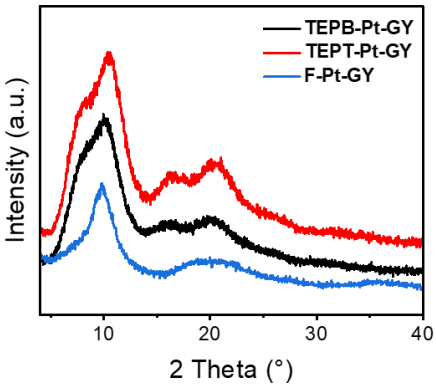

Figure 3.6 PXRD patterns of **TEPB-Pt-GY**, **TEPT-Pt-GY**, and **F-Pt-GY**.

TEM technique was performed to study their morphologies (Figure 3.7). Large-scale TEM images (Figure 3.7a–c) showed that **TEPB-Pt-GY**, **TEPT-Pt-GY**, and **F-Pt-GY** are characterized by nanosheet structures. In addition, HRTEM images (Figure 3.7d–f) revealed that the interlayer distance of the Pt-GYs is ~0.44 nm[54]. It can be concluded that Pt-GYs have a larger interlayer distance than that of Hg-GYs, which may be because of the presence of PBu_3 units in the skeleton.

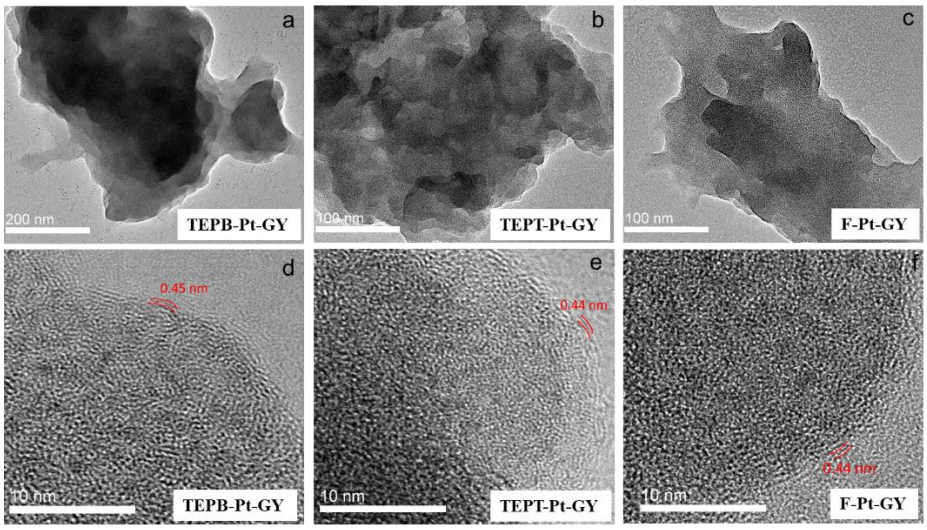

Figure 3.7 Large-scale TEM images of (a) **TEPB-Pt-GY**, (b) **TEPT-Pt-GY**, and (c) **F-Pt-GY** and HRTEM images of (c) **TEPB-Pt-GY**, (d) **TEPT-Pt-GY**, and (e) **F-Pt-GY**.

Finally, the thermal stability of **TEPB-Pt-GY**, **TEPT-Pt-GY**, and **F-Pt-GY** was analyzed by TGA, as shown in Figure 3.8. It can be seen from the TGA curves that **F-Pt-GY** has the best thermal stability with the onset decomposition temperature of about 340 °C, while the onset decomposition temperature of **TEPB-Pt-GY** and **TEPT-Pt-GY** is about 280 °C, which may be due to the semi-metallic nature of the C–F bond in this material. In addition, we can see that the thermal stability of Pt-GYs is not much better than that of Hg-GYs, demonstrating that the introduction of different metals into MGYs has little influence on their thermal stability. On the contrary, the residual mass of Pt-GYs at 800 ℃ after thermogravimetric analysis is about 50%, which is much higher than the residual mass of Pt-GYs with the value of 8%.

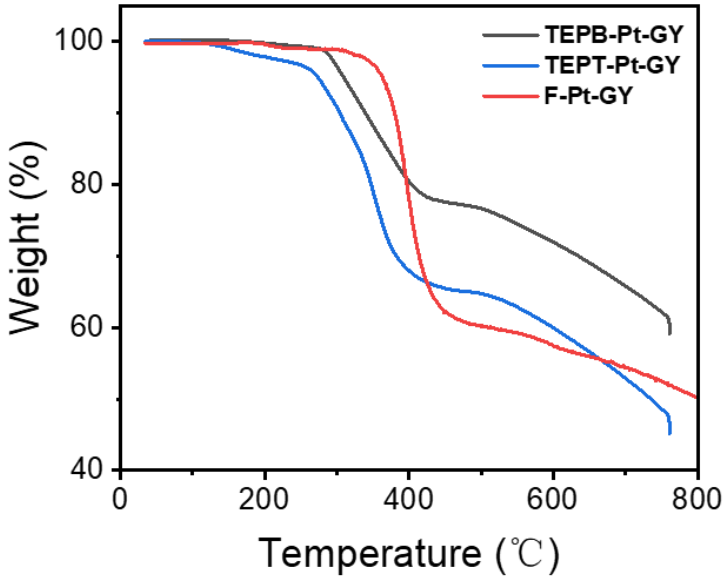

Figure 3.8 TGA curves of **TEPB-Pt-GY**, **TEPT-Pt-GY**, and **F-Pt-GY**.

3.3 Properties of platinum graphynes

There are few physical mechanisms that can cause NVR switching phenomena, including nanomechanical memory effect, molecular resistive switching effect, electrostatic/electronic memory effect, electrochemical metallization memory effect, valence change memory effect, thermochemical memory effect, phase change memory

effect, phrase memory effect, and ferroelectric tunneling effect, etc. Although these situations are all electrically excited resistive switching phenomena, their principles are quite different from each other[55]. For RRAM devices with both top-electrode and bottom-electrode inert, the mechanism of RRAM devices with active layer is generally valence change memory effect caused by charge transfer (CT) within the molecule. For 2D materials, this effect is closely related to the valence band structure and electron distribution. In addition, for ORRAM devices, their performance is also related to the light response of the material. Herein, we explored their properties of band structure, light absorbance, and charge transfer using UV–Vis DRS, UPS, and EIS characterizations as well as their semiconductor type by M–S electrochemical measurements.

Firstly, M–S electrochemical measurements were conducted to study their semiconductor type. Figure 3.9 showed that all the Pt-GYs are n-type semiconductors. What's more, the CB potential of **TEPB-Pt-GY, TEPT-Pt-GY**, and **F-Pt-GY** can be calculated from the M–S data as −0.40, −0.30, and −0.70 V (V vs RHE), respectively.

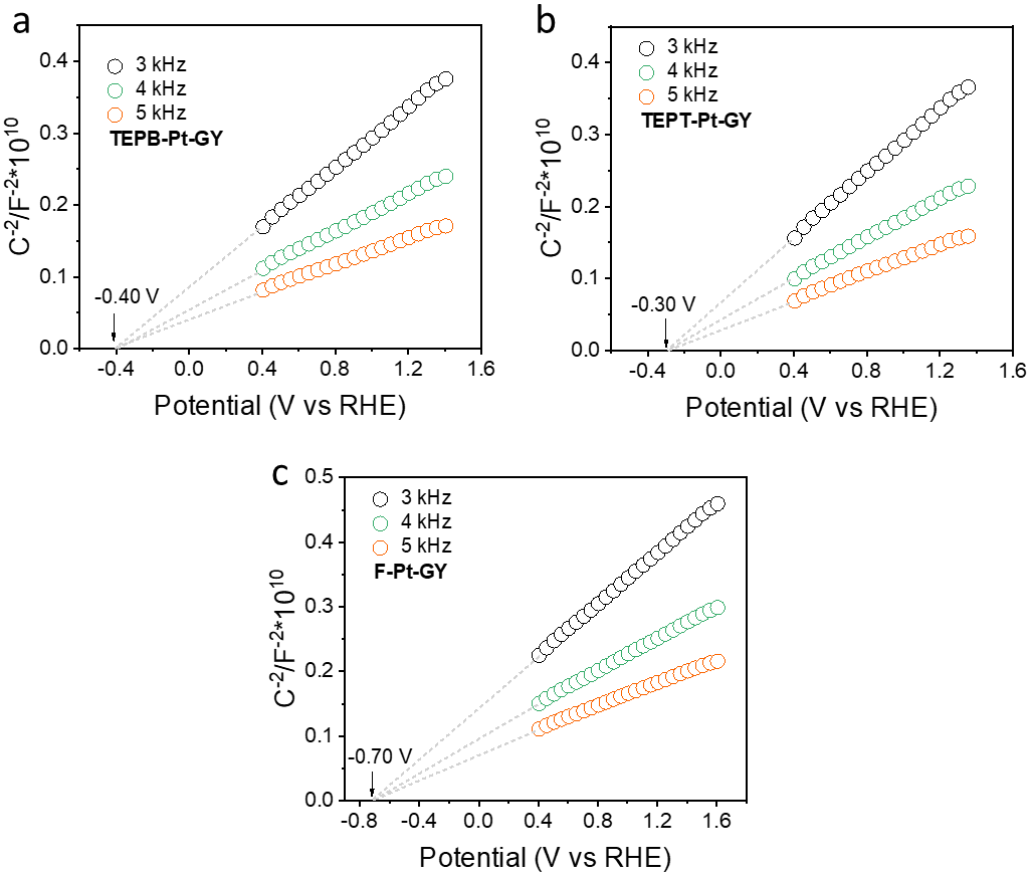

Figure 3.9 M–S curves of (a) **TEPB-Pt-GY**, (b) **TEPT-Pt-GY**, and (c) **F-Pt-GY**.

The light absorption capability of Pt-GYs was demonstrated by UV–Vis DRS, as shown in Figure 3.10. UV–Vis DRS (Figure 3.10a) indicated that **TEPT-Pt-GY** have the enhanced light absorbance than that of **TEPB-Pt-GY**, which indicated that the introduction of triazine is helpful for the light absorption of Pt-GYs. In addition, UV–Vis DRS of **F-Pt-GY** showed that it has a lower light absorbance than that of **TEPB-Pt-GY**, which revealed that the introduction of F atoms also has an influence on the light absorption capability of Pt-GYs. Besides, the corresponding Tauc's plots showed that the optical band gap (E_g) of **TEPB-Pt-GY**, **TEPT-Pt-GY**, and **F-Pt-GY** is 3.04, 2.69, and 3.21 eV, respectively (Figure 3.10b). Furthermore, it can be concluded that Pt-GYs have smaller band gap than those of Hg-GYs (Figure 2.10b), which revealed

that platinum group can decrease the energy potential of MGYs.

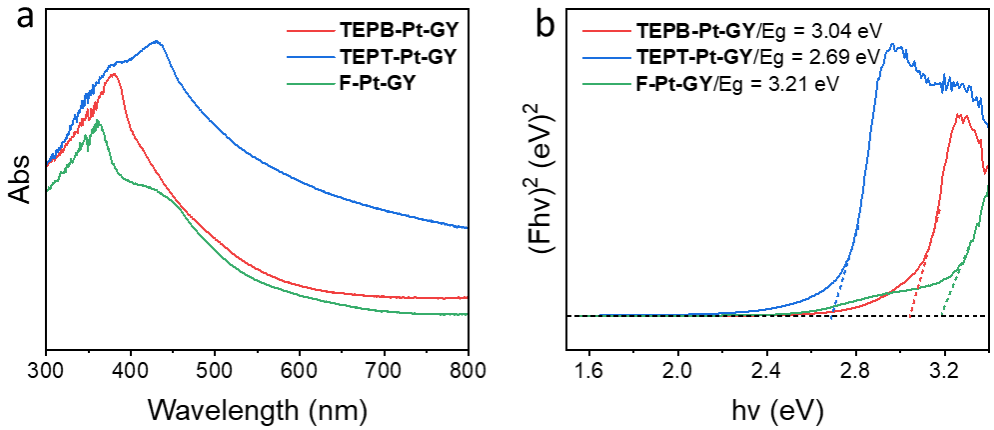

Figure 3.10 (a) UV–Vis spectra and (b) Tauc's plots of **TEPB-Pt-GY**, **TEPT-Pt-GY**, and **F-Pt-GY**.

UPS was performed to verify their VB potentials, as shown in Figure 3.11. Combined with E_g calculated from Tauc's plots, E_{VBM} and E_{CBM} can be calculated by the following equations:

$$\Phi = E_{cutoff} - hv \quad (1)$$

$$E_{VBM} = \Phi - E_{edge} \quad (2)$$

$$E_g = E_{CBM} - E_{VBM} \quad (3)$$

where Φ is the work function, hv = 21.22 eV. Accordingly, the E_{VBM} of **TEPB-Pt-GY**, **TEPT-Pt-GY**, and **F-Pt-GY** were calculated to be 2.43, 2.12, and 2.29 eV (vs. NHE), respectively. As a result, their E_{CBM} potential is −0.60, −0.50, and −0.90 eV (vs. RHE), respectively, which is consistent well with the CB potentials from M–S data. What's more, the corresponding band energy levels are displayed in Fig. 3.12, which indicated clearly that the introduction of heteroatoms can have an influence on the CB and VB potentials of Pt-GYs.

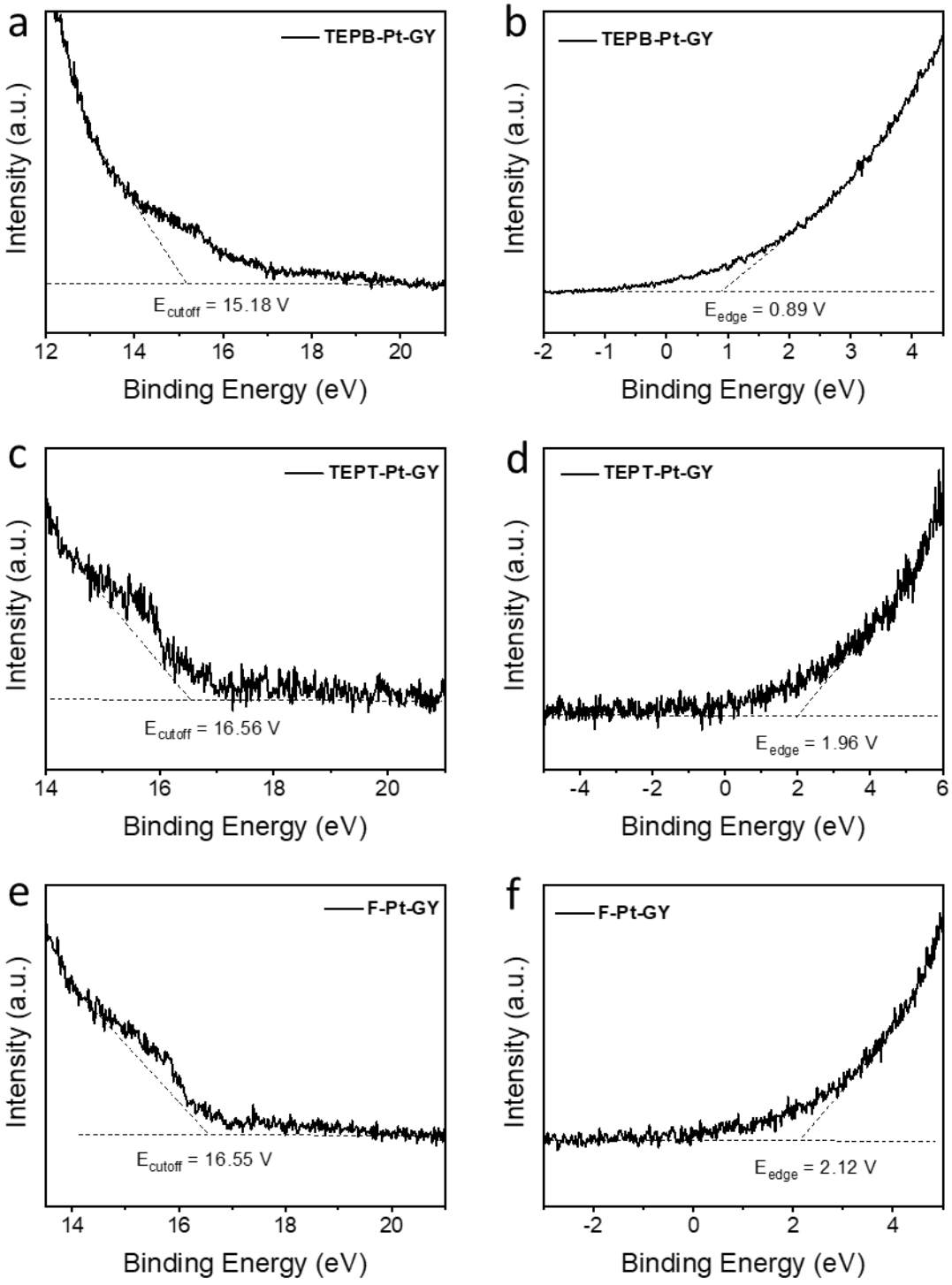

Figure 3.11 UPS of **TEPB-Pt-GY**, **TEPT-Pt-GY**, and **F-Pt-GY**.

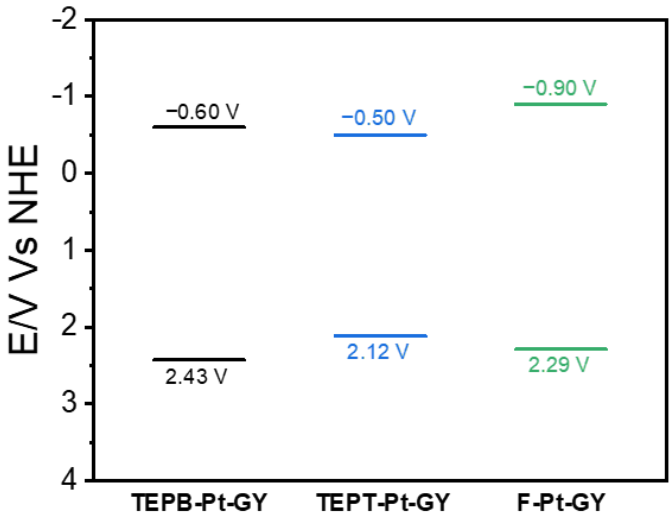

Figure 3.12 VB and CB positions of **TEPB-Pt-GY**, **TEPT-Pt-GY**, and **F-Pt-GY**.

EIS were conducted to explore their electrical properties, Figure 3.13 shows that **TEPT-Pt-GY** and **F-Pt-GY** have a superior electronic conductivity with smaller semicircles in the Nyquist plot than that of **TEPB-Pt-GY**, showing an enhanced charge transfer[56] and the fitting charge transfer rate (R_{ct}) of **TEPB-Pt-GY**, **TEPT-Pt-GY**, and **F-Pt-GY** is 52.72, 46.55, and 30.01, respectively, indicating that the introduction of heteroatoms can improve their photo-electric properties.

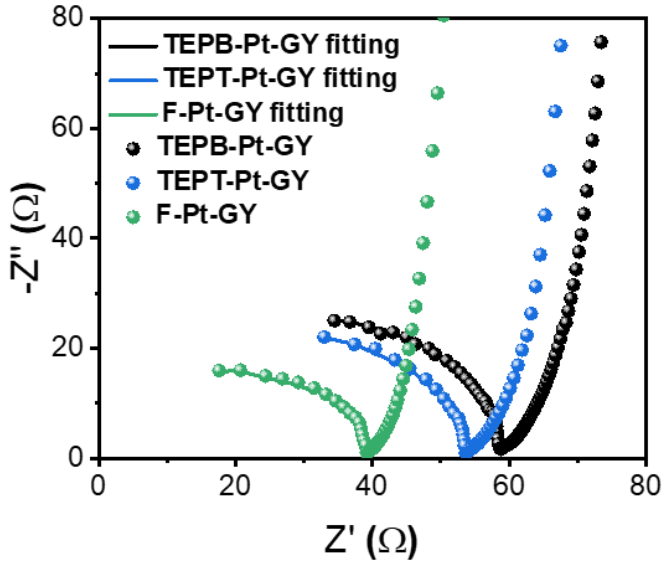

Figure 3.13 EIS curves of **TEPB-Pt-GY**, **TEPT-Pt-GY**, and **F-Pt-GY**.

3.4 Resistive random access memory performance

We fabricated the RRAM devices with a sandwich-like structure consisting of an ITO bottom electrode, a Pt top inert electrode, and Pt-GYs as the active layer, as shown in Figure 3.14a. Figure 3.14b–d showed the typical current-voltage (*I–V*) characteristics curves of these RRAM devices. It can be seen clearly from the *I–V* curves that **Pt/PMMA+TEPB-Pt-GY/ITO** memory device show a stable typical non-volatile memory behavior with the I_{on}/I_{off} of 10^3:1. But **Pt/PMMA+TEPT-Pt-GY/ITO** and **Pt/PMMA+F-Pt-GY/ITO** memory devices do not show the resistive switching behavior. For **Pt/PMMA+TEPB-Pt-GY/ITO** memory device, Figure 3.14b clearly showed the resistive switching characteristics. The device was initially in a low conductivity state (OFF state) during the positive scan from 0 to 2.7 V. Then, the current increases sharply (10^{-6} to 10^{-3} A) at around 2.7 V, indicating that the device transferred from the OFF state to a high conductivity state (ON state) with the I_{on}/I_{off} ratio of about 10^3:1 and remained in the high conductivity state during the subsequent positive scan from 2.7 to 5 V. The device still remained in the ON state during the beginning of the following negative scan from 0 to −2.8 V, then returned to the OFF state at around −2.8 V and remained in the OFF state during the subsequent negative scan from −2.8 to −5 V. The second round (blue line and green line) of *I–V* data demonstrated that this transformation process and its non-volatile properties are stable and repeatable. What's more, the non-volatile characteristic can be induced with the inert electrode, which revealed that **TEPB-Pt-GY** acts as the active layer in the device.

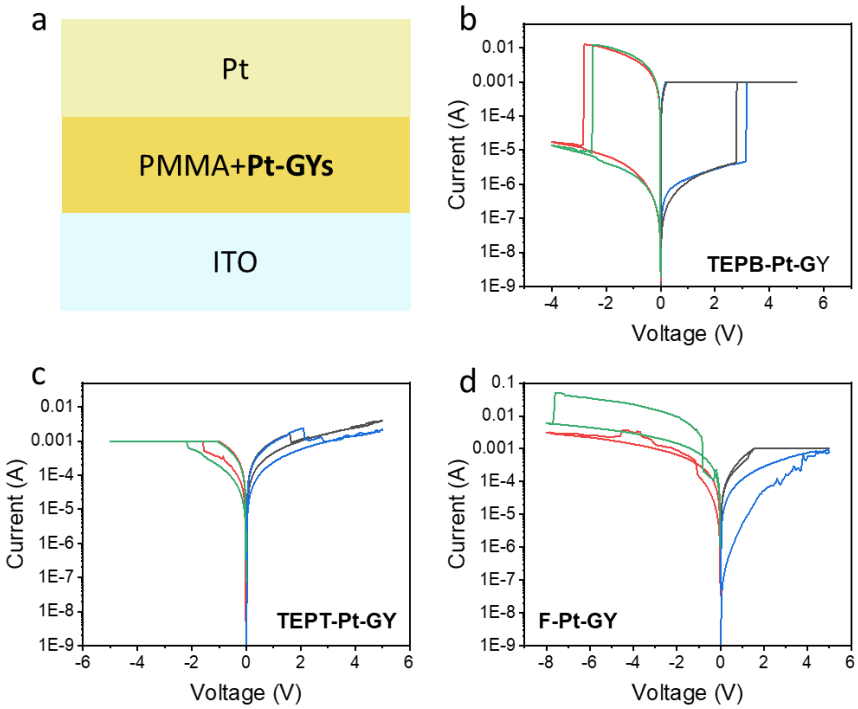

Figure 3.14 (a) Schematic representation of the sandwich-like structure of **Pt/PMMA+Pt-GYs/ITO**. *I–V* curves of the RRAM devices: (b) **Pt/PMMA+TEPB-Pt-GY/ITO**, (c) **Pt/PMMA+TEPT-Pt-GY/ITO**, and (d) **Pt/PMMA+F-Pt-GY/ITO**.

DFT calculations were performed to explore the mechanism of the electrical resistive switching behavior of **Pt/PMMA+TEPB-Pt-GY/ITO** RRAM device. According to previous works related to RRAM devices with inert electrodes and similar materials, the mechanism is generally reported as valence change caused by CT[44,57]. For this work, the valence change can be induced with Pt ion and the introduction of the heteroatoms can alter the electron landscape in the materials. Combined with the phenomenon that the non-volatile behavior can be triggered by a positive scan, it can be speculated that the valence state change process of Pt ion should be Pt(II)-to-Pt(IV) during the positive scan, which is an oxidation process losing electrons. Therefore, the high electron density in and around the Pt atom would be detrimental to this process.

Herein, we built suitable models with **TEPB-Pt-GY**, **TEPT-Pt-GY**, and **F-Pt-GY** in the active layer. Electrostatic potential (ESP) images clearly displayed that the electron density around Pt ion in **TEPB-Pt-GY** is lower than those in **TEPT-Pt-GY** and **F-Pt-GY**, which provided strong evidence that the conversion process of Pt(II)-to-Pt(IV) is more likely to occur with **TEPB-Pt-GY** (Figure 3.15). Combined with EIS analysis that **TEPT-Pt-GY** and **F-Pt-GY** possess larger charge transfer rate than that of **TEPB-Pt-GY** (Figure 3.13)**,** it can be concluded that the valence state change is the dominant mechanism of the electrical resistive switching behavior.

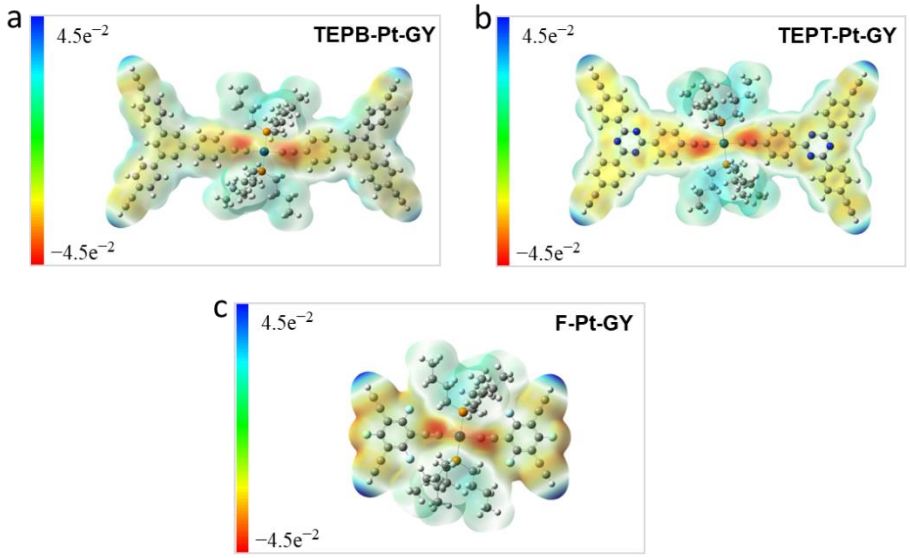

Figure 3.15 ESP images of (a) **TEPB-Pt-GY**, (b) **TEPT-Pt-GY**, and (c) **F-Pt-GY**.

To explore the non-volatile behavior of **TEPB-Pt-GY** based RRAM device, the other two two-terminal structures with different top electrodes (inert electrode: Au and active electrode: Ag) were fabricated based on **TEPB-Pt-GY** materials, as shown in Figure 3.16a, b. The *I–V* curves of the **Ag/PMMA+ Pt-GYs/ITO** RRAM device (Figure 3.16c) also showed electrical resistive switching behavior but were not very

stable. In addition, for the memory device with active electrodes, the mechanism generally involves the formation of conductive filament[58]. On the other hand, **Au/PMMA+Pt-GYs/ITO** RRAM device with an inert electrode showed a non-volatile characteristic during the positive scan, and the behavior was hardly detected during the negative scans and the non-volatile characteristic was very unstable (Figure 3.16d). Such characteristics are different from those of **Pt/PMMA+TEPB-Pt-GY/ITO** memory devices, which may come from different preparation methods for the Pt electrode and Au electrode. Therefore, it can be concluded that the inert Pt electrode is the most suitable for the RRAM device.

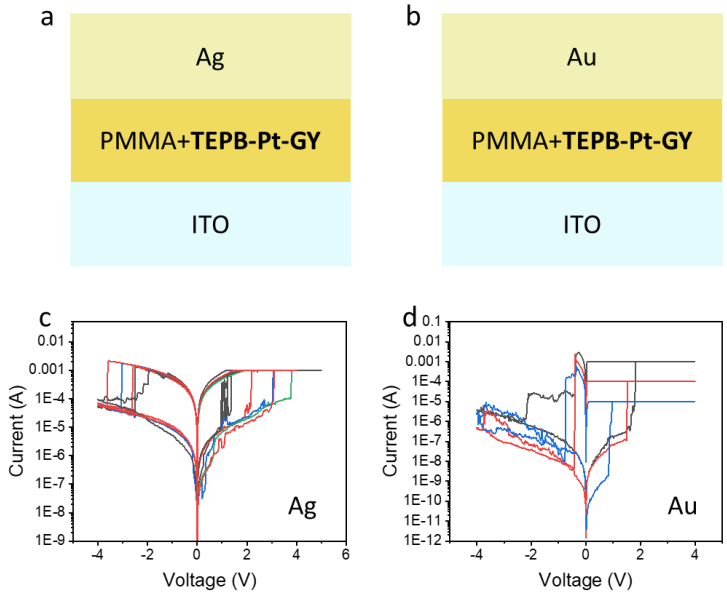

Figure 3.16 (a, b) Schematic representation of the sandwich-like structure of **Ag/PMMA+TEPB-Pt-GY/ITO** and **Au/PMMA+TEPB-Pt-GY/ITO**. *I–V* curves of the RRAM devices: (c) **Ag/PMMA+TEPB-Pt-GY/ITO** and (d) **Au/PMMA+TEPB-Pt-GY/ITO**.

The retention time (*I–V* plot) of the OFF and ON states of the **Pt/PMMA+TEPB-Pt-GY/ITO** memory devices at a read voltage of 0.1V was conducted to evaluate its

reliability, as shown in Figure 3.17a. It is worth noting that the OFF/ON status of the tested devices can remain stable for more than 12000 s without obvious fluctuations, which indicated that the TEPB-Pt-GY-based RRAM devices had good retention properties, making them suitable for data storage. The cyclic switching operation was performed to further study the durability of **Pt/PMMA+TEPB-Pt-GY/ITO** memory devices, as shown in Figure 3.17b. It is evident that both high resistivity state (HRS, OFF state) and low resistivity state (LRS, ON state) remain stable up to 400 pulse numbers, illustrating the excellent reproducibility of such RRAM devices. Therefore, the RRAM devices based on **TEPB-Pt-GY** exhibit excellent stability and have great potential for practical applications.

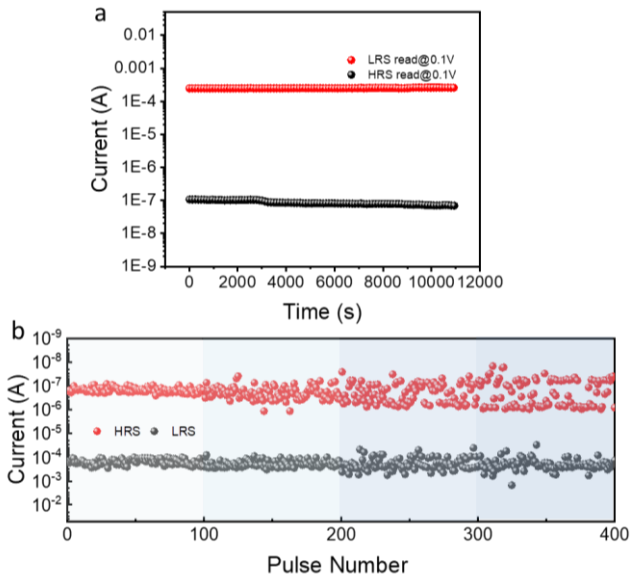

Figure 3.17 (a) Retention time test of **Pt/PMMA+TEPB-Pt-GY/ITO** memory device under read voltage of 0.1 V. (b) Endurance cycle test of **Pt/PMMA+TEPB-Pt-GY/ITO** memory device.

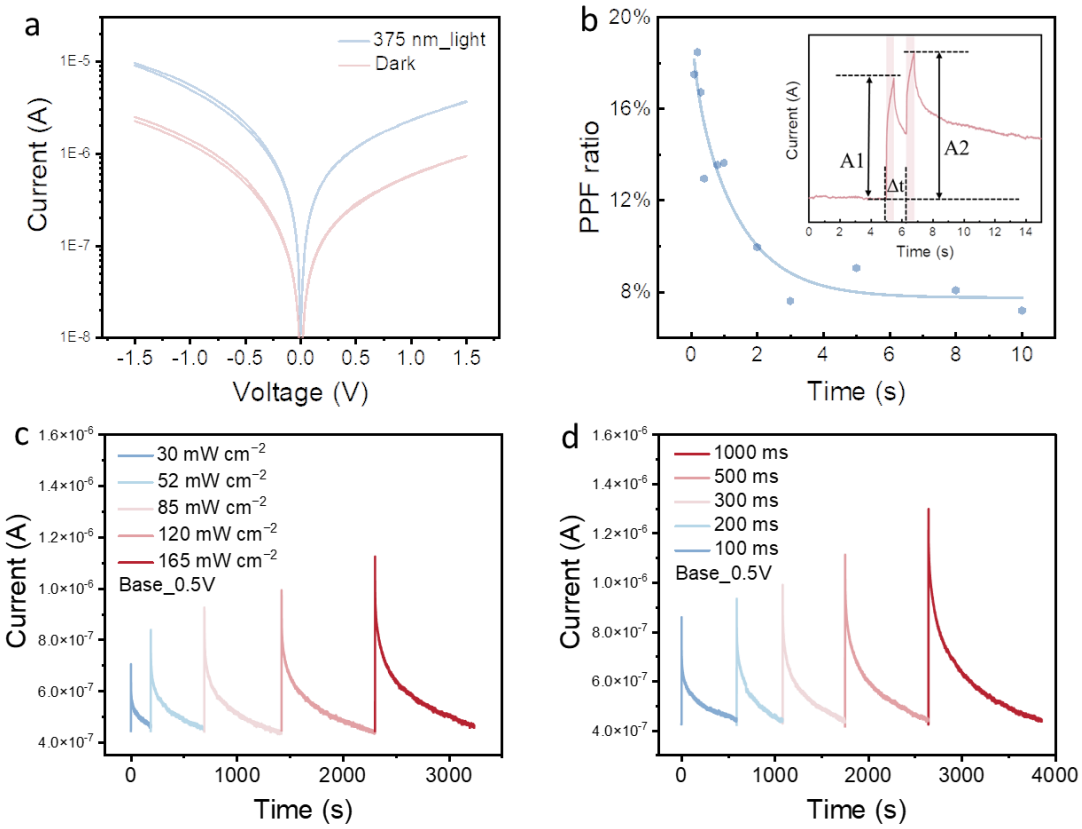

Figure 3.18 (a) *I–V* curves of **Pt/PMMA+TEPB-Pt-GY/ITO** memory without (red) and with (blue) light stimulation. (b) Relationship between PPF index and time interval. (c) Light-intensity-dependent (150, 175, 200, 225, and 250 mW cm^{-2}) current with a pulse width of 100 ms. (d) Light-time-dependent (100, 300, 500, and 1000 ms) current with a pulse intensity of 150 mW cm^{-2}.

Pt/PMMA+TEPB-Pt-GY/ITO ORRAM can respond to light and output a resistance state depending on the light intensity and stimulation time, which indicated that this device can be used to imitate the basic characteristics of synaptic plasticity, achieving learning and memory functions of the human brain. Figure 3.18a schematically showed the output current of the ORRAM synaptic device before and after illumination at the wavelength of 365 nm, showing its photo-responsive characteristics. Subsequently, we simulated paired-pulse facilitation (PPF), in which a

previous pulse can promote subsequent responses at biological synapses. The percentage change of the peak current ((A2 − A1)/A1, defined as the PPF index) showed a negative relationship with the time interval (inert Figure 3.18b). Figure 3.18b showed that the extracted PPF index is approximately 18% at the beginning time, while the PPF index decreases exponentially as the interval increases from 0 s to 10 s. Additionally, the effect of light intensity and illumination time on synaptic behavior was investigated to study their light-sensing capabilities and synaptic function. Figures 3.18c, d showed the spike current and relaxation time as a function of light intensity and pulse width, respectively. The rate of spike current and relaxation time increases with increasing light intensity and pulse width, which fully confirms its synaptic plasticity.

3.5 Conclusion

In summary, a series of Pt-GYs of **TEPB-Pt-GY**, **TEPT-Pt-GY**, and **F-Pt-GY** were successfully synthesized. Then we performed FTIR, solid-state ^{13}C-NMR and XPS spectroscopy, PXRD patterns, and TEM images to analyze their structures and morphologies. In addition, their basic optoelectronic properties were investigated by using UV–Vis DRS, UPS, EIS, and M–S electrochemical measurements, which indicated that all the Pt-GYs materials are n-type semiconductors, and the introduction of heteroatoms have an important influence on their band structures and electron distribution. Finally, these Pt-GYs based RRAM devices were fabricated and we found that **Pt/PMMA+TEPB-Pt-GY/ITO** memory device exhibited a good and stable non-volatile memory behavior with the I_{on}/I_{off} of 10^3:1. It was speculated that the domain

mechanism of the electrical resistive switching behavior should be the valence state change. What' more, both the retention time test and the endurance cycle test demonstrate that the **Pt/PMMA+TEPB-Pt-GY/ITO** RRAM device possesses a great potential for practical applications. Furthermore, it is noted that such memory device can also be switched to the LRS under light illumination by an UV laser with a wavelength of 365 nm, which indicated that such memory device can be regarded as an ORRAM synaptic device that not only store optical information but also perform light-tunable synaptic functions. This work shows that the **Pt/PMMA+TEPB-Pt-GY/ITO** ORRAM device presents a great potential in the application of neuromorphic vision systems, such as the first stage of image processing including image contrast enhancement and noise reduction.

References

1. Khan, M., Mutee Ur Rehman, H. M., Tehreem, R., Saqib, M., Rehman, M. M. & Kim, W. Y. All-Printed Flexible Memristor with Metal–Non-Metal-Doped TiO_2 Nanoparticle Thin Films. *Nanomater.* **12**, 2289 (2022).
2. Sun, T., Tu, J., Zhou, Z., Sun, R., Zhang, X., Li, H. & Wang, Z. Resistive Switching of Self-Assembly Stacked h-BN Polycrystal Film. *Cell Rep. Phys. Sci.* **3** (2022).
3. Ziegler, M., Mussenbrock, T. & Kohlstedt, H. in *Bio-Inspired Information Pathways: From Neuroscience to Neurotronics* 77–190 (2023).
4. Lanza, M., Sebastian, A., Lu, W. D., Le Gallo, M., Chang, M. F., Akinwande, D. & Roldan, J. B. Memristive Technologies for Data Storage, Computation, Encryption, and Radio-Frequency Communication. *Science.* **376**, eabj9979 (2022).
5. Ge, R., Wu, X., Kim, M., Shi, J., Sonde, S., Tao, L. & Akinwande, D. Atomristor: Nonvolatile Resistance Switching in Atomic Sheets of Transition Metal Dichalcogenides. *Nano Lett.* **18**, 434–441 (2018).
6. Luo, Y., Ghose, S., Cai, Y., Haratsch, E. F. & Mutlu, O. in *2018 IEEE International Symposium on High Performance Computer Architecture (HPCA).* 504–517 (IEEE).
7. Xiang, J., Li, X., Ma, Y., Zhao, Q., Ho, C. L. & Wong, W. Y. Efficient Flash Memory Devices Based on Non-Conjugated Ferrocene-Containing Copolymers. *J. Mater. Chem. C* **6**, 11348–11355 (2018).
8. Mondal, S. & Venkataraman, V. Low Temperature Below 200° C Solution Processed Tunable Flash Memory Device Without Tunneling and Blocking Layer. *Nat. Commun.* **10**, 2143 (2019).
9. Hidaka, H. *Embedded Flash Memory for Embedded Systems: Technology, Design for Sub-Systems, and Innovations*. *Springer* (2017).
10. Aritome, S. Scaling Challenge Of Nand Flash Memory Cells. (2015).
11. Meijer, G. Who Wins the Nonvolatile Memory Race? *Science.* **319**, 1625–1626 (2008).

12. Lankhorst, M. H. R., Ketelaars, B. W. & Wolters, R. A. M. Low-Cost and Nanoscale Non-Volatile Memory Concept for Future Silicon Chips. *Nat. Mater.* **4**, 347–352 (2005).
13. Fox, G. R., Chu, F. & Davenport, T. Current and Future Ferroelectric Nonvolatile Memory Technology. *J. Vac. Sci. Technol., B: Microelectron. Nanometer Struct.Process., Meas., Phenom.* **19**, 1967–1971 (2001).
14. Cowburn, R. P. Superparamagnetism and the Future of Magnetic Random Access Memory. *J. Appl. Phys.* **93**, 9310–9315 (2003).
15. Lai, S. in *IEEE International Electron Devices Meeting 2003.* 10.11. 11-10.11. 14 (IEEE).
16. Leydecker, T., Herder, M., Pavlica, E., Bratina, G., Hecht, S., Orgiu, E. & Samorì, P. Flexible Non-Volatile Optical Memory Thin-Film Transistor Device with over 256 Distinct Levels Based on an Organic Bicomponent Blend. *Nat. Nanotechnol.* **11**, 769–775 (2016).
17. Tan, H., Liu, G., Zhu, X., Yang, H., Chen, B., Chen, X. & Li, R. W. An Optoelectronic Resistive Switching Memory with Integrated Demodulating and Arithmetic Functions. *Adv. Mater.* **27**, 2797–2803 (2015).
18. Cheng, Z., Ríos, C., Pernice, W. H. P., Wright, C. D. & Bhaskaran, H. On-Chip Photonic Synapse. *Sci. Adv.* **3**, e1700160 (2017).
19. Kim, Y., Chortos, A., Xu, W., Liu, Y., Oh, J. Y., Son, D. & Lee, T. W. A Bioinspired Flexible Organic Artificial Afferent Nerve. *Science.* **360**, 998–1003 (2018).
20. Song, Y. M., Xie, Y., Malyarchuk, V., Xiao, J., Jung, I., Choi, K. J. & Rogers, J. A. Digital Cameras with Designs Inspired by the Arthropod Eye. *Nature.* **497**, 95–99 (2013).
21. Zhang, L., Pasthukova, N., Yao, Y., Zhong, X., Pavlica, E., Bratina, G. & Samorì, P. Self-Suspended Nanomesh Scaffold for Ultrafast Flexible Photodetectors Based on Organic Semiconducting Crystals. *Adv. Mater.* **30**, 1801181 (2018).
22. Du, C., Cai, F., Zidan, M. A., Ma, W., Lee, S. H. & Lu, W. D. Reservoir Computing

using Dynamic Memristors for Temporal Information Processing. *Nat. Commun.* **8**, 2204 (2017).

23. Yao, P., Wu, H., Gao, B., Eryilmaz, S. B., Huang, X., Zhang, W. & Qian, H. Face Classification using Electronic Synapses. *Nat. Commun.* **8**, 15199 (2017).
24. Yang, J. J., Pickett, M. D., Li, X., Ohlberg, D. A., Stewart, D. R. & Williams, R. S. Memristive Switching Mechanism for Metal/Oxide/Metal Nanodevices. *Nat. Nanotechnol.* **3**, 429–433 (2008).
25. Szot, K., Speier, W., Bihlmayer, G. & Waser, R. Switching the Electrical Resistance of Individual Dislocations in Single-Crystalline $SrTiO_3$. *Nat. Mater.* **5**, 312–320 (2006).
26. Kim, S., Chen, J., Chen, Y. C., Kim, M. H., Kim, H., Kwon, M. W. & Park, B. G. Neuronal Dynamics in HfO_x/AlO_y-Based Homeothermic Synaptic Memristors with Low-Power and Homogeneous Resistive Switching. *Nanoscale* **11**, 237–245 (2019).
27. Ding, G., Wang, Y., Zhang, G., Zhou, K., Zeng, K., Li, Z. & Han, S. T. 2D Metal–Organic Framework Nanosheets with Time-Dependent and Multilevel Memristive Switching. *Adv. Funct. Mater.* **29,** 1806637 (2018).
28. Zhou, K., Jia, Z., Zhou, Y., Ding, G., Ma, X. Q., Niu, W. & Zhou, Y. Covalent Organic Frameworks for Neuromorphic Devices. *J. Phys. Chem. Lett.* **14**, 7173–7192 (2023).
29. Hui, F., Grustan‐Gutierrez, E., Long, S., Liu, Q., Ott, A. K., Ferrari, A. C. & Lanza, M. Graphene and Related Materials for Resistive Random Access Memories. *Adv. Electron. Mater.* **3**, 1600195 (2017).
30. Liu, J., Zeng, Z., Cao, X., Lu, G., Wang, L. H., Fan, Q. L. & Zhang, H. Preparation of MoS_2-Polyvinylpyrrolidone Nanocomposites for Flexible Nonvolatile Rewritable Memory Devices with Reduced Graphene Oxide Electrodes. *Small* **8**, 3517–3522 (2012).
31. Das, U., Bhattacharjee, S., Mahato, B., Prajapat, M., Sarkar, P. & Roy, A.

Uniform, Large-Scale Growth of WS_2 Nanodomains via CVD Technique for Stable Non-Volatile RRAM Application. *Mater. Sci. Semicond. Process.* **107**, 104837 (2020).

32. Qian, K., Tay, R. Y., Nguyen, V. C., Wang, J., Cai, G., Chen, T. & Lee, P. S. Hexagonal Boron Nitride Thin Film for Flexible Resistive Memory Applications. *Adv. Funct. Mater.* **26**, 2176–2184 (2016).
33. Han, S. T., Hu, L., Wang, X., Zhou, Y., Zeng, Y. J., Ruan, S. & Peng, Z. Black Phosphorus Quantum Dots with Tunable Memory Properties and Multilevel Resistive Switching Characteristics. *Adv. Sci.* **4**, 1600435 (2017).
34. Xu, L., Sun, J., Tang, T., Zhang, H., Sun, M., Zhang, J. & Wong, W. Y. Metallated Graphynes as a New Class of Photofunctional 2D Organometallic Nanosheets. *Angew. Chem. Int. Ed.* **60**, 11326–11334 (2021).
35. Zhang, Y. Q., Paintner, T., Hellwig, R., Haag, F., Allegretti, F., Feulner, P. & Klappenberger, F. Synthesizing Highly Regular Single-Layer Alkynyl-Silver Networks at the Micrometer Scale via Gas-Mediated Surface Reaction. *J. Am. Chem. Soc.* **141**, 5087–5091 (2019).
36. Yang, Z., Sander, T., Gebhardt, J., Schaub, T. A., Schonamsgruber, J., Soni, H. R. & Maier, S. Metalated Graphyne-Based Networks as Two-Dimensional Materials: Crystallization, Topological Defects, Delocalized Electronic States, and Site-Specific Doping. *ACS Nano* **14,** 16887–16896 (2020).
37. Zhang, T., Xu, S., Hou, Y., Chai, G., Olianas, D., Liao, Z. & Feng, X. Solvent-Mediated Engineering of Copper-Metalated Acetylenic Polymer Scaffolds with Enhanced Photoelectrochemical Performance. *J. Mater. Chem. A* **9**, 9729–9734 (2021).
38. Zhan, X., Kang, H., Qian, F., Xu, L., Zheng, Y. & Huang, Z. Magnetic Investigation on the Two-Dimensional Metallated Graphdiyne Nanosheets. *J. Alloys. Compd.* **940,** 168693 (2023).
39. Fujikura, Y., Sonogashira, K. & Hagihara, N. Preparation and UV Spectra of Some

Oligomer-Complexes Composed of Platinum Group Metals and Conjugated Polyyne Systems. *Chem. Lett.* **66**, 067–1070 (1975).

40. Lewis, J., Raithby, P. R. & Wong, W. Y. Synthesis of New Bis(acetylide)-Substituted Fluorene Derivatives and Their Bimetallic and Polymeric Complexes. *J. Organomet. Chem.* **556**, 219–228 (1998).
41. Wong, W. Y. Recent Advances in Luminescent Transition Metal Polyyne Polymers. *J. Inorg. Organomet. Polym. Mater.* **15**, 197–219 (2005).
42. Wong, W. Y. & Ho, C. L. Di-, Oligo- and Polymetallaynes: Syntheses, Photophysics, Structures and Applications. *Coord. Chem. Rev.* **250**, 2627–2690 (2006).
43. Sina, A. A. I., Al-Rafia, S. I., Ahmad, M. F., Paul, R. K., Islam, S. S., Younus, M. & Wong, W. Y. Synthesis, Structures and Properties of Novel Platinum(II) Acetylide Complexes and Polymers with Tri(tolyl)phosphine as the Auxiliary Ligand. *J. Inorg. Organomet. Polym. Mater.* **25,** 427–436 (2014).
44. Wang, K., Cheng, X., Xia, W., Lian, H., Dou, Z., Zhang, Y. & Dong, Q. Regulating WORM/Flash Electrical Memory Behavior of Metallopolymers through Varying Metal Centers. *J. Organomet. Chem.* **983,** 122563 (2023).
45. Abd-EI-Aziz, A. S. Organometallic Polymers of the Transition Metals. *Macromol. Rapid. Commun.* **23**, 995–1031 (2002).
46. Charles, J. & Muthusamy, S. Comparative Study of Butyl Rubber (IIR) and Bromobutyl Rubber (BIIR) based on FTIR, Dielectric and Thermal Studies. *J. Appl. Sci. Eng. Methodol.* **2**, 206–211 (2016).
47. Kulkarni, R., Huang, J., Trunk, M., Burmeister, D., Amsalem, P., Müller, J. & Bojdys, M. J. Direct Growth of Crystalline Triazine-Based Graphdiyne using Surface-Assisted Deprotection-Polymerisation. *Chem. Sci.* **12**, 12661–12666 (2021).
48. Sato, Y., Itoh, K., Hagiwara, R., Fukunaga, T. & Ito, Y. On the So-Called "Semi-ionic" C–F Bond Character in Fluorine–GIC. *Carbon* **42**, 3243–3249 (2004).

49. Brar, A. S. & Kapur. G. S. Sequence Determination in Methyl Methacrylate-n-Butyl Methacrylate Copolymers by ^{13}C NMR Spectroscopy *Polym. J.* **20**, 811–817 (1988)).

50. Britton, D., Heatley, F. & Lovell, P. A. ^{13}C NMR Spectroscopy Studies of Branching and Sequence Distributionin Copolymers of Vinyl Acetate andn-Butyl Acrylate Prepared by Semibatch Emulsion Copolymerization. *macromolecules* **34**, 817–882 (2001).

51. Borovik, A. S., Bott, S. G. & Barron, A. R. Arene-Mercury Complexes Stabilized Aluminum and Gallium Chloride: Synthesis and Structural Characterization. *J. Am. Chem. Soc.* **123**, 11219–11228 (2001).

52. Wang, L., Wan, Y., Ding, Y., Wu, S., Zhang, Y., Zhang, X. & Xu, H. Conjugated Microporous Polymer Nanosheets for Overall Water Splitting Using Visible Light. *Adv. Mater.* **29,** 1702428 (2017).

53. Battocchio, C., Fratoddi, l. & Vittoria, R. M. H_2S Gas Interaction with Pt(II)-Containing Polymetallaynes of Selected Chain Length:An XPS and EXAFS Study. *J. Phys. Chem. A* **112**, 7365–7373 (2008).

54. Wang, F., Zuo, Z., Li, L., Li, K., He, F., Jiang, Z. & Li, Y. Large-Area Aminated-Graphdiyne Thin Films for Direct Methanol Fuel Cells. *Angew. Chem. Int. Ed.* **58**, 15010–15015 (2019).

55. Waser, R., Dittmann, R., Staikov, G. & Szot, K. Redox-based Resistive Switching Memories–Nanoionic Mechanisms, Prospects, and Challenges. *Adv. Mater.* **21**, 2632–2663 (2009).

56. Shiraishi, Y., Takii, T., Hagi, T., Mori, S., Kofuji, Y., Kitagawa, Y. & Hirai, T. Resorcinol-Formaldehyde Resins as Metal-Free Semiconductor Photocatalysts for Solar-to-Hydrogen Peroxide Energy Conversion. *Nat. Mater.* **18**, 985–993 (2019).

57. Goswami, S., Rath, S. P., Thompson, D., Hedström, S., Annamalai, M., Pramanick, R. & Venkatesan, T. Charge Disproportionate Molecular Redox for Discrete Memristive and Memcapacitive Switching. *Nat. Nanotechnol* **15**, 380–389 (2020).

58. Park, H. L., Kim, M. H., Kim, H. & Lee, S. H. Self-Selective Organic Memristor by Engineered Conductive Nanofilament Diffusion for Realization of Practical Neuromorphic System. *Adv. Electron. Mater.* **7,** 2100299 (2021).

Chapter 4

Synthesis and Properties of Nickel Graphynes and Application Studies in the Photocatalytic CO_2 Reduction to CO

4.1 Introduction

The rapid development of human society since the Industrial Revolution has intensified the use of non-renewable fossil fuels (such as coal, oil, and natural gas). Heavy reliance on these fossil fuels has gradually destroyed the balance of the carbon cycle, leading to an explosive increase in carbon dioxide (CO_2) emissions, which has led to serious global warming problems[1-4]. Therefore, effective capture and utilization of CO_2 has become an increasingly urgent issue. To date, photocatalytic CO_2 reduction reaction (CO_2RR) that utilizes clean and abundant solar energy to mimic natural photosynthesis is considered as a carbon-neutral and sustainable strategy to convert CO_2 into high-value-added chemical energy, thereby solving global energy and environmental issues[5-8]. In the past few decades, great efforts have been made mainly on various traditional semiconductor photocatalysts including metal oxides, metal dichalcogenides, and metals/metal-oxides composites[9-14]. However, problems such as poor CO_2 adsorption capacity, low intermolecular electron transfer efficiency, low reaction activity, and poor product selectivity still exist for the CO_2 transformation. To overcome these problems, two-dimensional (2D) materials, such as covalent organic frameworks (COFs)[15,16], metal-organic frameworks (MOFs)[17,18], metal–covalent organic frameworks (MCOFs)[19], and graphdiyne (GDY)[20], have shown great

advantages due to their higher surface area-to-volume ratio that facilitates solar energy collection, atomic-level thickness that can reduce carrier recombination, and sufficient surface coordination. Unsaturated sites can serve as active centers[21,22].

Recently, metallated graphynes (MGYs), as a new class of functional 2D materials consisting of aromatic rings and –C≡C–M–C≡C– linkage, have attracted great attention because they combine the advantages both of GDY and single metal atoms, such as highly ordered pores, high π conjugation, and large surface area[23-25]. More importantly, the metals in the –C≡C–M–C≡C– linkage tend to become possibly catalytically active centers and are relatively stable when compared to metal-anchored 2D materials. Moreover, the easy delocalization of electrons in high-energy acetylenic bonds helps improve the electron transfer rate of the material[26,27]. Hg-GYs, Cu-GYs, and Co-GYs have been explored as efficient photo- and electro-2D catalysts for hydrogen evolution reaction (HER), oxygen reduction reaction (ORR), or CO_2RR[28-30]. In another aspect, the transition metal, nickel (Ni), has been suggested to promote the efficiency of photocatalytic CO_2RR with nanomaterials anchored with single-atom Ni, such as Ni–N–C catalysts and Ni-single atom catalysts (Ni-SACs)[31-33]. Therefore, nickel graphynes (Ni-GYs) can be expected to be a promising 2D material for efficient photocatalytic CO_2RR. In addition, organic units in 2D materials can also affect the performance of CO_2RR by systematically adjusting electron-withdrawing groups or electron-donating groups[34]. Furthermore, different groups in the organic unit will change the electron mobility of the material, which is also crucial to the CO_2RR performance[35]. Generally,

the photocatalytic CO_2RR mainly involves three processes: (i) the semiconductor material absorbs light to generate electron-hole pairs, (ii) the electron-hole pairs are separated and transferred to the surface of the semiconductor material, and (iii) CO_2RR occurs on the surface of semiconductor materials[36]. However, an understanding of the entire reaction process for the complete mechanism still needs to be explored deeply.

Herein, we reported a series of Ni-GYs with different organic struts (**TEPB-Ni-GY**, **TEPT-Ni-GY**, **NH_2-Ni-GY**, and **F-Ni-GY**) and studied the effect of the introduction of different functional groups on their crystal structures, electronic structures, and their photocatalytic CO_2RR performance. It is found that the introduction of heteroatoms or active groups has an important effect on their electronic structures and their performance of photocatalytic CO_2RR. The photocatalytic CO_2RR performance showed that all the **Ni-GYs** show good performance of photocatalytic CO_2RR under visible-light irradiation ($\lambda \geq 420$ nm) with photosensitizer of ruthenium terpyridine and electron donor of TEOA in the mixed solvents (V_{ACN}/V_{H2O} = 5:1), and the CO production rate of **NH_2-Ni-GY**, **F-Ni-GY, TEPT-Ni-GY, and TEPB-Ni-GY** is 4.78, 5.84, 6.23, and 9.08 mmol g^{-1} h^{-1}, respectively. Notably, comprehensive experiments and DFT calculations revealed that Ni atoms in the skeleton act as the catalytic centers, and the heteroatoms or active groups in organic struts (N, F, and NH_2) can increase the electron density of Ni atoms and alter the electron distribution around Ni atoms. This work reveals the relationship between the structures of Ni-GYs and their photocatalytic CO_2RR performance, providing a general guidance for the design of

more competitive photocatalysts.

4.2 Synthesis and characterization of nickel graphynes

4.2.1 Synthesis of the organic ligands

The platinum complex of ***trans*-Ni(PBu$_3$)$_2$Cl$_2$** was prepared from the reaction of $NiCl_2$•$6H_2O$ with tributylphosphine (PBu_3) and the synthetic routes are shown in Figure 4.1. The structure of ***trans*-Ni(PBu$_3$)$_2$Cl$_2$** was characterized by ^{1}H NMR, ^{13}C NMR, and ^{31}P NMR (Details are shown in Chapter 5). The synthetic routes of the designed organic ligands (**TEPB**, **TEPT**, **TEBA**, and **TEFB**) were the same as Figure 2.1 in Chapter 2, which were no longer displayed here.

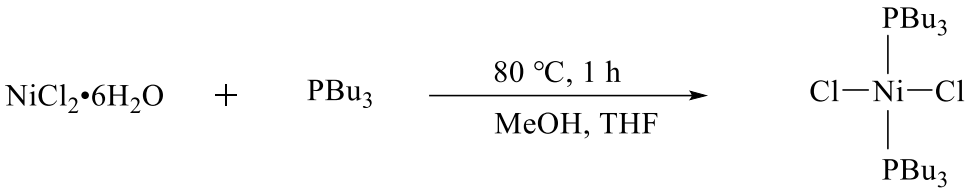

Figure 4.1 Synthetic route of ***trans*-Ni(PBu$_3$)$_2$Cl$_2$**

4.2.2 Synthesis of the nickel graphynes

TEPB-Ni-GY, **TEPT-Ni-GY**, **NH$_2$-Ni-GY**, and **F-Ni-GY** were synthesized via the base-catalyzed dehydrohalogenation reactions from the ligands of **TEPB**, **TEPT**, **TEBA**, and **TEFB** with ***trans*-Ni(PBu$_3$)$_2$Cl$_2$**, respectively, as shown in Figure 4.2. (details are shown in Chapter 5). What's more, it was found that **TEPT-Ni-GY** can be obtained at room temperature (RT) in comparison of lower yield of **TEPB-Ni-GY**, **NH$_2$-Ni-GY**, and **F-Ni-GY** at RT, which indicated that TEPT is easier to coordinate with ***trans*-Pt(PBu$_3$)$_2$Cl$_2$** than **TEPB**, **TEBA**, and **TEFB**.

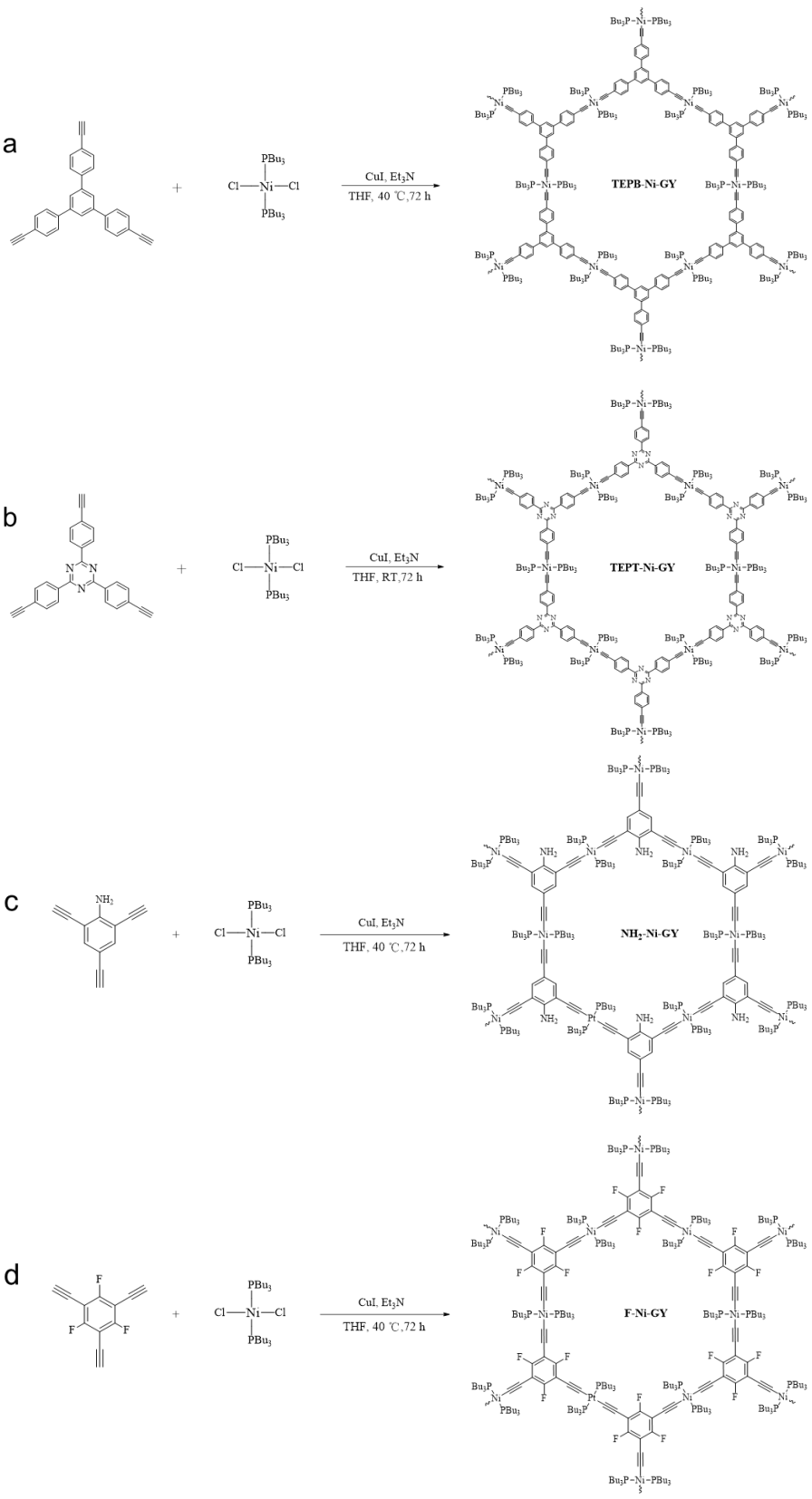

Figure 4.2 Synthetic routes of the nickel graphynes of (a) **TEPB-Ni-GY**, (b) **TEPT-Ni-GY**, (c) **NH_2-Ni-GY**, and (d) **F-Ni-GY.**

4.2.3 Characterization of the nickel graphynes

To comprehensively characterize the chemical structures of Ni-GYs, we first performed their FTIR spectra, as shown in Figure 4.3. The sharp peaks at ≈ 3200 cm^{-1} of the organic ligands can be assigned to the ≡C–H stretching vibrations and disappeared in the FTIR spectra of the Ni-GYs, which indicated that the base-catalyzed dehydrohalogenation reactions were completed[23]. What's more, the characteristic absorption peaks at about 2950 cm^{-1}, 2920 cm^{-1}, and 2860 cm^{-1} in all spectra correspond to the saturated C–H stretching vibrations of the butyl groups[37], indicating that *trans*-$Ni(PBu_3)_2Cl_2$ coordinated successfully with the as-designed organic ligand.

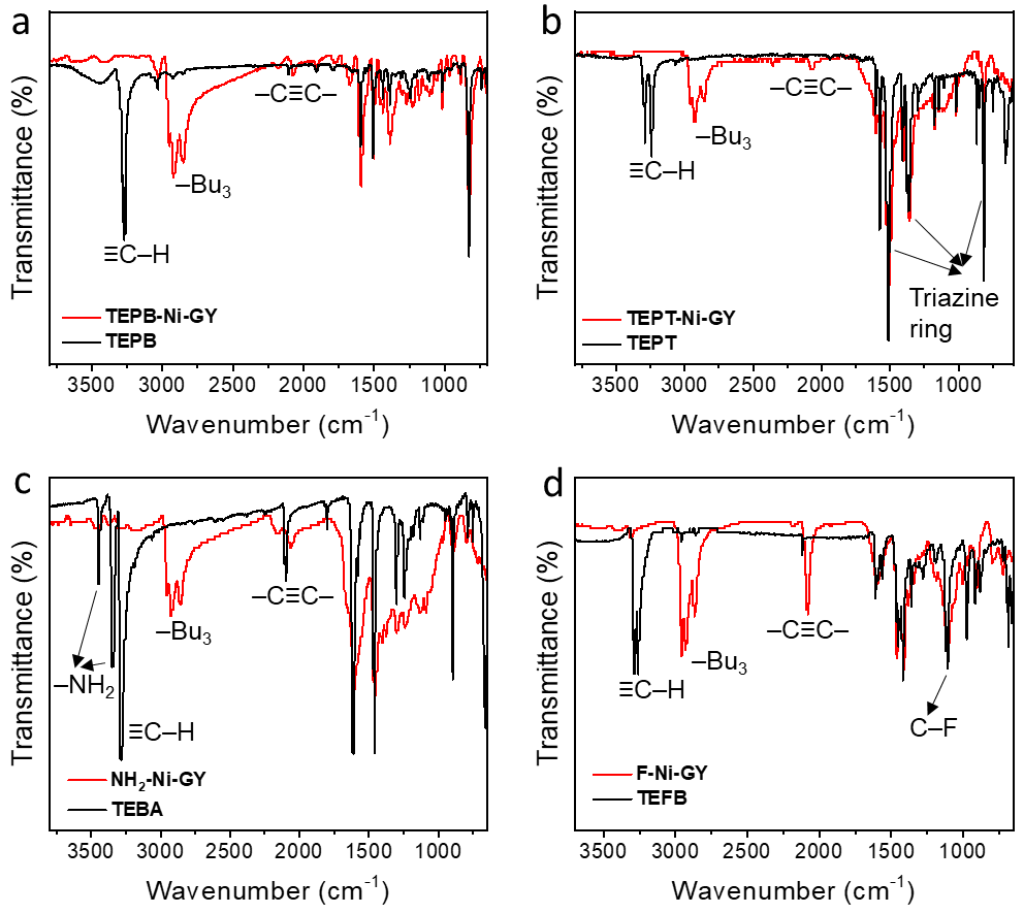

Figure 4.3 FTIR spectra of the nickel graphynes and their corresponding organic ligands of (a) **TEPB-Ni-GY**, (b) **TEPT-Ni-GY**, (c) **NH_2-Ni-GY**, and (d) **F-Ni-GY**.

In addition, for **TEPT-Ni-GY**, the peaks at 1516 cm^{-1}, 1359 cm^{-1}, and 820 cm^{-1} (Figure 4.3b) can be assigned to the triazine ring[38]. Furthermore, for **NH_2-Ni-GY**, the peaks at 3300-3400 cm^{-1} can be assigned to the typical absorption peaks of amine groups for its symmetrical and asymmetrical stretching vibration[39]. For **F-Ni-GY**, the peak at 1110 cm^{-1} can be assigned to the semi-ionic C–F bond[40]**,** which showed that the heteroatoms or active groups retained in the frameworks.

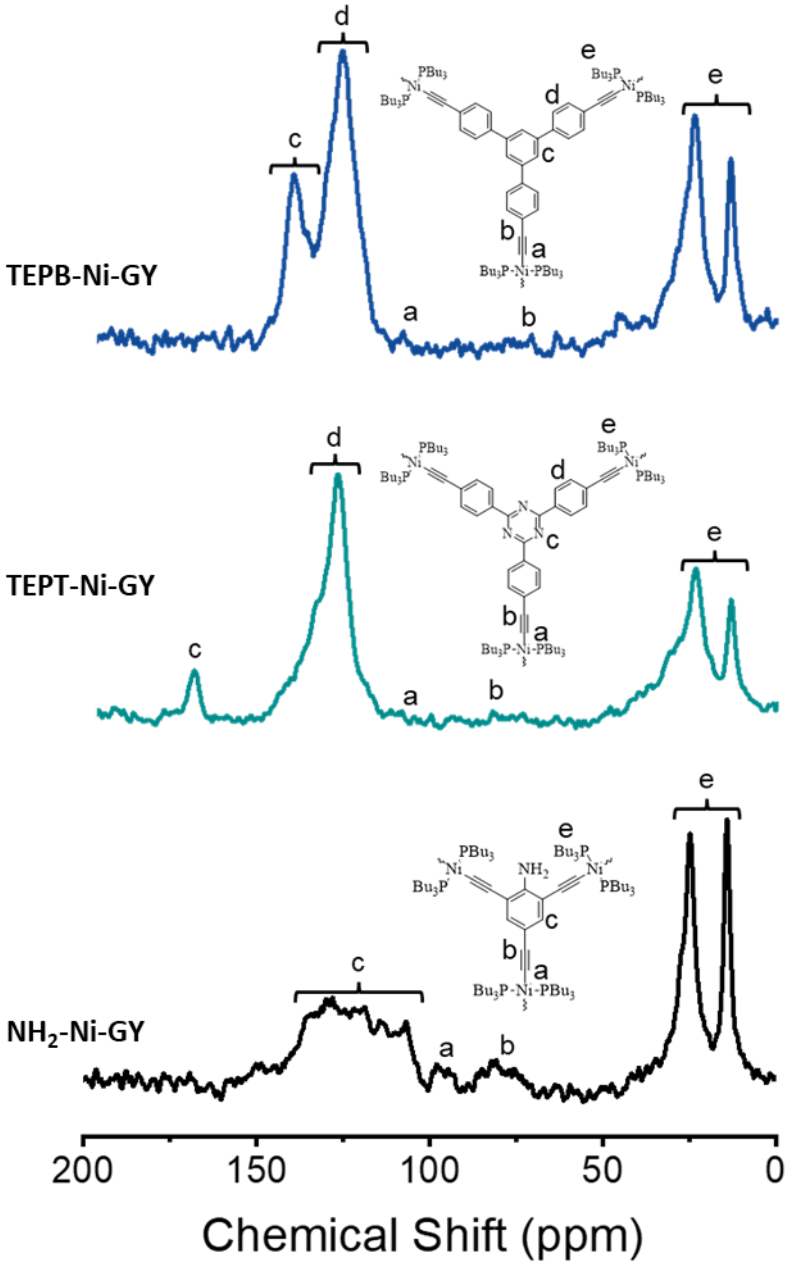

Figure 4.4 Solid-state ^{13}C NMR spectra of **TEPB-Ni-GY**, **TEPT-Ni-GY**, **and NH_2-Ni-GY**.

The solid-state ^{13}C cross-polarization magic-angle spinning NMR was then performed to verify their chemical structures, as shown in Figure 4.4. It can be seen from all the spectra that the peaks at ≈ 8 and ≈ 19 ppm indicate the presence of the butyl groups in Ni-GYs[41,42], and the peaks at ≈ 80 and ≈ 110 ppm can be assigned to the carbon atoms in the –C≡C–Ni–C≡C– moieties[43]. In addition, the peaks in the range of 120–140 ppm in the top spectra can be attributed to the phenyl groups in Ni-GYs[44]. What's more, the peak at ≈170 ppm in the bottom spectra can be assigned to triazine groups in **TEPT-Ni-GY**[38]. These assignments verify the structure of the design and are consistent well with the results from FTIR spectra. On the other hand, XPS was conducted to illustrate the chemical states of the existing elements in Ni-GYs. The full-XPS spectra of **TEPB-Ni-GY** (Figure 4.5a) showed that the binding energy of 285.07, 190.28, 132.87, 69.44, and 874.47 and 856.33 eV can be ascribed to C 1s, P 2s, P 2p, Ni 3p, Ni $2p_{1/2}$, and Ni $2p_{3/2}$, respectively[45]. For **TEPT-Ni-GY**, the binding energy of N 1s was 399.25 eV and the binding energy of C 1s, P 2s, P 2p, Ni 3p, Ni $2p_{1/2}$, and Ni $2p_{3/2}$ were 285.07, 190.31, 132.56, 68.70, and 874.22 and 856.52 eV, respectively (Figure 4.5b). For **NH_2-Ni-GY**, the binding energy of N 1s was 399.88 eV and the binding energy of C 1s, P 2s, P 2p, Ni 3p, Ni $2p_{1/2}$, and Ni $2p_{3/2}$ were 285.07, 189.45, 133.49, 68.07, and 874.01 and 856.67 eV, respectively (Figure 4.5c). For the **F-Ni-GY**, the XPS spectra showed that the binding energy of 832.62 and 685.58 eV were assigned to F KLL (Auger transition) and F 1s and the binding energy of C 1s, P 2s, P 2p, Ni 3p, Ni $2p_{1/2}$, and Ni $2p_{3/2}$ were 285.90, 190.37, 132.59, 68.78, and 875.06 and 856.68 eV,

respectively (Figure 4.5d). These assignments of the elements for all Ni-GYs showed that the introduction of heteroatoms and active groups hardly affects the chemical states of the metal elements.

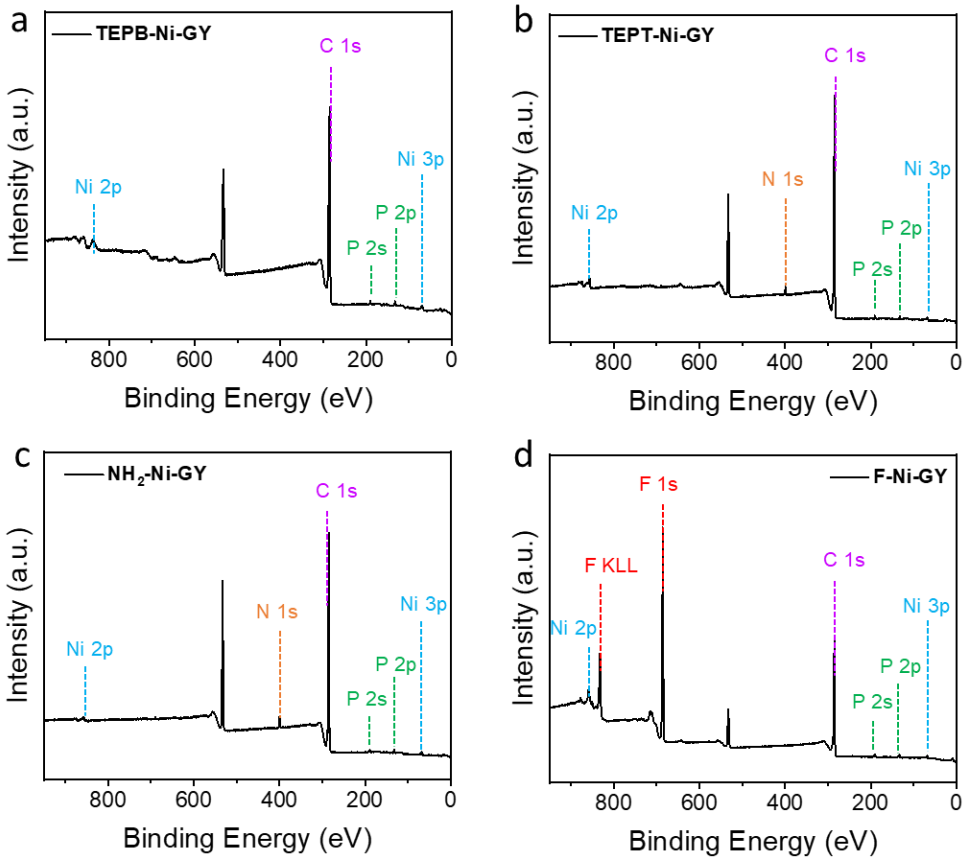

Figure 4.5 XPS spectra of (a) **TEPB-Ni-GY**, (b) **TEPT-Ni-GY**, (c) **NH_2-Ni-GY**, and (d) **F-Ni-GY**.

The morphologies of **TEPB-Ni-GY**, **TEPT-Ni-GY**, **NH_2-Ni-GY**, and **F-Ni-GY** were characterized by TEM images. Low resolution of TEM images (Figure 4.6a–d) demonstrated that all the Ni-GYs possessed a layered structure. In addition, HRTEM images shown in Figures 4.7 revealed that the interlayer distance of the Ni-GYs was ~0.44 nm, which indicated that they have the same interlayer distance as that of Pt-GYs because these two series of MGYs have almost the same chemical structures. Their interlayer distances are larger than those of Hg-GYs due to the presence of PBu_3 units in the skeleton.

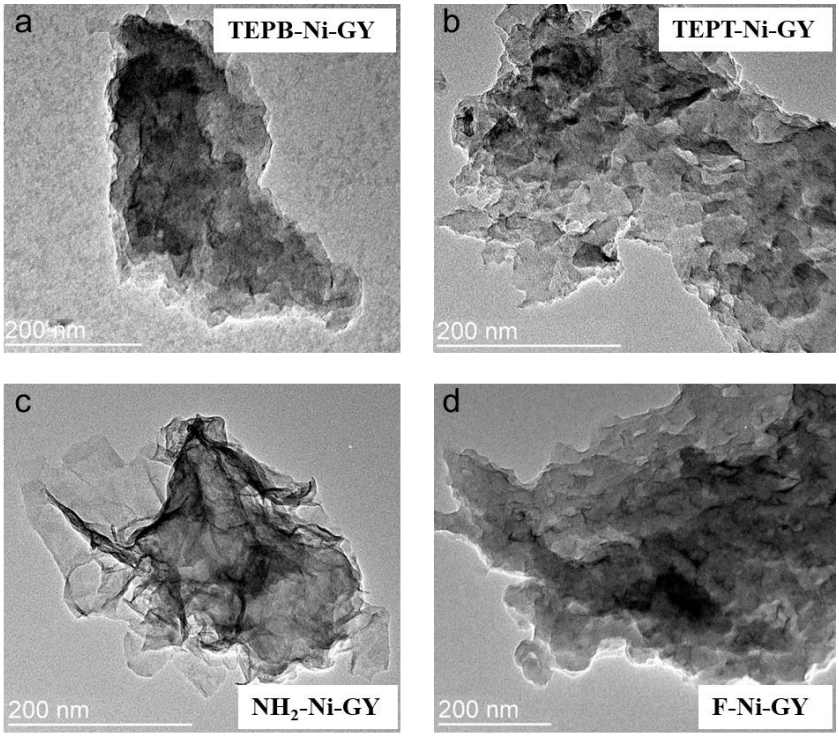

Figure 4.6 Low-resolution TEM images of (a) **TEPB-Ni-GY**, (b) **TEPT-Ni-GY**, (c) **NH_2-Ni-GY**, and (d) **F-Ni-GY**.

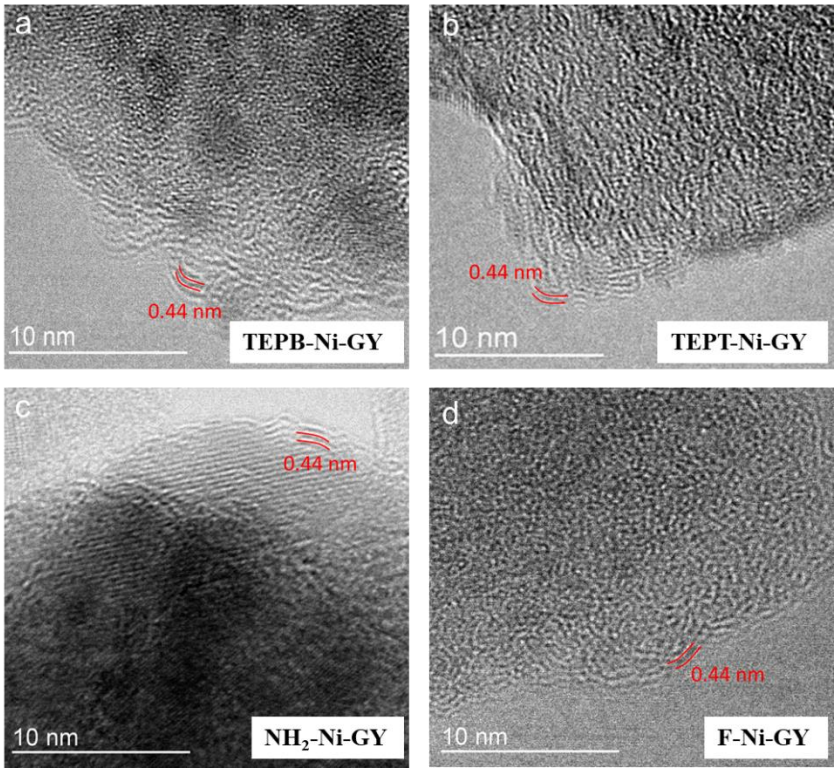

Figure 4.7 High-resolution TEM images of (a) **TEPB-Ni-GY**, (b) **TEPT-Ni-GY**, (c) **NH_2-Ni-GY**, and (d) **F-Ni-GY**.

To explore the crystal natures of **TEPB-Ni-GY**, **TEPT-Ni-GY**, **NH_2-Ni-GY**, and **F-Ni-GY**, their PXRD patterns were conducted (Figure 4.8). It can be concluded that all the Ni-GYs were featured with the same crystal type and showed the same diffraction peaks at the 2θ angles of about 10° and 20° In addition, we can also see from the spectra that the intensity of patterns remained unchanged among different samples, which revealed that the organic ligands can also have little influence on their crystallinity. On the other hand, the diffraction peak at the 2θ angle of ≈ 20° can be assigned to the interlayer distance with 0.44 nm[46].

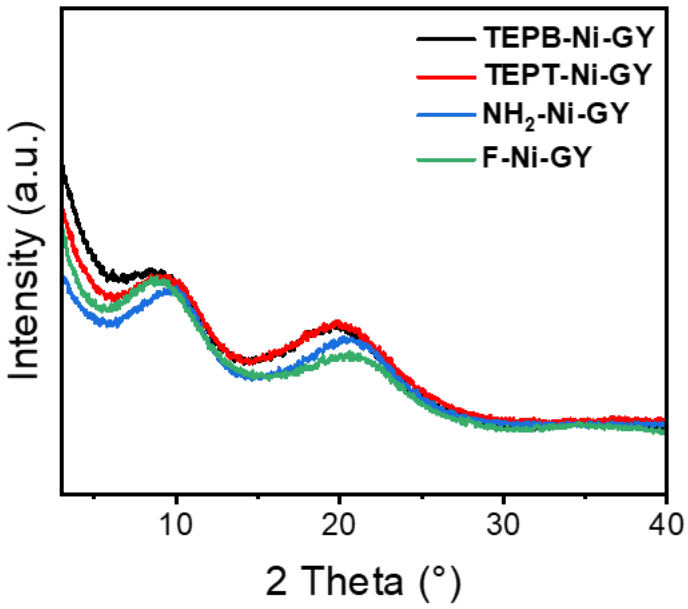

Figure 4.8 PXRD patterns of **TEPB-Ni-GY**, **TEPT-Ni-GY**, **NH_2-Ni-GY**, and **F-Ni-GY**.

Finally, the thermal stability of **TEPB-Ni-GY**, **TEPT-Ni-GY**, **NH_2-Ni-GY**, and **F-Ni-GY** was analyzed by TGA, as shown in Figure 4.9. It can be seen from the TGA curves that the onset decomposition temperature of all the samples is about 180 °C, which indicated their good thermal stability. Furthermore, it can be concluded that the thermal stability of Ni-GYs is lower than those of Pt-GYs and Hg-GYs, which may be due to the fact that the bond strength of nickel-acetylene is smaller that of platinum-

acetylene and mercury-acetylene.

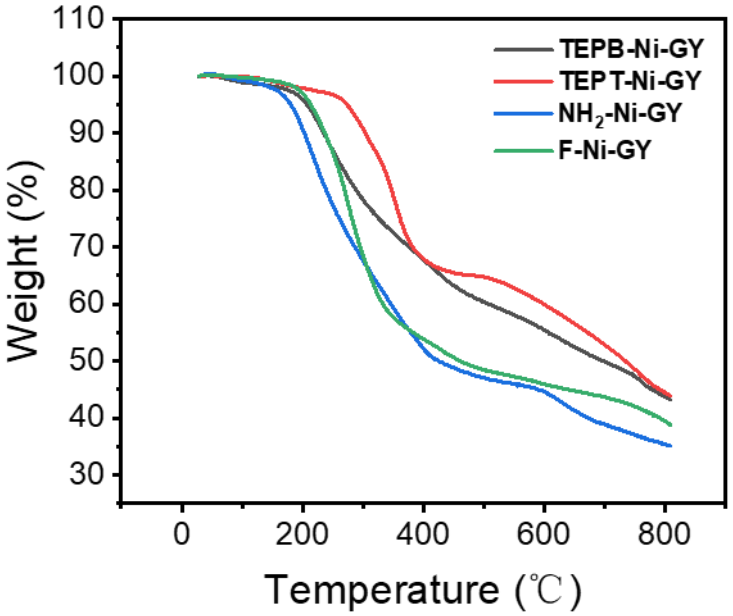

Figure 4.9 TGA curves of **TEPB-Ni-GY**, **TEPT-Ni-GY**, **NH_2-Ni-GY**, and **F-Ni-GY**.

4.3 Properties of nickel graphynes

As we all know, the catalytic performance of materials has a big relationship with their basic properties, such as the type of semiconductor, the band structure, and the electron transport capability. Therefore, UV–Vis DRS, UPS, M–S electrochemical measurements, and EIS were conducted. Firstly, their semiconductor type was studied by the M–S electrochemical measurements, as shown in Figure 4.10. M–S curves showed that all the Ni-GYs are n-type semiconductors, indicating that Ni-GYs are suitable for the catalytic reduction reaction. In addition, the M–S curves also demonstrated that the CB potential of **TEPB-Ni-GY**, **TEPT-Ni-GY**, **NH_2-Ni-GY**, and **F-Ni-GY** is −0.30, −0.80, −0.80, and −0.60 V, respectively (V vs RHE).

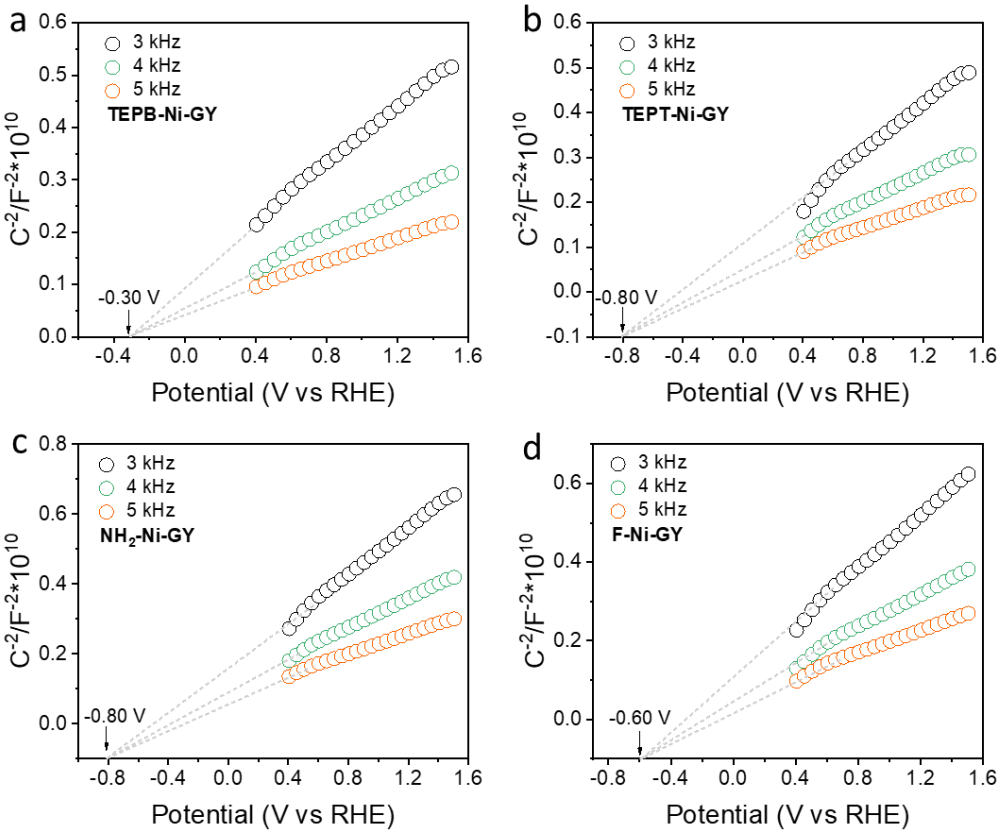

Figure 4.10 M-S curves of (a) **TEPB-Ni-GY**, (b) **TEPT-Ni-GY**, (c) **NH_2-Ni-GY**, and (d) **F-Ni-GY**.

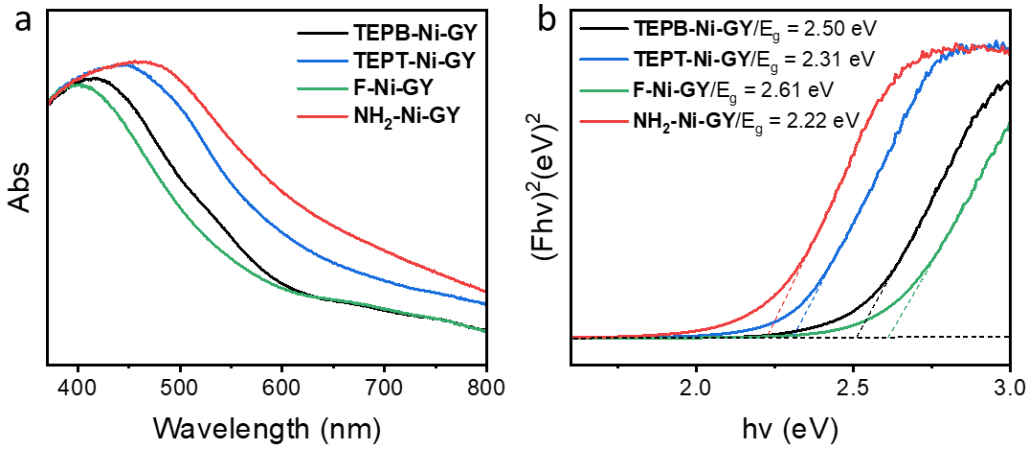

Figure 4.11 (a) UV−Vis spectra and (b) Tauc's plots of **TEPB-Ni-GY**, **TEPT-Ni-GY**, **NH_2-Ni-GY**, and **F-Ni-GY**.

UV–Vis spectroscopy was performed to explore the light absorbance and band structure. Figure 4.11a showed that all the samples possess good light absorption ability and revealed that the introduction of reactive groups and heteroatoms can change their

light absorption capability. In addition, it can be concluded that the introduction of amino groups and N atoms into Ni-GYs increase their light absorbance while the introduction of F atoms decreases the light absorbance. On the other hand, the corresponding Tauc's plots showed that the optical band gap (Eg) of **TEPB-Ni-GY**, **TEPT-Ni-GY**, **NH_2-Ni-GY**, and **F-Ni-GY** is 2.50, 2.31, 2.61, and 2.22 eV, respectively (Figure 4.11b). Furthermore, compared to Pt-GYs and Hg-GYs, Ni-GYs have the smallest band gap, which revealed that the nickel metal has the biggest ability to decrease the energy potential of MGYs. What's more, their VB potentials were demonstrated by UPS, as shown in Figure 4.12. Combined with Eg calculated from Tauc's plots, the E_{VBM} and E_{CBM} can be calculated by the following equations:

$$\Phi = E_{cutoff} - hv \quad (1)$$

$$E_{VBM} = \Phi - E_{edge} \quad (2)$$

$$E_g = E_{CBM} - E_{VBM} \quad (3)$$

where Φ is the work function, hv = 21.22 eV. Accordingly, the E_{VBM} of **TEPB-Ni-GY**, **TEPT-Ni-GY**, **NH_2-Ni-GY**, and **F-Ni-GY** were calculated to be 2.00, 1.31, 1.22, and 1.81 V (V vs. NHE), respectively. As a result, their E_{CBM} potentials were calculated as −0.50, −1.00, −1.00, and −0.80 V (V vs. RHE), respectively, which matched well with the CB potentials displayed from M–S data.

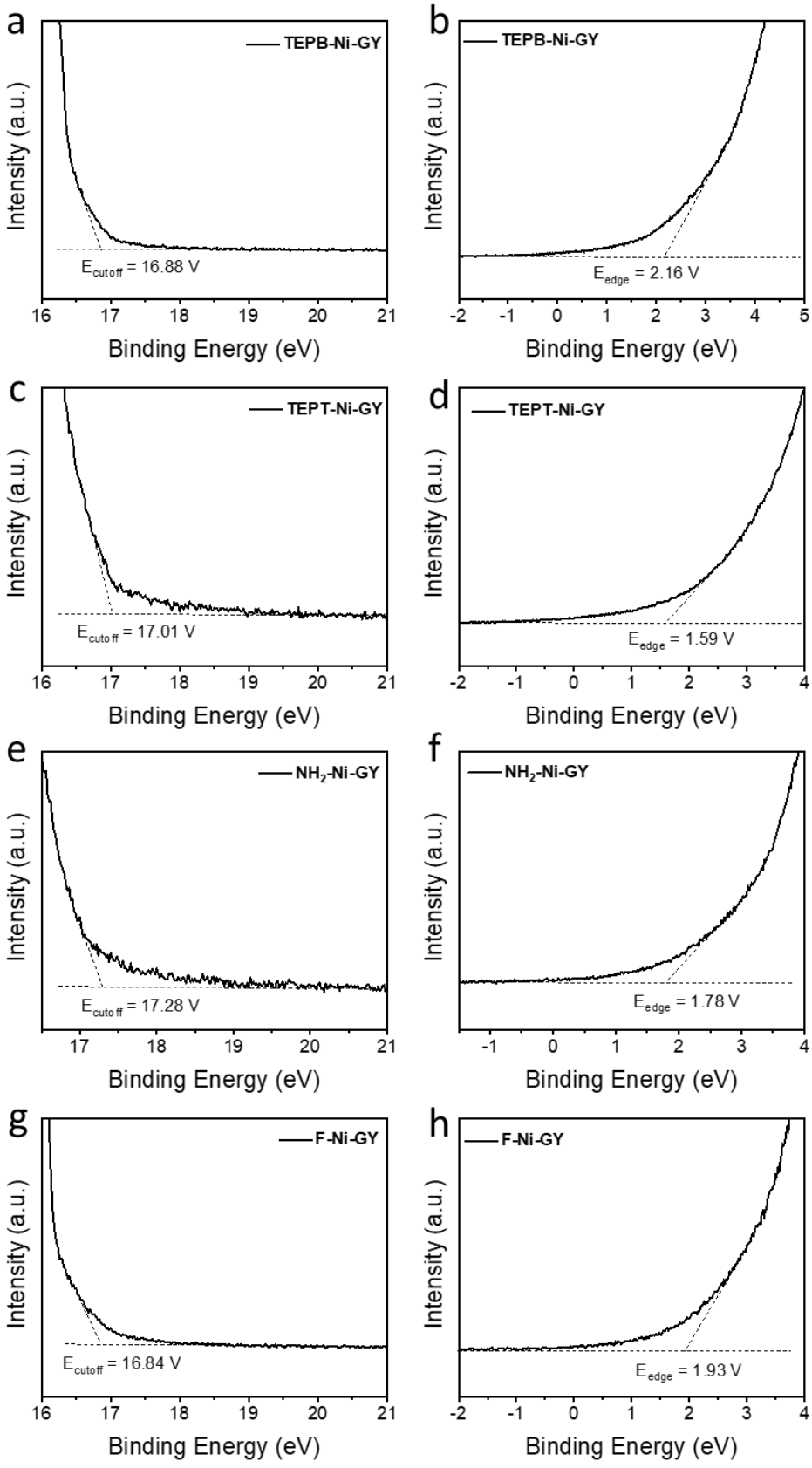

Figure 4.12 UPS of **TEPB-Ni-GY**, **TEPT-Ni-GY**, **NH_2-Ni-GY**, and **F-Ni-GY**.

Finally, the corresponding band energy levels were displayed in Figure. 4.13 and indicated that the introduction of heteroatoms has an important influence on the CB and VB potentials of Ni-GYs.

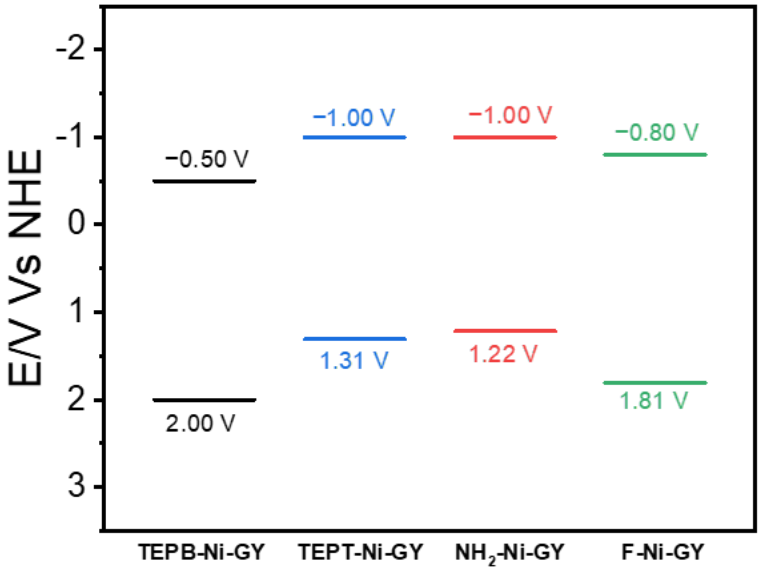

Figure 4.13 VB and CB positions of **TEPB-Ni-GY**, **TEPT-Ni-GY**, **NH_2-Ni-GY**, and **F-Ni-GY**.

EIS were conducted to explore their charge transfer ability, as shown in Figure 4.14. It was found from EIS that **NH_2-Ni-GY** has the best electronic conductivity with the smallest semicircles of the Nyquist plot among Ni-GYs and the fitting charge transfer rate (R_{ct}) of **TEPB-Ni-GY**, **TEPT-Ni-GY**, **NH_2-Ni-GY**, and **F-Ni-GY** is 30.01, 29.31, 27.35, and 24.01, respectively, indicating that the introduction of heteroatoms or active group can improve their electronic properties.

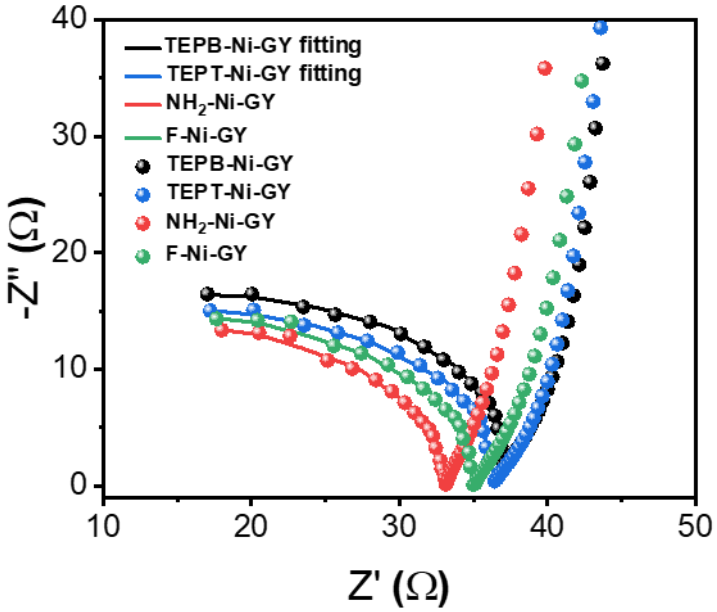

Figure 4.14 EIS curves of **TEPB-Ni-GY**, **TEPT-Ni-GY**, **NH_2-Ni-GY**, and **F-Ni-GY**.

4.4 Photocatalytic reduction of CO_2 to CO performance

We performed photocatalytic CO_2 reduction experiments with **TEPB-Ni-GY**, **TEPT-Ni-GY**, **NH_2-Ni-GY**, and **F-Ni-GY** under visible-light irradiation ($\lambda \geq 420$ nm) in the mixed solvents (V_{ACN}/V_{H2O} = 5:1) with photosensitizer (PS) of ruthenium terpyridine and electron donor of TEOA and found that all the samples exhibit a good performance of photocatalytic CO_2RR. It can be found that the CO production rate of **TEPB-Ni-GY**, **TEPT-Ni-GY**, **F-Ni-GY**, and **NH_2-Ni-GY** is 4.78, 5.84, 6.23, and 9.08 mmol g^{-1} h^{-1}, respectively, which indicated that the introduction of heteroatoms into the frameworks can improve the photocatalytic CO_2RR performance. To explore the catalytic path and the role of each component in the system, we conducted a series of control experiments under different catalytic conditions and the results are displayed in Table 1. It can be seen from the table that the CO production rate became very low

without any of the ingredients of ACN, H_2O, or PS. Accordingly, we can conclude that the role of the photosensitizer is to absorb light for the catalytic reaction system and Ni-GYs just act as catalysts. In addition, the electrons and protons for the catalytic reaction were provided by TEOA and water, respectively[47,48].

Table 4.1. CO production rate of **TEPB-Ni-GY**, **TEPT-Ni-GY**, **F-Ni-GY**, and **NH_2-Ni-GY** under different catalytic conditions.

Catalytic conditions	CO production rate of **TEPB-Ni-GY** (mmol g^{-1} h^{-1})	CO production rate of **TEPT-Ni-GY** (mmol g^{-1} h^{-1})	CO production rate of **F-Ni-GY** (mmol g^{-1} h^{-1})	CO production rate of **NH_2-Ni-GY** (mmol g^{-1} h^{-1})
ACN/H_2O/PS/TEOA	4.787	5.846	6.233	9.084
ACN/H_2O/TEOA	0.001	0.003	0.003	0.005
ACN/PS/TEOA	0.004	0.005	0.005	0.007
H_2O /PS/TEOA	0.002	0.003	0.004	0.006

Subsequently, we also performed the photocatalytic reactions with a long period to study the activity. It was found that the production of CO gradually increased in 5 h and showed a linear relationship within the first 5 h (Figure 4.15a). The CO production of **TEPB-Ni-GY**, **TEPT-Ni-GY**, **F-Ni-GY,** and **NH_2-Ni-GY** was found to be nearly 17, 20, 21, and 27 mmol g^{-1}, respectively, at 5 h, which exceeded the performance of the other reported 2D materials. In addition, all the Ni-GYs exhibited a good selectivity for CO production during the catalytic reaction. Figure 4.15b showed that compared to the competitive product of H_2, the selectivity for CO production of **TEPB-Ni-GY**, **TEPT-Ni-GY**, **F-Ni-GY**, and **NH_2-Ni-GY** reached 95%, 95%, 96%, and 98%,

respectively. The performance of Ni-GYs is relatively better than the other materials (listed in Table 4.2). Such findings revealed that the introduction of heteroatoms and amino groups can not only improve the activity of photocatalytic CO_2RR, but also enhance their selectivity, especially for F atoms and amino groups. Finally, cyclic tests were conducted to evaluate their stability. Figure 4.15c–f showed that all Ni-GYs exhibited good stability in the photocatalytic CO_2RR.

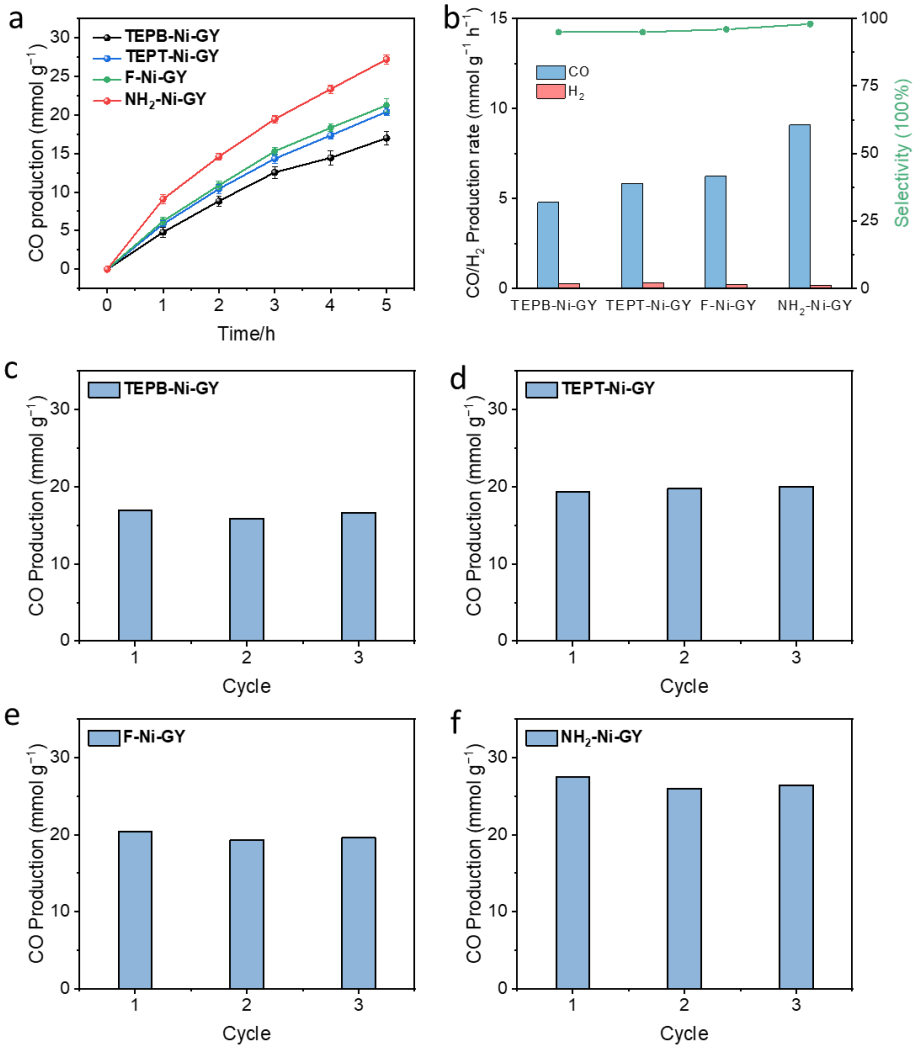

Figure 4.15 (a) CO production of **TEPB-Ni-GY**, **TEPT-Ni-GY**, **NH_2-Ni-GY**, and **F-Ni-GY** in 5 h. (b) CO/H_2 production rate of **TEPB-Ni-GY**, **TEPT-Ni-GY**, **NH_2-Ni-GY**, and **F-Ni-GY**. Repeatability performance of (c) **TEPB-Ni-GY**, (d) **TEPT-Ni-GY**, (e) **F-Ni-GY**, and (f) **NH_2-Ni-GY**.

Table 4.2. Photocatalytic CO_2 reduction systems in aqueous solution for CO production.

Photocatalyst	Irradiation condition	Selectivity	CO(μmol h^{-1} g^{-1})	Ref.
Ni MOLs $Ru(bpy)_3Cl_2$	5 W white LED light (400 nm ≤ λ ≤ 800 nm)	97.8%	12.5 μmol h^{-1} g^{-1}	49
$Ni_3(HITP)_2$ $Ru(bpy)_3Cl_2$	100 W LED light (λ = 420 nm)	97%	3.45×10^4μmol h^{-1} g^{-1}	50
spongy Ni(TPA/TEG) nanostructure $Ru(bpy)_3Cl_2$	300 W Xe lamp (λ > 420 nm)	nearly 100%	1.6×10^4 μmol h^{-1} g^{-1}	51
Ni-TpBpy $[Ru(bpy)_3]Cl_2$	300 W Xe lamp (λ ≥ 420 nm)	96 %	966 μmol h^{-1} g^{-1}	52
Co-ZIF-9 $[Ru(bpy)_3]Cl_2$	Xe lamp (λ > 420 nm)	58 %	TON: 89.6	53
Zr-UiO-66-NH_2 $[Ru(bpy)_3]Cl_2$	Xe lamp (λ > 420 nm)	35%	TON: 4.3	53
Re_3-MOF Ag nanocubes	300 W Xe lamp (λ = 400–700 nm)	100%	TON: 2.8	54
$Zr_6O_4(OH)_4$ $[Re(5,5bpydb)(CO)_3Cl]_6$	410 nm LED	94%	TON: 6.4	55
Re-COF	225 W Xe lamp (λ > 420 nm)	98%	~15 mmol CO/g > 20 h	56
MAF-X27-OH $Ru(bpy)_3Cl_2$	LED light (λ = 420 nm)	97%	$28\times10^{-3}s^{-1}$ (TOF)	57
Co1–G $Ru(bpy)_3Cl_2$	300 W Xe lamp (λ > 420 nm)	79%	TON: 374	58
Co_3O_4 hexagonal platelets $Ru(bpy)_3Cl_2$	300 W Xe lamp (λ > 420 nm)	77.1 %	2003 μmol h^{-1} g^{-1}	59
PCP-RuII $Ru(bpy)_3Cl_2$	300 W Xe lamp (λ = 385–740 nm)	15%	TON: 8.1	60
NH_2-Ni-GY	300 W Xe lamp (λ > 420 nm)	98%	9.1×10^4 μmol h^{-1} g^{-1}	This work
F-Ni-GY	300 W Xe lamp (λ > 420 nm)	96%	6.2×10^4 μmol h^{-1} g^{-1}	This work
TEPT-Ni-GY	300 W Xe lamp (λ > 420 nm)	96%	5.8×10^4 μmol h^{-1} g^{-1}	This work
TEPB-Ni-GY	300 W Xe lamp (λ > 420 nm)	96%	4.7×10^4 μmol h^{-1} g^{-1}	This work

To further explore the mechanism of superior performance of **TEPB-Ni-GY**, **TEPT-Ni-GY**, **F-Ni-GY**, and **NH_2-Ni-GY** toward photocatalytic CO_2RR, DFT calculations were conducted. It is noted that the density of electron on the metals has a great influence on the catalytic reactions as well as the electron distribution around metals. Generally, the higher the electron density in the metal centre, the better the performance of photocatalytic CO_2RR. Hence, reasonable models were built to perform DFT calculations to illustrate their electronic properties which related to the photocatalytic performance. The images of electrostatic potential (ESP), shown in Figure 4.16a–d, clearly showed the landscape of electrons and revealed that the electron density on nickel in **TEPT-Ni-GY**, **F-Ni-GY**, and **NH_2-Ni-GY** is higher than that in **TEPB-Ni-GY**, indicating that introduction of heteroatoms and amino groups into the frameworks can alter the electron distribution within Ni-GYs[34]. Therefore, the performance of **TEPT-Ni-GY**, **F-Ni-GY**, and **NH_2-Ni-GY** toward photocatalytic CO_2RR is improved with the enhanced electron density on the metal of nickel. What's more, it can be seen from the comparison of ESP images of **TEPB-Ni-GY** and **TEPT-Ni-GY** that the introduction of triazine into the frameworks enables **TEPT-Ni-GY** with a flatter two-dimensional surface, which is beneficial to the transmission of electrons on the surface.

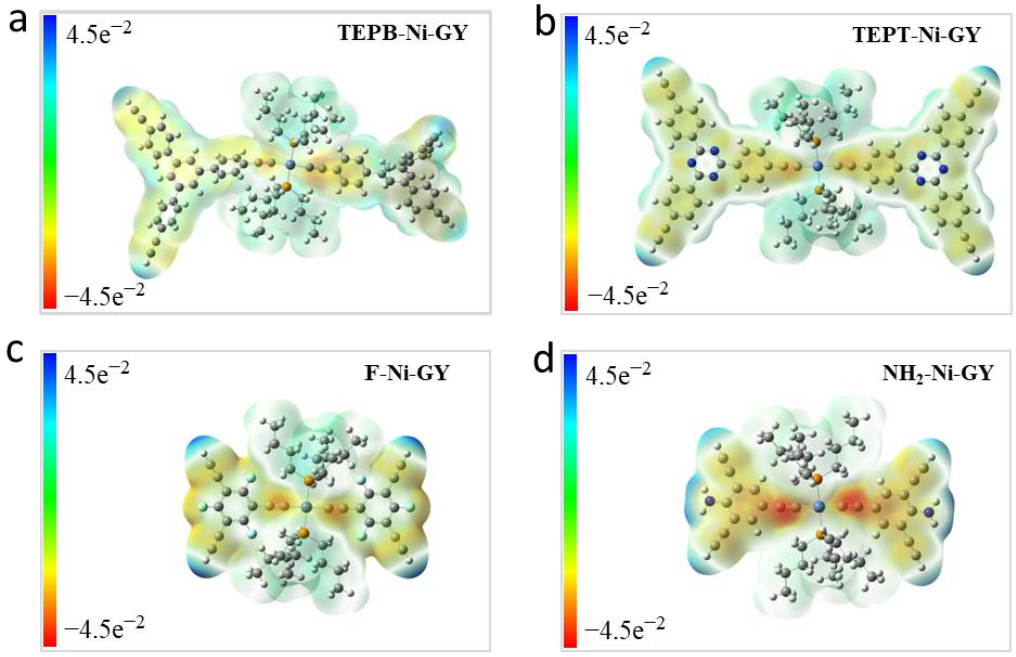

Figure 4.16 ESP images of (a) **TEPB-Ni-GY**, (b) **TEPT-Ni-GY**, (c) **NH_2-Ni-GY**, and (d) **F-Ni-GY**.

In order to analyse the electron distribution more intuitively, we calculated the Mulliken charges that can be used to characterize the electronic charge distribution in a molecule and the bonding nature of the molecular orbitals for particular pairs of atoms[62]. As displayed in Table 4.3, the Mulliken charge on nickel in **TEPB-Ni-GY**, **TEPT-Ni-GY**, **F-Ni-GY**, and **NH_2-Ni-GY** is −0.046, −0.058, −0.064, and −0.066 eV, respectively. In addition, the Mulliken charge on the C atoms of acetylene ($C_{\alpha 1}$, $C_{\beta 1}$, $C_{\alpha 2}$, and $C_{\beta 2}$) of **TEPB-Ni-GY**, **TEPT-Ni-GY**, **F-Ni-GY**, and **NH_2-Ni-GY** are also displayed in Table 2. Such analysis of Mulliken charge also demonstrates that heteroatoms and amino groups can help optimize the electron distribution in the frameworks, which are consistent well with ESP analysis.

Table 4.3. Mulliken charges on nickel and C atoms of acetylene ($C_{\alpha1}$, $C_{\beta1}$, $C_{\alpha2}$, and $C_{\beta2}$) of **TEPB-Ni-GY**, **TEPT-Ni-GY**, **F-Ni-GY**, and **NH_2-Ni-GY**.

Atom	Mulliken charges (eV) of **TEPB-Ni-GY**	Mulliken charges (eV) of **TEPT-Ni-GY**	Mulliken charges (eV) of **F-Ni-GY**	Mulliken charges (eV) of **NH_2-Ni-GY**
Nickel	−0.046	−0.058	−0.064	−0.066
$C_{\alpha1}$	−0.042	−0.056	−0.052	−0.096
$C_{\beta1}$	−0.054	−0.056	−0.052	−0.096
$C_{\alpha2}$	−0.204	−0.216	−0.215	−0.189
$C_{\beta2}$	−0.213	−0.216	−0.215	−0.189
–C≡C–Ni–C≡C– (α2 α1 β1 β2)				

4.5 Conclusion

In summary, we successfully synthesized a series of nickel graphynes of **TEPB-Ni-GY**, **TEPT-Ni-GY**, **F-Ni-GY**, and **NH_2-Ni-GY.** Firstly, their structures and morphologies were characterized comprehensively with FTIR, solid-state ^{13}C-NMR and XPS spectroscopy, PXRD patterns, and TEM images, which demonstrated that all the materials were prepared as designed and all the materials possess 2D structures in nanoscale. In addition, UV–Vis DRS, UPS, EIS, and M–S electrochemical measurements were performed to study their basic optoelectronic properties. Such characterizations illustrated that all the materials are n-type semiconductors, and the introduction of heteroatoms and amino groups can help alter their band structures, thus, improving their light absorption ability and charge transfer rate. Furthermore, photocatalytic CO_2RR was conducted and revealed that all the Ni-GYs exhibit a good

performance toward the CO_2-to-CO production. It is noted that **TEPT-Ni-GY**, **F-Ni-GY**, and **NH_2-Ni-GY** have a better performance with the CO production rates of 5.84, 6.23, and 9.08 mmol g^{-1} h^{-1}, respectively than that of **TEPB-Ni-GY** with the CO production rate of 4.78 mmol g^{-1} h^{-1}, which indicates that heteroatoms and amino groups can improve the photocatalytic CO_2RR performance of Ni-GYs. Besides, the DFT calculations further revealed the mechanisms that the introduction of heteroatoms and amino groups into frameworks can help optimize their electron distribution to achieve an enhanced electron density on the metal centers as well as their surrounding moieties, thus achieving a better performance toward photocatalytic CO_2RR. This is the first work example of using nickel graphynes in the application of photocatalytic CO_2RR, shedding fresh light on the future design for efficient photocatalysts.

References

1. Sorcar, S., Hwang, Y. & Grimes, C. A. Highly Enhanced and Stable Activity of Defect-Induced Titania Nanoparticles for Solar Light-Driven CO_2 Reduction into CH_4. *Mater. Today.* **20**, 507–515 (2017).
2. El-Khouly, M. E., El-Mohsnawy, E. & Fukuzumi, S. Solar Energy Conversion: From Natural to Artificial Photosynthesis. *J. Photochem. Photobiol. C* **31**, 36–83 (2017).
3. Cao, S., Shen, B., Tong, T., Fu, J. & Yu, J. 2D/2D Heterojunction of Ultrathin MXene/Bi_2WO_6 Nanosheets for Improved Photocatalytic CO_2 Reduction. *Adv. Funct. Mater.* **28**, 1800136 (2018).
4. Zeng, Z., Yan, Y., Chen, J., Zan, P., Tian, Q. & Chen, P. Boosting the Photocatalytic Ability of Cu_2O Nanowires for CO_2 Conversion by MXene Quantum Dots. *Adv. Funct. Mater.* **29**, 1806500 (2019).
5. Wagner, A., Sahm, C. D. & Reisner, E. Towards Molecular Understanding of Local Chemical Environment Effects in Electro- and Photocatalytic CO_2 Reduction. *Nat. Catal.* **3**, 775–786 (2020).
6. Ran, J., Jaroniec, M. & Qiao, S. Z. Cocatalysts in Semiconductor-based Photocatalytic CO_2 Reduction: Achievements, Challenges, and Opportunities. *Adv. Mater.* **30,** 1704649 (2018).
7. Arcudi, F., Dordevic, L., Nagasing, B., Stupp, S. I. & Weiss, E. A. Quantum Dot-Sensitized Photoreduction of CO_2 in Water with Turnover Number > 80,000. *J.*

Am. Chem. Soc. **143**, 18131–18138 (2021).

8. Lu, M., Liu, J., Li, Q., Zhang, M., Liu, M., Wang, J. L. & Lan, Y. Q. Rational Design of Crystalline Covalent Organic Frameworks for Efficient CO_2 Photoreduction with H_2O. *Angew. Chem. Int. Ed.* **58**, 12392–12397 (2019).
9. Lou, Z., Zhang, P., Li, J., Yang, X., Huang, B. & Li, B. Plasmonic Heterostructure TiO_2-MCs/WO_{3^-} x-NWs with Continuous Photoelectron Injection Boosting Hot Electron for Methane Generation. *Adv. Funct. Mater.* **29**, 1808696 (2019).
10. Xu, F., Meng, K., Cheng, B., Yu, J. & Ho, W. Enhanced Photocatalytic Activity and Selectivity for CO_2 Reduction over a TiO_2 Nanofibre Mat Using Ag and MgO as Bi-Cocatalyst. *ChemCatChem* **11**, 465–472 (2019).
11. Jin, J., Yu, J., Guo, D., Cui, C. & Ho, W. A Hierarchical Z-scheme CdS–WO_3 Photocatalyst with Enhanced CO_2 Reduction Activity. *Small* **11**, 5262–5271 (2015).
12. Kuehnel, M. F., Orchard, K. L., Dalle, K. E. & Reisner, E. Selective Photocatalytic CO_2 Reduction in Water through Anchoring of a Molecular Ni Catalyst on CdS Nanocrystals. *J. Am. Chem. Soc.* **139**, 7217–7223 (2017).
13. Yu, B., Zhou, Y., Li, P., Tu, W., Li, P., Tang, L. & Zou, Z. Photocatalytic Reduction of CO_2 over Ag/TiO_2 Nanocomposites Prepared with a Simple and Rapid Silver Mirror Method. *Nanoscale* **8**, 11870–11874 (2016).
14. Chong, R., Su, C., Du, Y., Fan, Y., Ling, Z., Chang, Z. & Li, D. Insights into the Role of MgAl Layered Double Oxides Interlayer in Pt/TiO_2 Toward Photocatalytic

CO_2 Reduction. *J. Catal.* **363**, 92–101 (2018).

15. Zhong, H., Sa, R., Lv, H., Yang, S., Yuan, D., Wang, X. & Wang, R. Covalent Organic Framework Hosting Metalloporphyrin-Based Carbon Dots for Visible-Light-Driven Selective CO_2 Reduction. *Adv. Funct. Mater.* **30,** 2002654 (2020).
16. Li, C., Ju, W., Vijay, S., Timoshenko, J., Mou, K., Cullen, D. A. & Strasser, P. Covalent Organic Framework (COF) Derived Ni–N–C Catalysts for Electrochemical CO_2 Reduction: Unraveling Fundamental Kinetic and Structural Parameters of the Active Sites. *Angew. Chem. Int. Ed.* **61**, e202114707 (2022).
17. Li, D., Kassymova, M., Cai, X., Zang, S. & Jiang, H. Photocatalytic CO_2 Reduction over Metal-Organic Framework-based Materials. *Coord. Chem. Rev.* **412**, 213262 (2020).
18. Chen, Y., Wang, D., Deng, X. & Li, Z. i. Metal–Organic Frameworks (MOFs) for Photocatalytic CO_2 Reduction. *Catal. Sci. Technol.* **7**, 4893–4904 (2017).
19. Dong, J., Han, X., Liu, Y., Li, H. & Cui, Y. Metal–Covalent Organic Frameworks (MCOFs): A Bridge Between Metal–Organic Frameworks and Covalent Organic Frameworks. *Angew. Chem. Int. Ed.* **59**, 13722–13733 (2020).
20. Xu, F., Meng, K., Zhu, B., Liu, H., Xu, J. & Yu, J. Graphdiyne: A New Photocatalytic CO_2 Reduction Cocatalyst. *Adv. Funct. Mater.* **29,** 1904256 (2019).
21. Liu, X., Yang, H., He, J., Liu, H., Song, L., Li, L. & Luo, J. Highly Active, Durable Ultrathin $MoTe_2$ Layers for the Electroreduction of CO_2 to CH_4. *Small* **14**, 1704049 (2018).

22. Li, F., Xue, M., Li, J., Ma, X., Chen, L., Zhang, X. & Zhang, J. Unlocking the Electrocatalytic Activity of Antimony for CO_2 Reduction by Two-Dimensional Engineering of the Bulk Material. *Angew. Chem. Int. Ed.* **56**, 14718–14722 (2017).

23. Xu, L., Sun, J., Tang, T., Zhang, H., Sun, M., Zhang, J., Xie, Z. & Wong, W. Y. Metallated Graphynes as a New Class of Photofunctional 2D Organometallic Nanosheets. *Angew. Chem. Int. Ed.* **60**, 11326–11334 (2021).

24. Liu, J., Chen, Q., Cai, K., Li, J., Li, Y., Yang, X. & Wu, K. Stepwise On-surface Dissymmetric Reaction to Construct Binodal Organometallic Network. *Nat. Commun.* **10**, 2545 (2019).

25. Zhang, Y. Q., Paintner, T., Hellwig, R., Haag, F., Allegretti, F., Feulner, P. & Klappenberger, F. Synthesizing Highly Regular Single-Layer Alkynyl-Silver Networks at the Micrometer Scale via Gas-Mediated Surface Reaction. *J. Am. Chem. Soc.* **141**, 5087–5091 (2019).

26. Zhao, Y., Wan, J., Yao, H., Zhang, L., Lin, K., Wang, L. & Wang, D. Few-layer Graphdiyne Doped with Sp-hybridized Nitrogen Atoms at Acetylenic Sites for Oxygen Reduction Electrocatalysis. *Nat. Chem.* **10**, 924–931 (2018).

27. Wang, S., Yi, L., Halpert, J. E., Lai, X., Liu, Y., Cao, H. & Li, Y. A Novel and Highly Efficient Photocatalyst Based on P_{25}–Graphdiyne Nanocomposite. *Small* **8**, 265–271 (2012).

28. Fang, M., Xu, L., Zhang, H., Zhu, Y. & Wong, W. Y. Metalloporphyrin-Linked Mercurated Graphynes for Ultrastable CO_2 Electroreduction to CO with nearly

100% Selectivity at a Current Density of 1.2 A cm^{-2}. *J. Am. Chem. Soc.* **144**, 15143–15154 (2022).

29. Zhang, T., Xu, S., Hou, Y., Chai, G., Olianas, D., Liao, Z. & Feng, X. Solvent-Mediated Engineering of Copper–Metalated Acetylenic Polymer Scaffolds with Enhanced Photoelectrochemical Performance. *J. Mater. Chem. A* **9**, 9729–9734 (2021).
30. Zhan, X., Kang, H., Qian, F., Xu, L., Zheng, Y. & Huang, Z. Magnetic Investigation on the Two-Dimensional Metallated Graphdiyne Nanosheets. *J. Alloys. Compd.* **940,** 168693 (2023).
31. Zhang, X., Wang, Y., Gu, M., Wang, M., Zhang, Z., Pan, W. & Liang, Y. Molecular Engineering of Dispersed Nickel Phthalocyanines on Carbon Nanotubes for Selective CO_2 Reduction. *Nat. Energy* **5**, 684–692 (2020).
32. Liang, S., Jiang, Q., Wang, Q. & Liu, Y. Revealing the Real Role of Nickel Decorated Nitrogen-Doped Carbon Catalysts for Electrochemical Reduction of CO_2 to CO. *Adv. Energy Mater.* **11,** 2101477 (2021).
33. Hossain, M. D., Huang, Y., Yu, T. H., Goddard, W. A., III & Luo, Z. Reaction Mechanism and Kinetics for CO_2 Reduction on Nickel Single Atom Catalysts from Quantum Mechanics. *Nat. Commun.* **11**, 2256 (2020).
34. Diercks, C. S., Lin, S., Kornienko, N., Kapustin, E. A., Nichols, E. M., Zhu, C. & Yaghi, O. M. Reticular Electronic Tuning of Porphyrin Active Sites in Covalent Organic Frameworks for Electrocatalytic Carbon Dioxide Reduction. *J. Am. Chem.*

Soc. **140**, 1116–1122 (2018).

35. Zhu, H. J., Lu, M., Wang, Y. R., Yao, S. J., Zhang, M., Kan, Y. H. & Lan, Y. Q. Efficient Electron Transmission in Covalent Organic Framework Nanosheets for Highly Active Electrocatalytic Carbon Dioxide Reduction. *Nat. Commun.* **11,** 497 (2020).
36. Wang, L., Chen, W., Zhang, D., Du, Y., Amal, R., Qiao, S. & Yin, Z. Surface Strategies for Catalytic CO_2 Reduction: from Two-Dimensional Materials to Nanoclusters to Single Atoms. *Chem. Soc. Rev.* **48**, 5310–5349 (2019).
37. Charles, J. & Muthusamy, S. Comparative Study of Butyl Rubber (IIR) and Bromobutyl Rubber (BIIR) based on FTIR, Dielectric and Thermal Studies. *J. Appl. Sci. Eng. Methodol.* **2**, 206–211 (2016).
38. Kulkarni, R., Huang, J., Trunk, M., Burmeister, D., Amsalem, P., Müller, J. & Bojdys, M. J. Direct Growth of Crystalline Triazine-Based Graphdiyne using Surface-Assisted Deprotection-Polymerisation. *Chem. Sci.* **12**, 12661–12666 (2021).
39. Huang, C., Li, A., Li, L. & Chen, Z. Synthesis of Quinolines from Aniline and Propanol over Modified USY Zeolite: Catalytic Performance and Mechanism Evaluated by In Situ Fourier Transform Infrared Spectroscopy. *RSC. Adv.* **7**, 24950–24962 (2017).
40. Sato, Y., Itoh, K., Hagiwara, R., Fukunaga, T. & Ito, Y. On the So-Called "Semi-ionic" C–F Bond Character in Fluorine–GIC. *Carbon* **42**, 3243–3249 (2004).

41. Brar, A. S. & Kapur, G. S. Sequence Determination in Methyl Methacrylate-n-Butyl Methacrylate Copolymers by ^{13}C NMR Spectroscopy *Polym. J.* **20**, 811–817 (1988)).

42. Britton, D., Heatley, F. & Lovell, P. A. ^{13}C NMR Spectroscopy Studies of Branching and Sequence Distributionin Copolymers of Vinyl Acetate andn-Butyl Acrylate Prepared by Semibatch Emulsion Copolymerization. *Macromol.* **34**, 817–882 (2001).

43. Borovik, A. S., Bott, S. G. & Barron, A. R. Arene-Mercury Complexes Stabilized Aluminum and Gallium Chloride: Synthesis and Structural Characterization. *J. Am. Chem. Soc.* **123**, 11219–11228 (2001).

44. Wang, L., Wan, Y., Ding, Y., Wu, S., Zhang, Y., Zhang, X. & Xu, H. Conjugated Microporous Polymer Nanosheets for Overall Water Splitting Using Visible Light. *Adv. Mater.* **29,** 1702428 (2017).

45. Grosvenor, A. P., Biesinger, M. C., Smart, R. S. C. & McIntyre, N. S. New Interpretations of XPS Spectra of Nickel Metal and Oxides. *Surf. Sci.* **600**, 1771–1779 (2006).

46. Wang, F., Zuo, Z., Li, L., Li, K., He, F., Jiang, Z. & Li, Y. Large-Area Aminated-Graphdiyne Thin Films for Direct Methanol Fuel Cells. *Angew. Chem. Int. Ed.* **58**, 15010–15015 (2019).

47. Rupp, M., Auvray, T., Rousset, E., Mercier, G. M., Marvaud, V., Kurth, D. G. & Hanan, G. S. Photocatalytic Hydrogen Evolution Driven by a Heteroleptic

Ruthenium(II) Bis(terpyridine) Complex. *Inorg. Chem.* **58**, 9127–9134 (2019).

48. Yang, S., Hu, W., Zhang, X., He, P., Pattengale, B., Liu, C. & Huang, J. 2D Covalent Organic Frameworks as Intrinsic Photocatalysts for Visible Light-Driven CO_2 Reduction. *J. Am. Chem. Soc.* **140**, 14614–14618 (2018).

49. Han, B., Ou, X., Deng, Z., Song, Y., Tian, C., Deng, H., Xu, Y. & Lin, Z. Nickel Metal – Organic Framework Monolayers for Photoreduction of Diluted CO2: Metal - Node - Dependent Activity and Selectivity. Angew. Chem., Int. Ed. 57, 16811 (2018).

50. Zhu, W., Zhang, C., Li, Q., Xiong, L., Chen, R., Wan, X., Wang, Z., Chen, W., Deng, Z. & Peng, Y. Selective Reduction of CO_2 by Conductive MOF Nanosheets as an Efficient Co-Catalyst under Visible Light Illumination. *Appl. Catal. B: Environ.* **238**, 339 (2018).

51. Niu, K., Xu, Y., Wang, H., Ye, R., Xin, F., Lin, H., Tian, C., Lum, Y., Bustillo, K. C., Doeff, M. M., Koper, M. T. M., Ager, J., Xu, R. & Zheng, H. A Spongy Nickel-Organic CO_2 Reduction Photocatalyst for nearly 100% Selective CO Production. *Sci Adv*, **3**, 1700921 (2017).

52. Zhong, W., Sa, R., Li, L., He, Y., Li, L., Bi, J., Zhuang, Z., Yu. Y. & Zou, Z. A Covalent Organic Framework Bearing Single Ni Sites as a Synergistic Photocatalyst for Selective Photoreduction of CO_2 to CO. *J. Am. Chem. Soc.* **141**, 7615–7621 (2019).

53. Zhong, W., Sa, R., Li, L., He, Y., Li, L., Bi, J., Zhuang, Z., Yu. Y. & Zou, Z. A

Covalent Organic Framework Bearing Single Ni Sites as a Synergistic Photocatalyst for Selective Photoreduction of CO_2 to CO. *J. Am. Chem. Soc.* **141**, 7615–7621 (2019).

54. Choi, K. M., Kim, D., Rungtaweevoranit, B., Trickett, C. A., Barmanbek, J. T., Alshammari, A. S., Yang, P. & Yaghi, O. M. Plasmon-Enhanced Photocatalytic CO_2 Conversion within Metal–Organic Frameworks under Visible Light *J. Am. Chem. Soc.* **139**, 356 (2017).

55. Huang, R., Peng, Y., Wang, C., Shi, Z. & Lin, W. A Rhenium-Functionalized Metal–Organic Framework as a Single-Site Catalyst for Photochemical Reduction of Carbon Dioxide. *Eur. J. Inorg. Chem.* 2016, 4358–4362 (2016).

56. Yang, S., Hu, W., Zhang, X., He, P., Pattengale, B., Liu, C., Cendejas, M., Hermans, I., Zhang, X., Zhang, J. & Huang, J. 2D Covalent Organic Frameworks as Intrinsic Photocatalysts for Visible Light-Driven CO_2 Reduction. *J. Am. Chem. Soc.* **140**, 14614 (2018).

57. Wang, Y., Huang, N., Shen, J., Liao, P., Chen, X. & Zhang, J. Hydroxide Ligands Cooperate with Catalytic Centers in Metal–Organic Frameworks for Efficient Photocatalytic CO_2 Reduction. *J. Am. Chem. Soc.* **140**, 38–41 (2018).

58. Gao, C., Chen, S., Wang, Y., Wang, J., Zheng, X., Zhu, J., Song, L., Zhang, W. & Xiong, Y. Heterogeneous Single-Atom Catalyst for Visible-Light-Driven High-Turnover CO_2 Reduction: The Role of Electron Transfer. *Adv. Mater.* **30**, 1704624 (2018).

59. Gao, C., Meng, Q., Zhao, K., Yin, H., Wang, D., Guo, J., Zhao, S., Chang, L., He, M., Li, S., Zhao, H., Huang, X., Gao, Y. & Tang, Z. Co_3O_4 Hexagonal Platelets with Controllable Facets Enabling Highly Efficient Visible-Light Photocatalytic Reduction of CO_2. *Adv. Mater.* **28**, 6485 (2016).

60. Kajiwara, T., Fujii, M., Tsujimoto, M., Kobayashi, K., Higuchi, M., Tanaka, K. & Kitagawa, S. Photochemical Reduction of Low Concentrations of CO_2 in a Porous Coordination Polymer with a Ruthenium(II)–CO Complex. *Angew. Chem., Int. Ed.* 55, 2697 (2016).

61. Mulliken, R. S. Electronic Population Analysis on LCAO–MO Molecular Wave Functions. I. *J. Chem. Phys.* **23**, 1833–1840 (1955).

Chapter 5

Experimental Details

5.1 General information

All reagents and solvents were received from commercial suppliers and used without further purification unless otherwise noted. Mercury dichloride ($HgCl_2$, ≥ 98.0%, Energy), triethylamine (Et_3N, 99.5%, TCI), methanol, anhydrous dichloromethane (DCM), trimethylsilylacetylene (≥ 98.0%, TCI), 2,4,6-tris(4-bromophenyl)-1,3,5-triazine (≥ 97.0%, TCI), 1,3,5-trifluoro-2,4,6-triiodobenzene (≥ 97.0%, TCI), 1,3,5-tris(4-bromophenyl)benzene (≥ 98.0%, TCI), 2,4,6-tribromoaniline (≥ 98.0%, TCI), bis(triphenylphosphine)palladium(II) chloride ($PdCl_2(PPh_3)_2$, 98.0%, J&K), potassium carbonate (K_2CO_3, J&K), and copper iodide (CuI, 98.0%, J&K). Diatom powder and silica gel for column chromatography were used from Sigma-Aldrich (pore size 60 Å, 70–230 mesh, and 63–200 μm). Nafion (5% w/w) was used from Sigma-Aldrich.

All reactions were carried out under nitrogen unless otherwise stated. Commercially available reagents were used without further purification. All reactions were monitored by thin-layer chromatography (TLC) with Merck pre-coated aluminum plates. Compounds were visualized with UV light irradiation at 254 and 365 nm. Separation or purification of products was achieved by column chromatography using silica gel from Huanghai (200–300 mesh). The chemical structures of organic ligands

were characterized by ^{1}H and ^{13}C NMR spectra using a 400 MHz spectrometer (Bruker ascend 400 MHz NMR spectrometer). Solid-state ^{13}C NMR spectra were recorded on a Bruker Avance III 600 MHz NMR spectrometer. Chemical shifts of NMR spectra were reported in parts per million (ppm) relatives to tetramethylsilane ($\delta = 0$). The following abbreviations were used to describe peak splitting patterns when appropriate: s = singlet, d = doublet, t = triplet, q = quartet, m = multiplet, dd = doublet of doublet. The mass of organic compounds was measured on a Bruker UltrafleXtreme MALDI-TOF mass spectrometer. Fourier transform infrared (FT-IR) spectra were recorded on a Thermo-Nicolet 6700 spectrometer in the 4000–500 cm^{-1} range. The morphology of the samples was investigated via scanning electron microscopy (SEM) on an FEI SIRION200 microscope and transmission electron microscopy (TEM) with a JEM-ARM 2100F Atomic Resolution Analytical Microscope. The crystal structure of the as-prepared products was characterized by powder X-ray diffraction (PXRD) by using a Japan Rigaku DMax-γA rotation anode X-ray diffractometer equipped with graphite monochromatic Cu Kα radiation ($\lambda = 1.54178$ Å). Diffuse reflectance spectra (DRS) were collected at room temperature with a UV–Vis spectrophotometer (Cary-300, Shimazu). A white standard of $BaSO_4$ was used as a reference. The valence band of the photocatalyst was obtained by ultraviolet photoelectron spectroscopy (UPS) with HeI (21.22 eV) as the monochromatic light source and a total instrumental energy resolution of 100 meV. X-ray photoelectron spectra (XPS) spectra were acquired by using a Thermo Fisher Nexsa spectrometer. The adventitious carbon C 1s peak (284.5 eV) was

used to calibrate all binding energy values.

5.2 Experimental Details

Synthesis of 1,3,5-tris{4-(trimethylsilyl)ethynyl]phenyl}benzene:

To the tris(4-bromophenyl)benzene in a round bottom flask, CuI, $Pd(PhCN)_2Cl_2$, and $[(t\text{-}Bu)_3PH]BF_4$ were added. The mixture was treated with a vacuum-nitrogen cycle three times. Then, dioxane was added to the mixture and stirred to dissolve the mixture, giving a brick-red suspension. To this suspension, diisopropylamine (DIPA) was injected. Then, trimethylsilylacetylene was dropwise injected to this solution and the mixture was stirred for one night, giving a black solution. After the reaction ended, the solution was filtered with diatomite. The obtained solution was purified through flash column chromatography. After evaporating the solvents and dried by a reduced pressure, 1,3,5-tris{4-(trimethylsilyl)ethynyl]phenyl}benzene was obtained as yellow crystals in 73% yield. ^{1}H NMR (400 MHz, Chloroform-*d*): δ ppm 7.74 (s, 3H), 7.62 (dd, J = 8.0 Hz, 6H), 7.56 (dd, 6H), 0.26 (s, 27H). ^{13}C NMR (100 MHz, Chloroform-*d*): δ ppm 141.6, 140.7, 132.5, 127.0, 125.1, 122.5, 104.8, 95.2, 0.2. MALDI-TOF: m/z calculated 594.2594, found 579.232 $[M-CH_3]^+$.

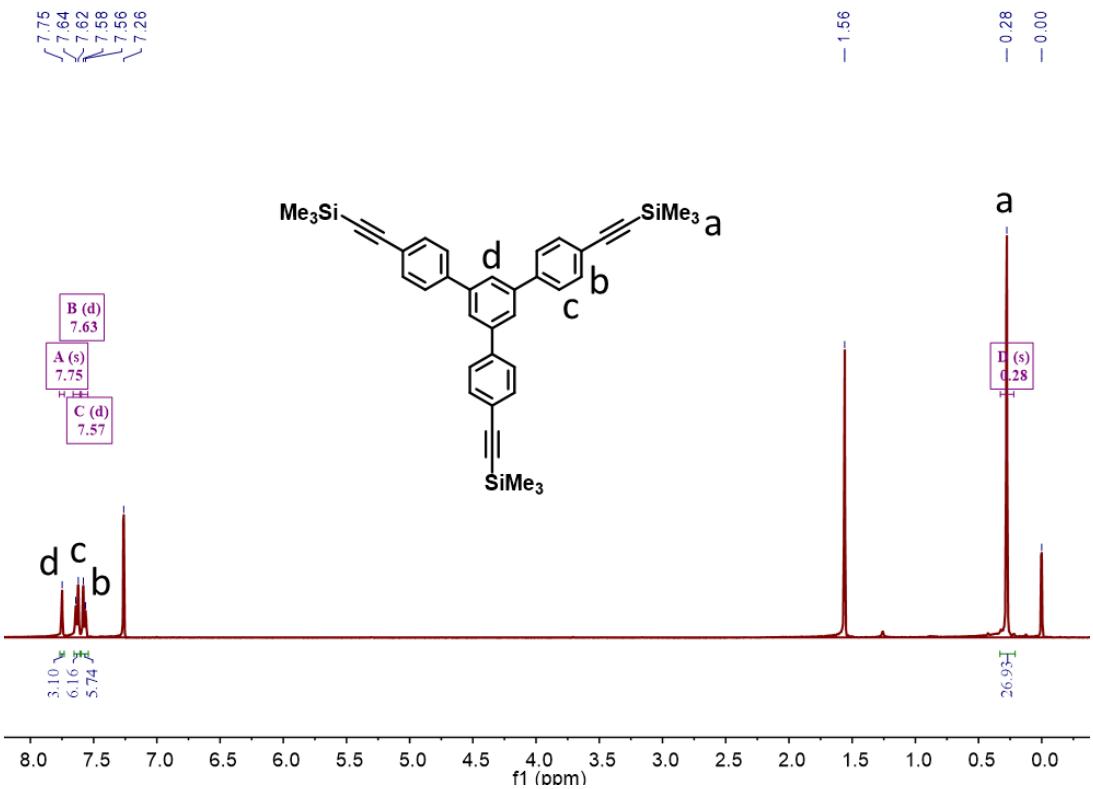

Figure 1 [1]H-NMR spectrum of 1,3,5-tris{4-(trimethylsilyl)ethynyl]phenyl}benzene.

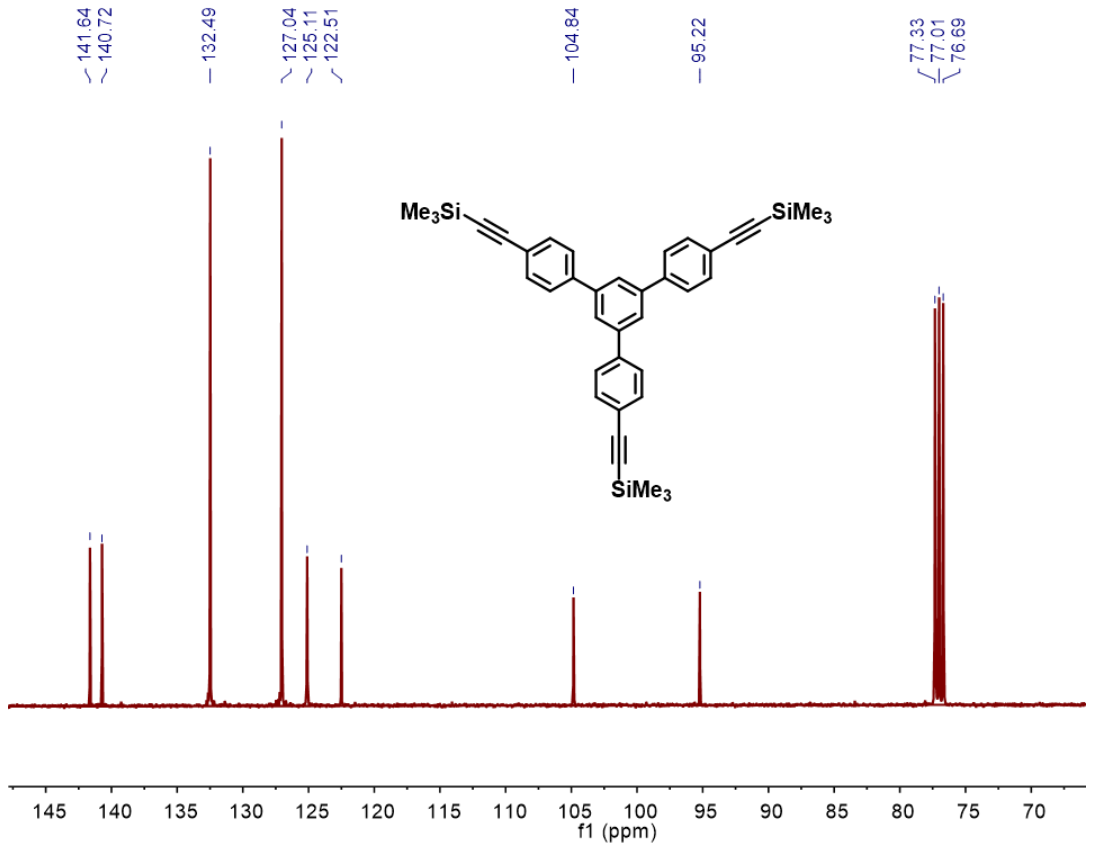

Figure 2 [13]C-NMR spectrum of 1,3,5-tris{4-(trimethylsilyl)ethynyl]phenyl}benzene.

Synthesis of 1,3,5-triethynyltriphenylbenzene:

To the 1,3,5-tris{4-(trimethylsilyl)ethynyl]phenyl}benzene in a round bottom flask, DCM and methanol were added. Then, K_2CO_3 was added to the solution and the mixture was stirred at RT for 16 h. After the reaction ended, the solution was filtered, and the obtained product was purified through flash column chromatography. After evaporating the solvent and dried by a reduced pressure, 1,3,5-triethynyltriphenylbenzene was obtained as white crystals in 90% yield. ^{1}H NMR (400 MHz, Chloroform-*d*) δ ppm 7.76 (s, 3H), 7.65 (dd, *J* = 8.4 Hz, *J* = 8.3 Hz, 6H), 7.61 (dd, *J* = 8.4 Hz 6H), 3.16 (s, 1H). ^{13}C NMR (100 MHz, Chloroform-*d*): δ ppm 141.9, 141.3, 132.9, 127.4, 125.5, 121.7, 83.6, 78.3. MALDI-TOF: m/z calculated 378.1247, found 376.299 $[M-2H]^{+}$.

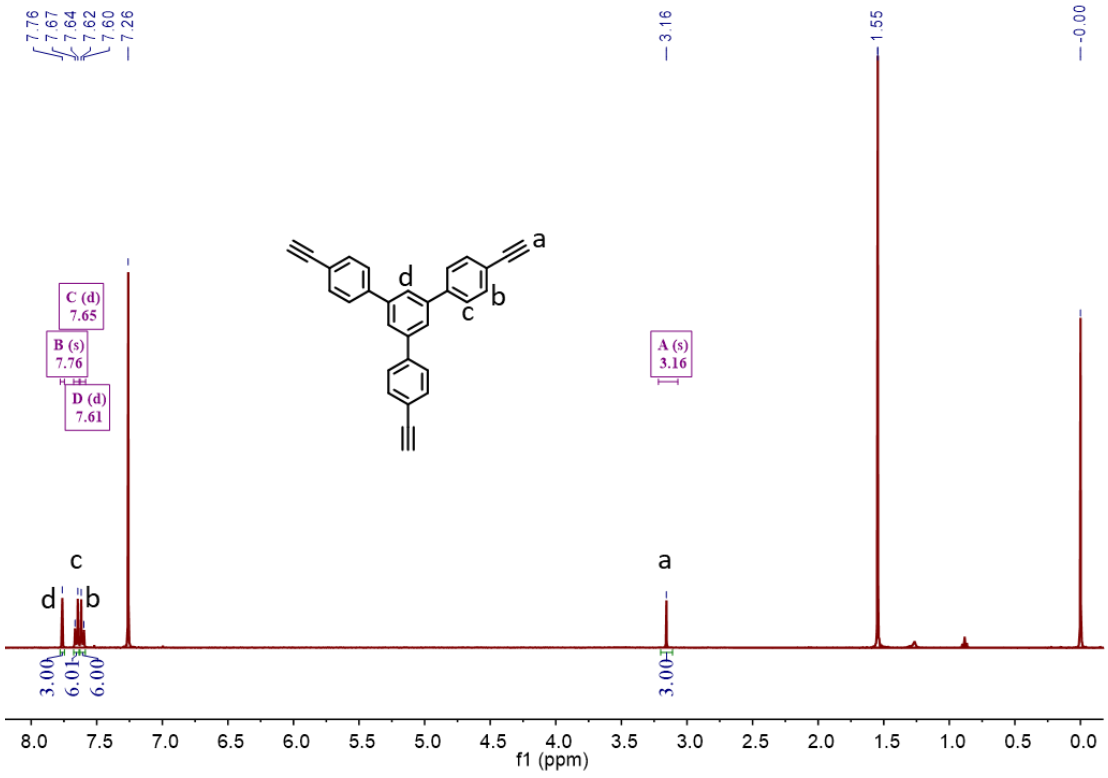

Figure 3 ^{1}H-NMR spectrum of 1,3,5-triethynyltriphenylbenzene.

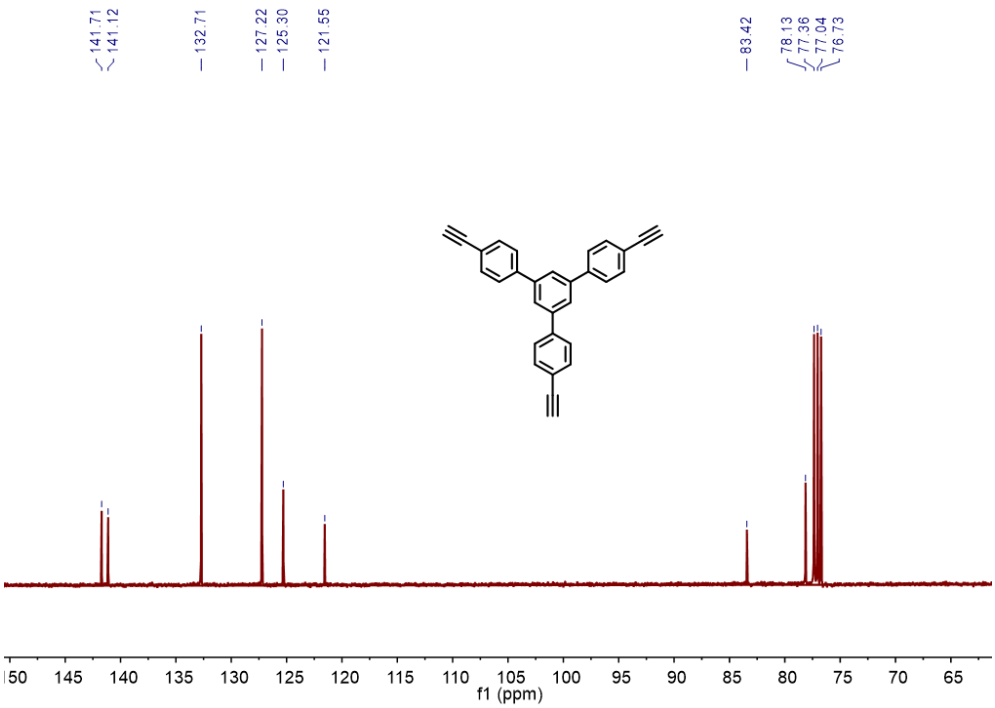

Figure 4 ^{13}C-NMR spectrum of 1,3,5-triethynyltriphenylbenzene.

Synthesis of 2,4,6-tris[4-[2-(trimethylsilyl)ethynyl]phenyl]-1,3,5-triazine:

To the 2,4,6-tris(4-bromophenyl)-1,3,5-triazine in a round bottom flask, CuI, Pd $(PhCN)_2Cl_2$, and $[(t\text{-}Bu)_3PH]BF_4$ were added. The mixture was treated by vacuum-nitrogen cycle three times. Then, dioxane was added to the mixture and stirred to dissolve the mixture, giving a brick-red suspension. DIPA was injected to this suspension and then trimethylsilylacetylene was dropwise injected to this solution. The mixture was stirred for 48 h at 85°C, giving a black solution. After the reaction ended, the solution was filtered with diatomite. The obtained product was purified through flash column chromatography. After evaporating the solvent and dried by a reduced pressure, 2,4,6-tris[4-[2-(trimethylsilyl)ethynyl]phenyl]-1,3,5-triazine was obtained as a yellow crystalline solid. ^{1}H NMR (400 MHz, Chloroform-*d*): δ ppm 8.70 (d, J = 8.4 Hz, 6H), 7.65 (d, J = 8.4 Hz, 6H), 0.30 (s, 27H). MALDI-TOF: m/z calculated 598.2525,

found 599.325 $[M+H]^+$.

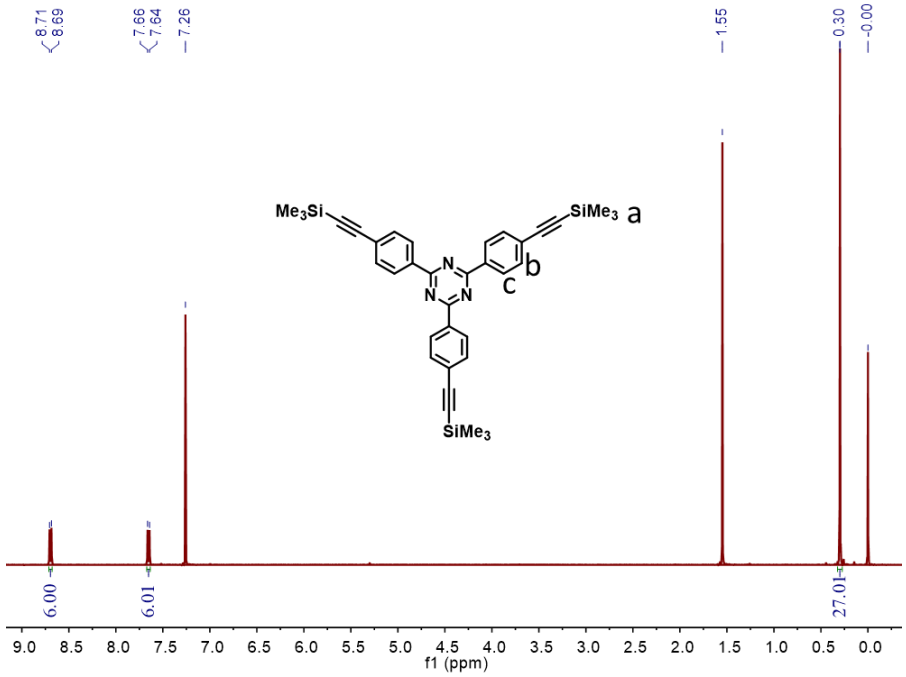

Figure 5 ^{1}H-NMR spectrum of 2,4,6-tris[4-[2-(trimethylsilyl)ethynyl]phenyl]-1,3,5-triazine.

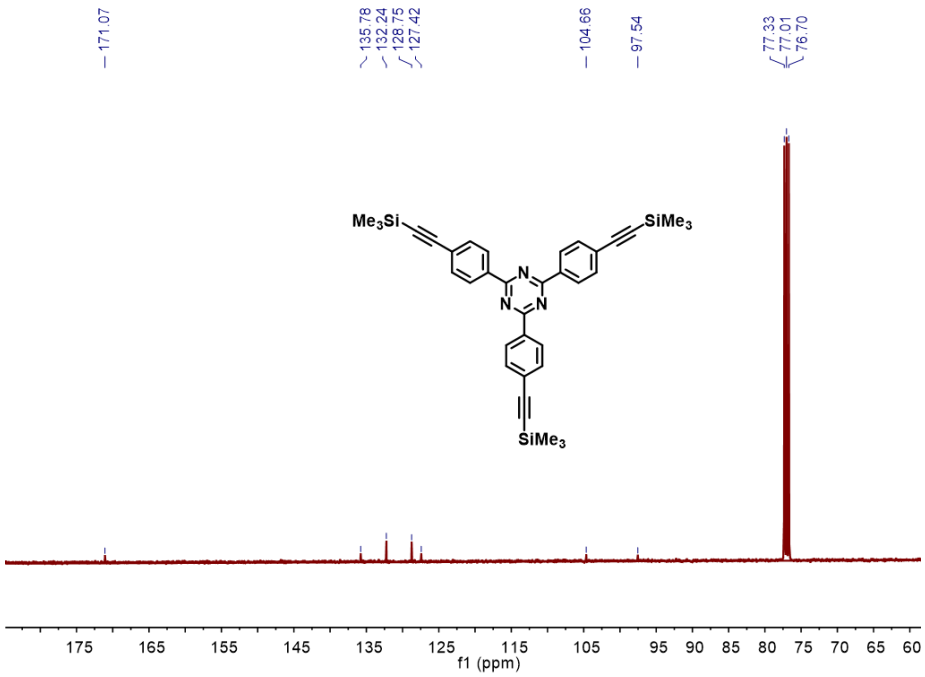

Figure 6 ^{13}C-NMR spectrum of 2,4,6-tris[4-[2-(trimethylsilyl)ethynyl]phenyl]-1,3,5-triazine.

Synthesis of 2,4,6-tris(4-ethynylphenyl)-1,3,5-triazine:

To the 2,4,6-tris[4-[2-(trimethylsilyl)ethynyl]phenyl]-1,3,5-triazine in a round bottom flask, DCM and methanol were added. Then, K_2CO_3 was added to the solution and the mixture was stirred at RT for 16 h. After the reaction ended, the solution was filtered, and the obtained product was purified through flash column chromatography. After evaporating the solvent and dried by a reduced pressure, 2,4,6-tris(4-ethynylphenyl)-1,3,5-triazine was obtained as brown crystals in 85% yield. ^{1}H NMR (400 MHz, Chloroform-*d*): δ ppm 8.73 (d, *J* = 8.4 Hz, 6H), 7.70 (d, *J* = 8.4 Hz, 6H), 3.28 (s, 3H). ^{13}C NMR (100 MHz, Chloroform-*d*): δ ppm 171.1, 136.1, 132.4, 128.8, 126.4, 83.3, 80.0. MALDI-TOF: m/z calculated 381.1339, found 382.1850 $[M+H]^+$.

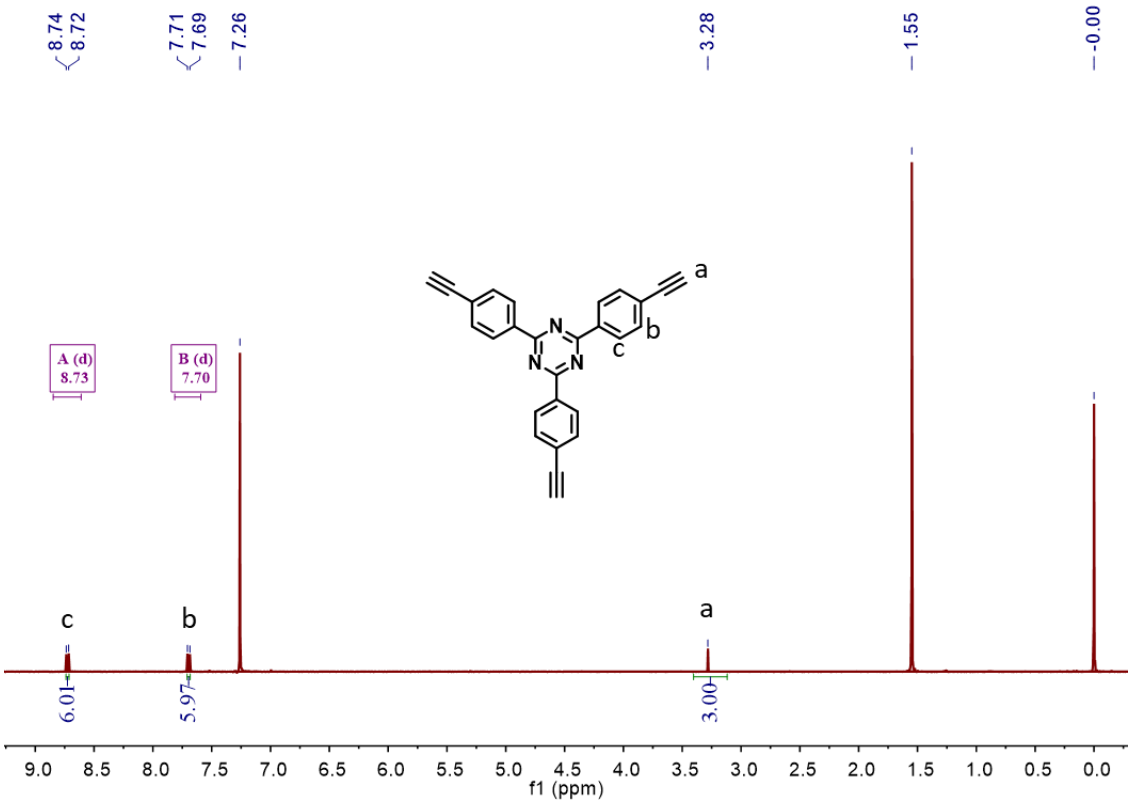

Figure 7 ^{1}H-NMR spectrum of 2,4,6-tris(4-ethynylphenyl)-1,3,5-triazine.

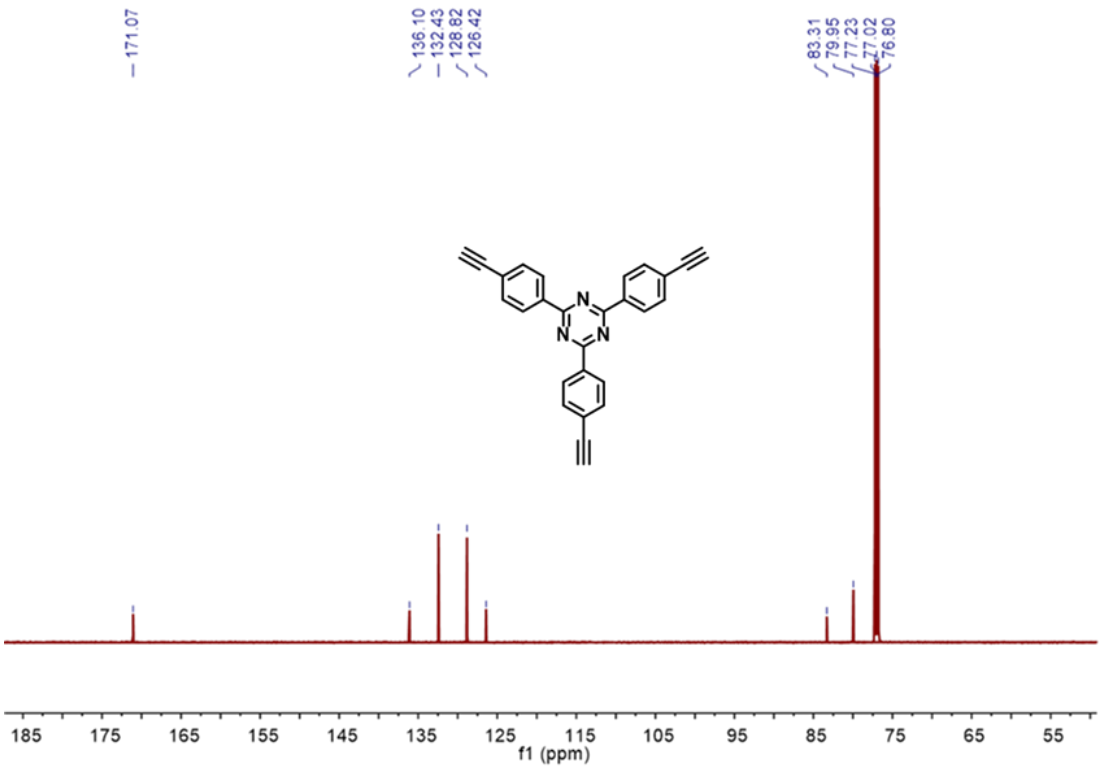

Figure 8 ^{13}C-NMR spectrum of 2,4,6-tris(4-ethynylphenyl)-1,3,5-triazine.

Synthesis of 2,4,6-tris[2-(trimethylsilyl)ethynyl]aniline:

2,4,6-Tribromoaniline (1.32 g, 4 mmol) was mixed with CuI (84.2 g, 0.12 mmol) and $PdCl_2(PPh_3)_2$ (22.9 g, 0.12 mmol) in a round bottom flask. The mixture was vacuum-degassed and purged with pure nitrogen three times. Then, 20 mL of Et_3N was added to the mixture, and it was stirred upon complete dissolution, giving a brick-red suspension. Then, 12 mmol (1.18 g,) of trimethylsilylacetylene were dropwise injected into this solution and stirred at 85 °C for 48 h, giving a black solution. After the reaction ended, the solution was filtered with diatom powder to remove the catalyst of $PdCl_2(PPh_3)_2$. The obtained solution was purified through a flash column chromatography (hexane/CH_2Cl_2 = 15:1). After evaporating the solvent and drying by reduced pressure, 2,4,6-tris[2-(trimethylsilyl)ethynyl]aniline (1.25 g, yield 50%) was

obtained as a yellow oil. ^{1}H NMR (400 MHz, Chloroform-d): δ ppm 7.38 (s, 2H), 4.97 (s, 2H), 0.25 (s, 18H), 0.20 (s, 9H). ^{13}C NMR (400 MHz, Chloroform-d): δ ppm 149.61, 136.18, 111.53, 107.31, 104.29, 100.74, 100.19, 91.87, 29.73. MALDI-TOF: m/z calculated 381.1759, found 381.2280 $[M]^{+}$.

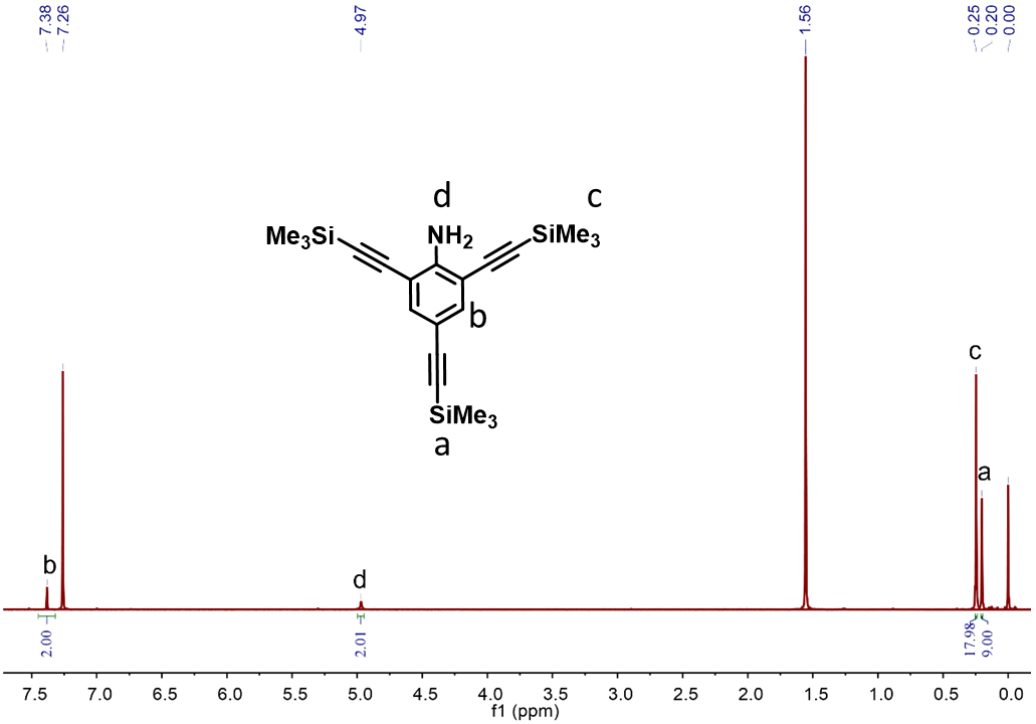

Figure 9 ^{1}H-NMR spectrum of 2,4,6-tris[2-(trimethylsilyl)ethynyl]aniline.

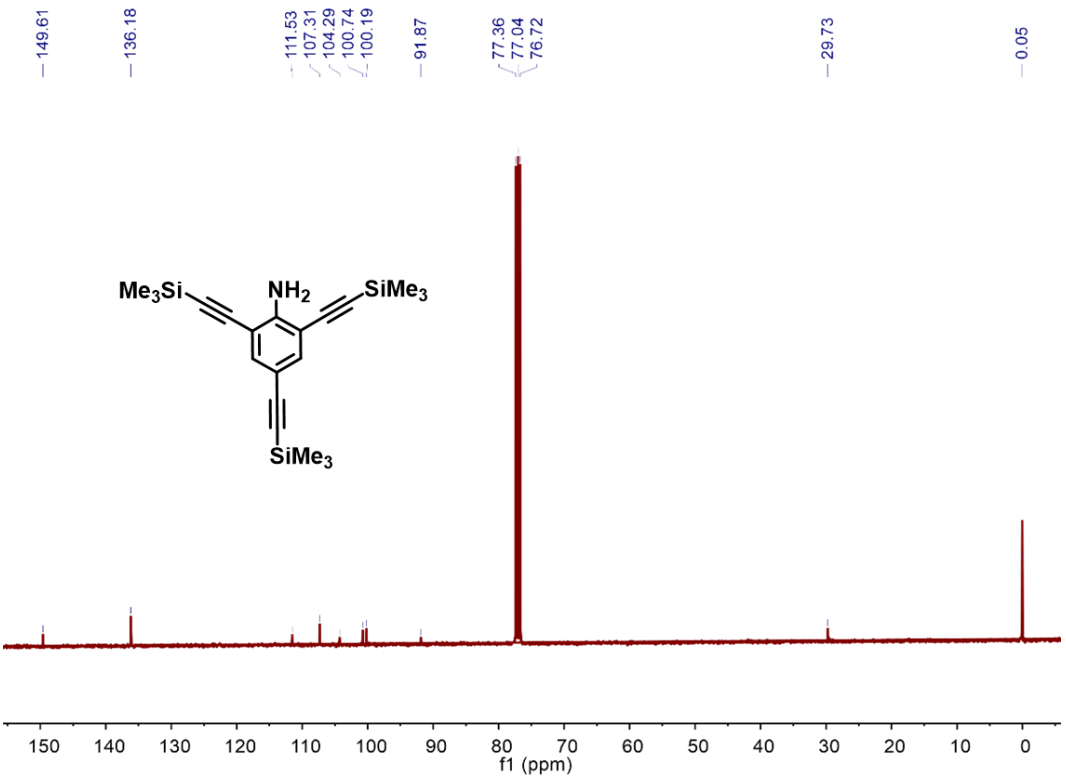

Figure 10 ^{13}C-NMR spectrum of 2,4,6-tris[2-(trimethylsilyl)ethynyl]aniline.

Synthesis of 2,4,6-tiethynylaniline:

2,4,6-Tris[2-(trimethylsilyl)ethynyl]aniline (0.76 g, 2 mmol) was added and dissolved in DCM (20 mL) and methanol (10 mL) in a round bottom flask. Then, 5.79 mmol (0.8 g) of K_2CO_3 was added to the solution and stirred at RT for 6 h. After the reaction ended, the product was filtered and purified through a flash column chromatography (hexane/CH_2Cl_2 = 3:1). After evaporating the solvents and drying at a reduced pressure, 2,4,6-triethynylaniline (0.33 g, yield 90%) was obtained as white crystals. ^{1}H NMR (400 MHz, Chloroform-d): δ ppm 7.46 (s, 2H), 5.03 (s, 2H), 3.40 (s, 2H), 2.93 (s, 1H). ^{13}C NMR (400 MHz, Chloroform-d): δ ppm 150.28, 136.92, 110.45, 106.31, 83.41, 82.48, 78.95, 75.46. MALDI-TOF: m/z calculated 165.1078, found 495.274 $[3M]^+$.

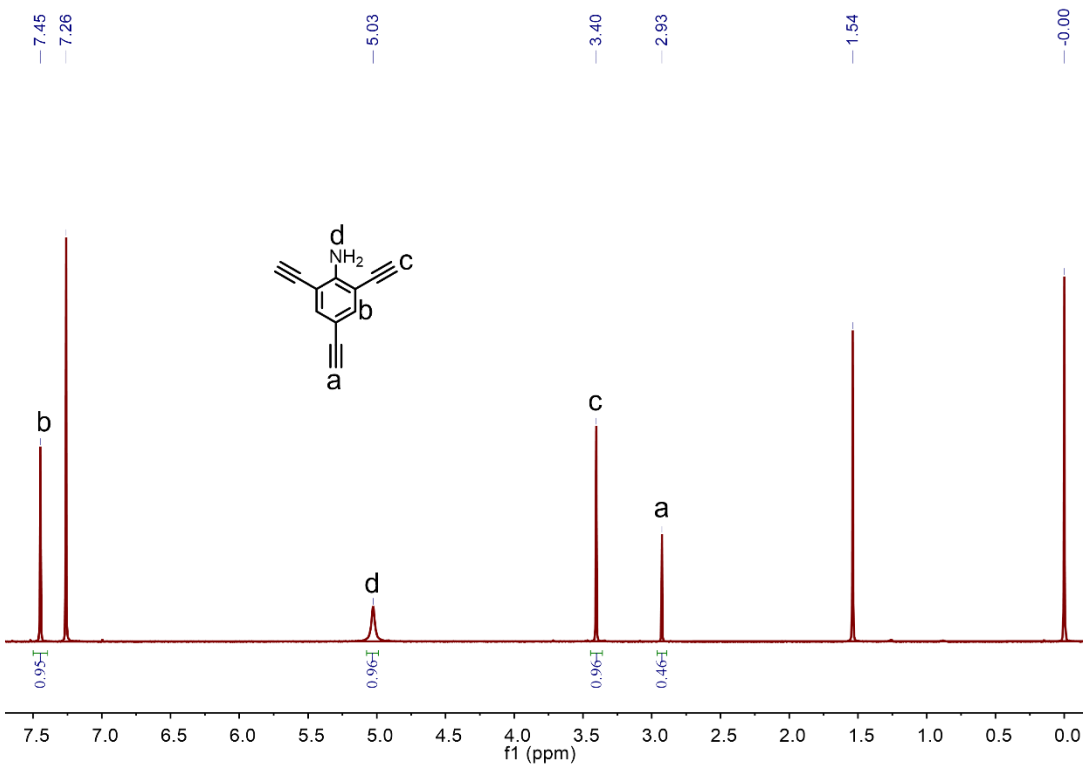

Figure 11 [1]H-NMR spectrum of 2,4,6-triethynylaniline.

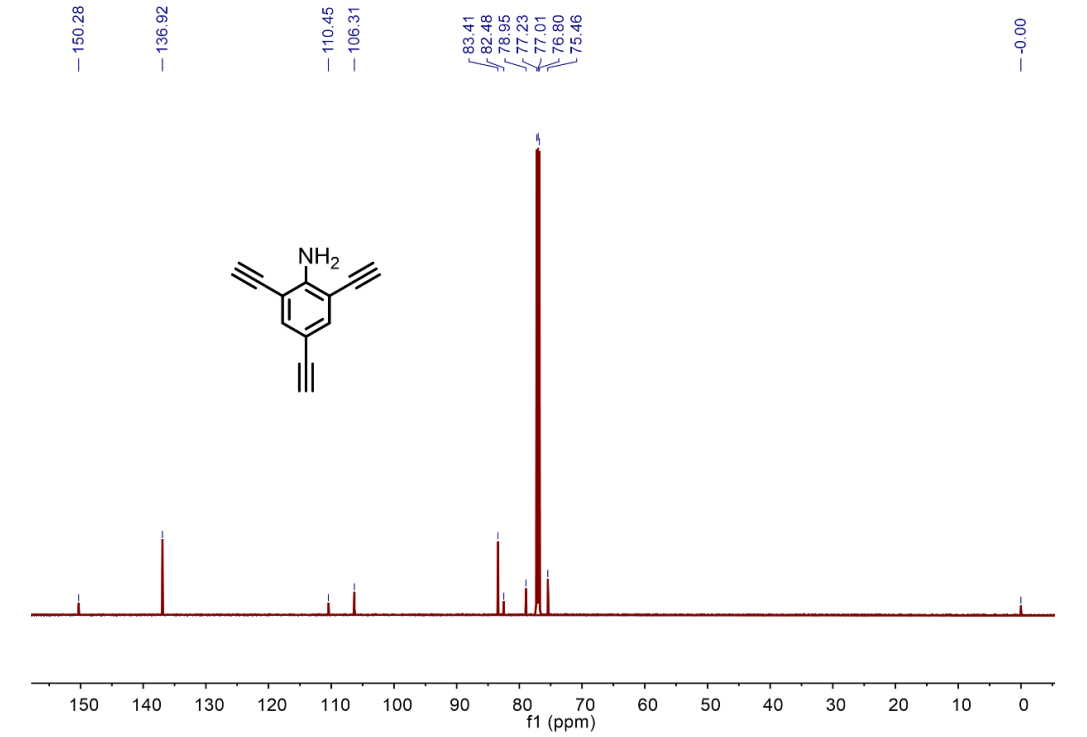

Figure 12 [13]C-NMR spectrum of 2,4,6-triethynylaniline.

Synthesis of 1,3,5-(trimethylsilyl)ethynyl-2,4,6-trifluorobenzene:

DIPA, 1,3,5-trifluoro-2,4,6-triiodobenzene, [$PdCl_2(PPh_3)_2$], and CuI were added to a dry three-necked flask. A solution of ethynyltrimethylsilane in DIPA was added dropwise, followed by PPh_3. At the end of the addition, the mixture was heated to 80 °C. After 1 h, THF was added, and the mixture was stirred for 35 h under nitrogen protection. The mixture was filtered through Celite, diluted with water, and extracted with chloroform. The extract was washed with brine and dried with anhydrous Na_2SO_4. After the evaporation of the solvents, the residue was purified by Biotageflash silica gel chromatography (eluted with hexane) to give 1,3,5-(trimethylsilyl)ethynyl-2,4,6-trifluorobenzene as a white powder in 80% yield. ^{1}H NMR (400 MHz, Chloroform-*d*): δ ppm 0.26 (s, 27H). ^{13}C NMR (400 MHz, Chloroform-d): δ ppm 164.66, 162.05, 107.15, 99.95, 88.96. ^{19}F NMR (400 MHz, Chloroform-*d*): -105.55 ppm. MALDI-TOF: m/z calculated 420.1373, found 333.192 $[M\text{-}TMS\text{-}Me]^+$.

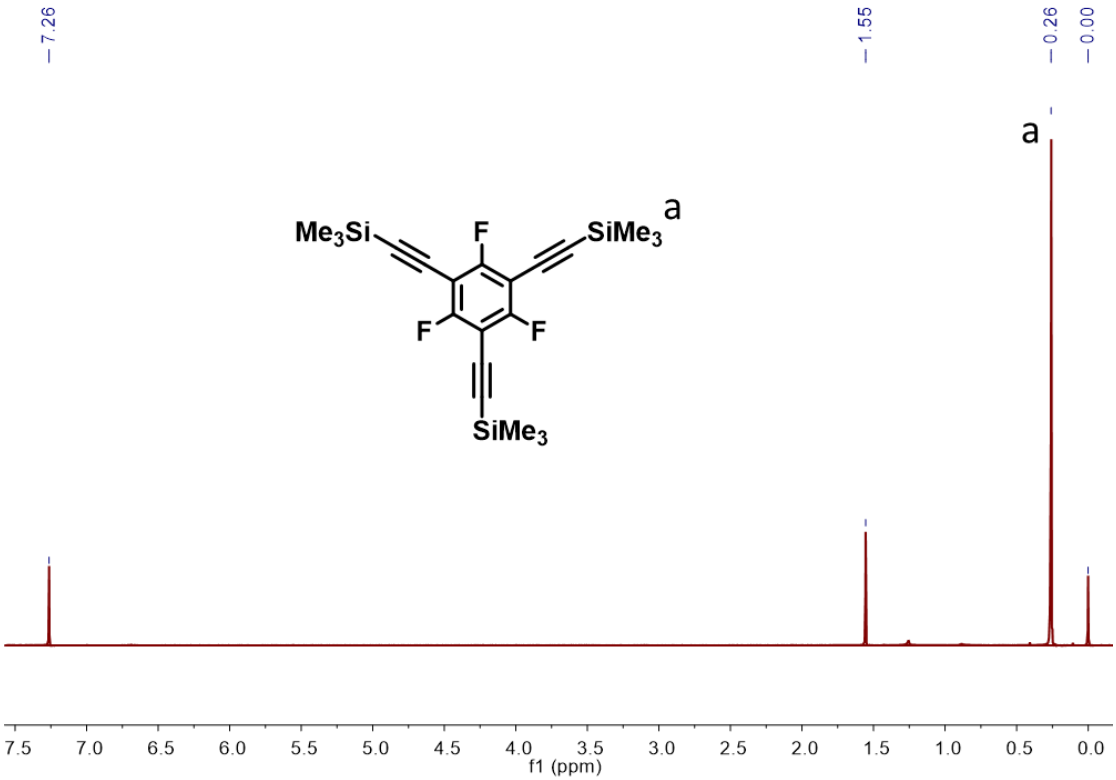

Figure 12 ^{1}H-NMR spectrum of 1,3,5-(trimethylsilyl)ethynyl-2,4,6-trifluorobenzene.

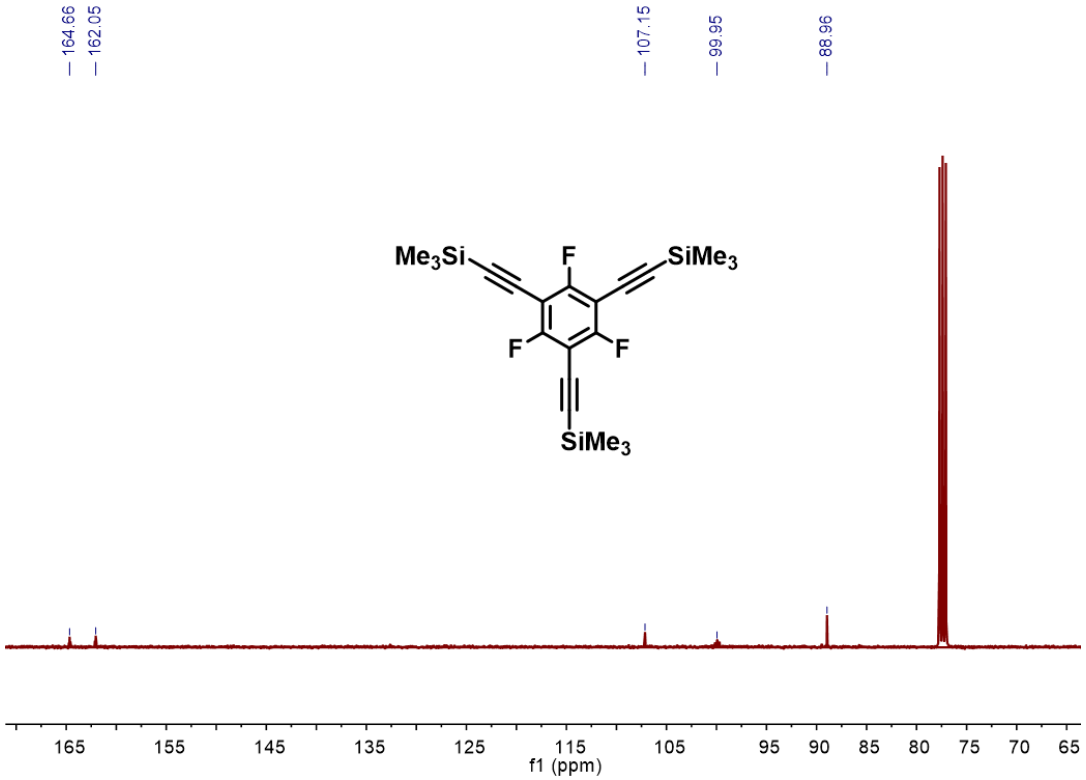

Figure 13 ^{13}C-NMR spectrum of 1,3,5-(trimethylsilyl)ethynyl-2,4,6-trifluorobenzene.

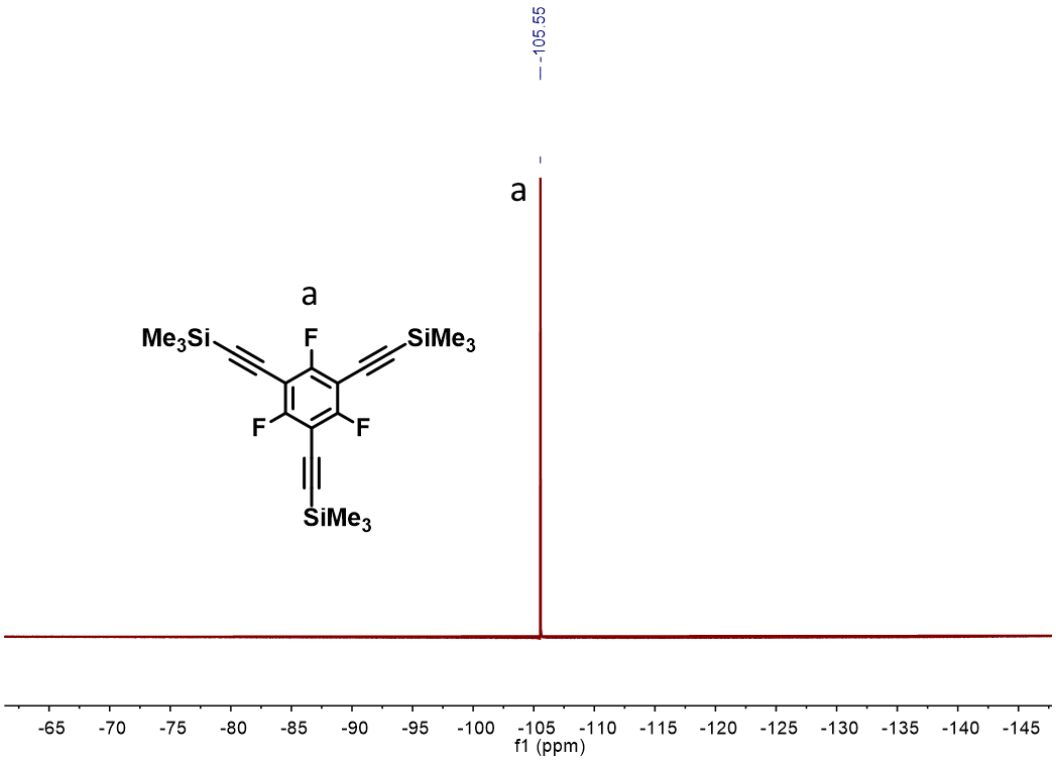

Figure 14 ^{19}F-NMR spectrum of 1,3,5-(trimethylsilyl)ethynyl-2,4,6-trifluorobenzene.

Synthesis of 1,3,5-triethynyl-2,4,6-trifluoro-benzene:

To the 1,3,5-(trimethylsilyl)ethynyl-2,4,6-trifluorobenzene in a round bottom flask, DCM and methanol were added. Then to the solution, K_2CO_3 was added and the mixture was stirred at RT for 16 h. After the reaction ended, the solution was filtered, and the obtained product was purified through flash column chromatography. After evaporating the solvent and dried by a reduced pressure, 1,3,5-triethynyl-2,4,6-trifluoro-benzene was obtained as a white powder in 95% yield. ^{1}H NMR (400 MHz, Chloroform-*d*): δ ppm, 3.49 (s, 3H). ^{13}C NMR (100 MHz, Chloroform-*d*): δ ppm 166.1, 163.4, 102.1, 87.6, 77.36, 71.38. ^{19}F NMR (400 MHz, Chloroform-*d*): -99.61 ppm. MALDI-TOF: m/z calculated 241.9740, found 242.303 $[M+H]^+$.

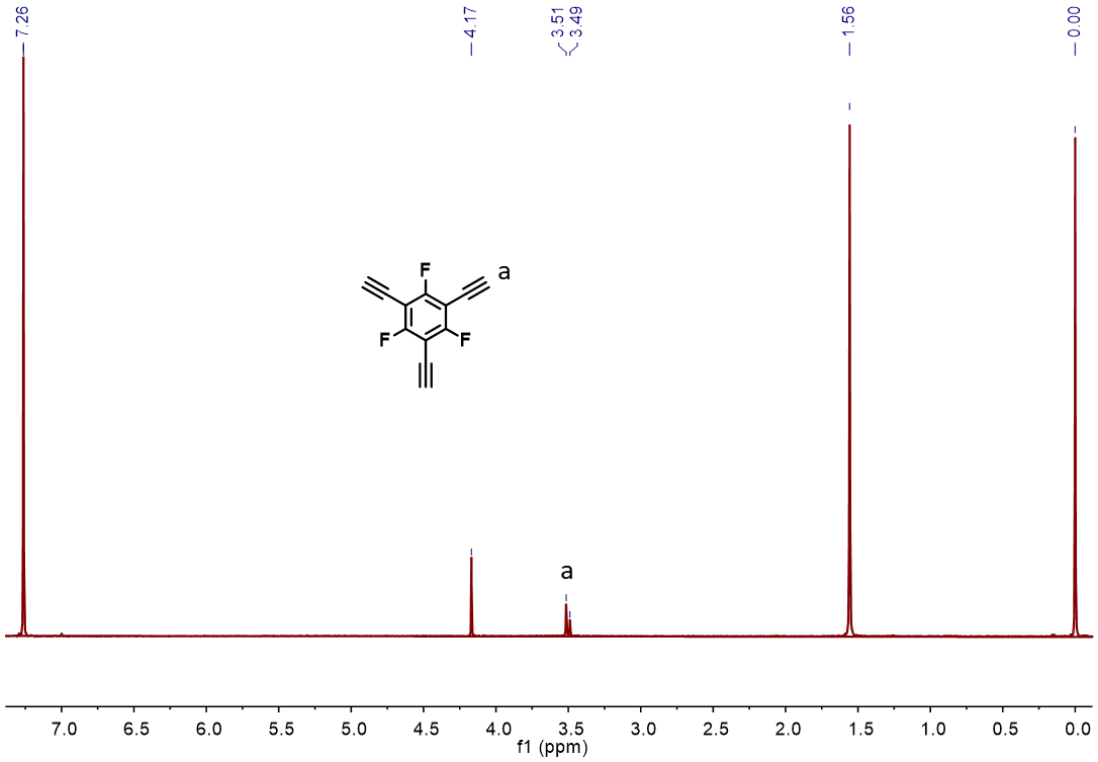

Figure 15 [1]H-NMR spectrum of 1,3,5-triethynyl-2,4,6-trifluoro-benzene.

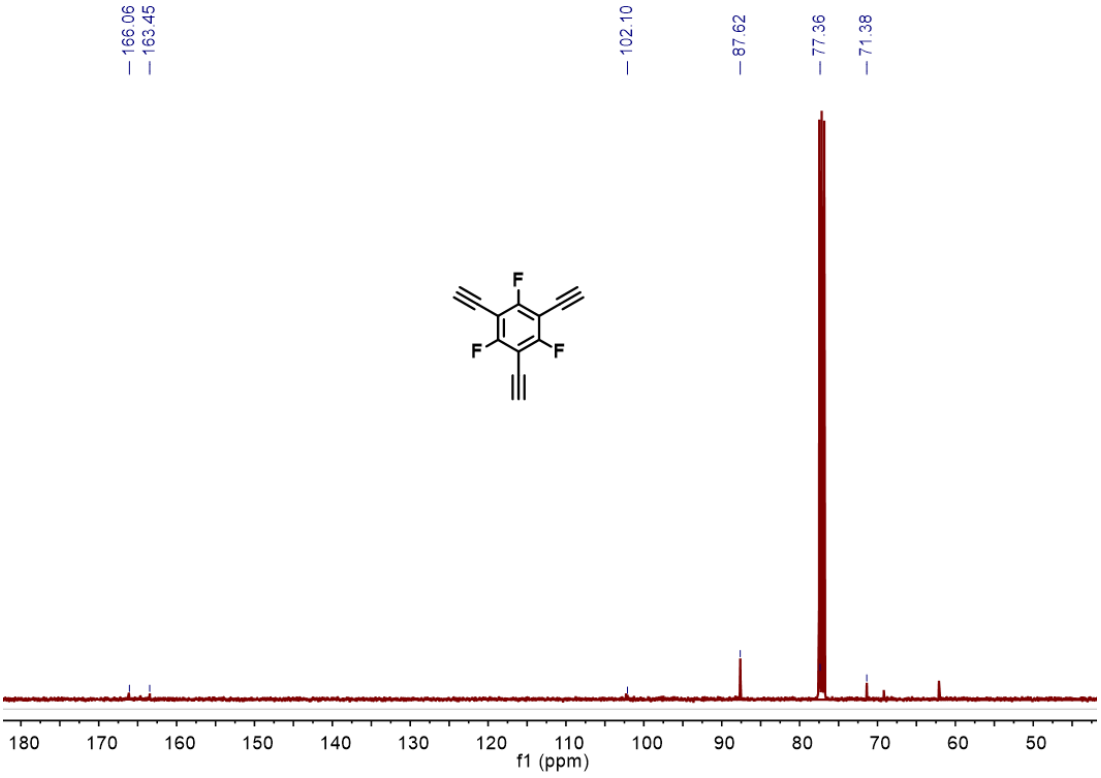

Figure 16 [13]C-NMR spectrum of 1,3,5-triethynyl-2,4,6-trifluoro-benzene.

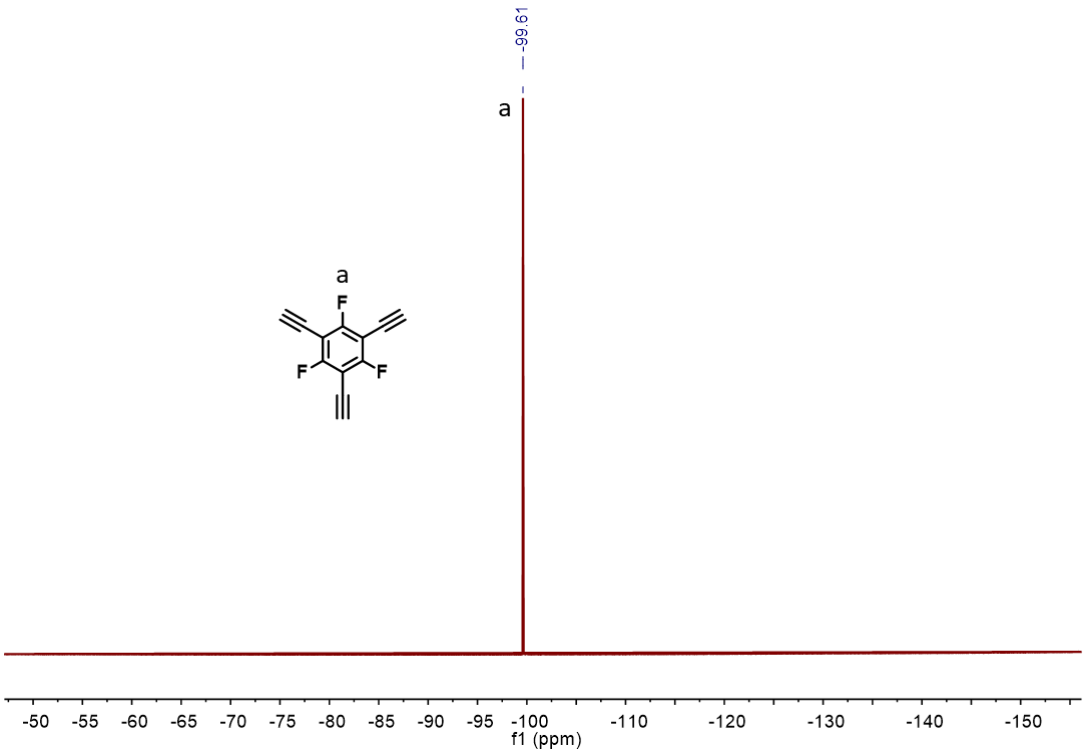

Figure 17 ^{19}F-NMR spectrum of 1,3,5-triethynyl-2,4,6-trifluoro-benzene.

Synthesis of *trans*-Pt(PBu$_3$)$_2$Cl$_2$:

To the K_2PtCl_4 in a round bottom flask, DI water was added. Then, the mixture was stirred to completely dissolve K_2PtCl_4, giving an orange-red solution. This solution was dropwise injected with PBu_3, and it was stirred for 3 h, giving a white precipitate. After the reaction ended, the product was extracted with DCM. The organic layer was collected, and the solvent was evaporated, giving a pale-yellow oil. The oil was heated at 190 ℃ for 1 h. The obtained mixture was purified through flash column chromatography. After evaporating the solvent and drying by reduced pressure, *trans*-Pt(PBu$_3$)$_2$Cl$_2$ was obtained as a yellow powder. ^{1}H NMR (400 MHz, Chloroform-*d*): δ ppm 1.98–1.76 (m, 12H), 1.61–1.40 (m, 24H), 0.95 (t, J = 7.2 Hz, 18H). ^{32}P NMR (400 MHz, Chloroform-*d*): δ ppm 4.44 (s, 2P).

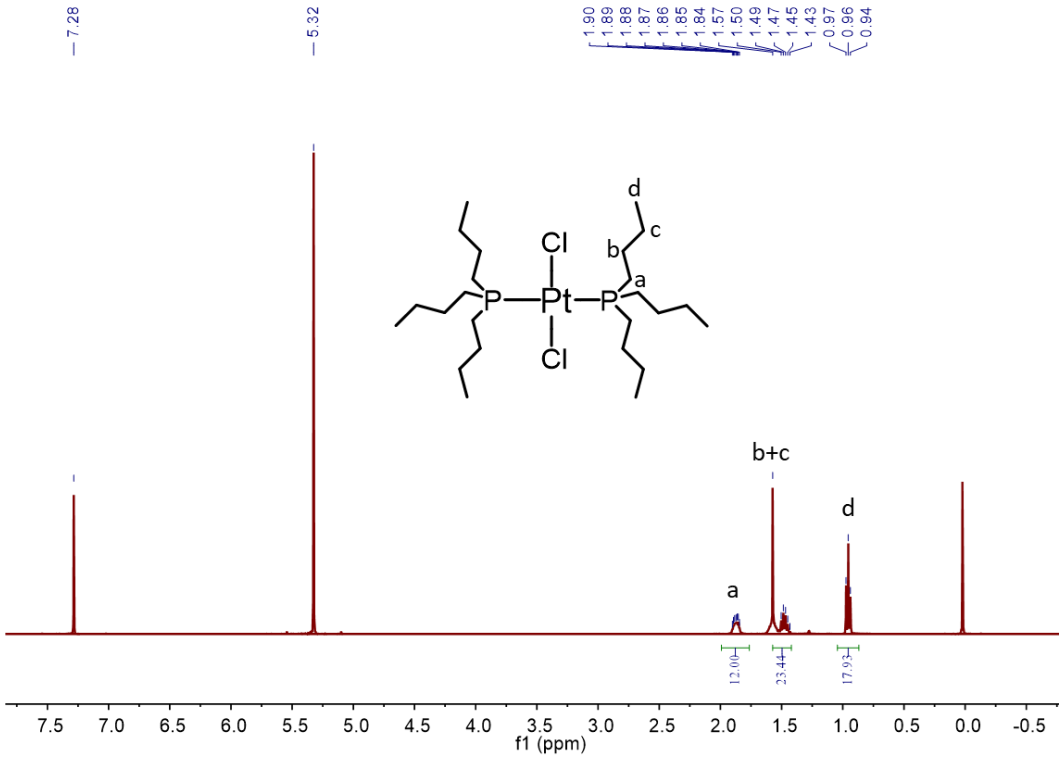

Figure 18 ^{1}H-NMR spectrum of *trans*-Pt(PBu$_3$)$_2$Cl$_2$.

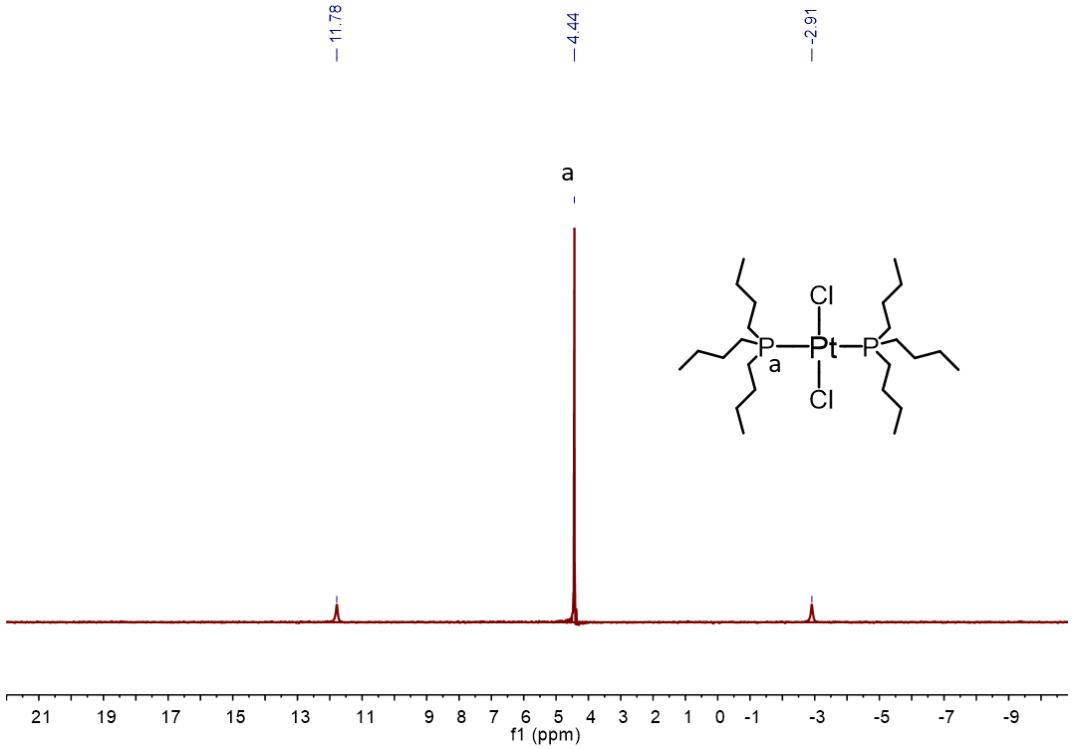

Figure 19 ^{32}P-NMR spectrum of *trans*-Pt(PBu$_3$)$_2$Cl$_2$.

Synthesis of *trans*-Ni(PBu$_3$)$_2$Cl$_2$:

To the NiCl$_2$•6H$_2$O in a round bottom flask, HPLC-grade EtOH was added. The mixture was stirred to completely dissolve NiCl$_2$•6H$_2$O, giving a green solution. Then, N$_2$ was bubbled into the mixed solution for 15 min. PBu$_3$ was mixed with HPLC-grade THF first, and then the mixed solution was added dropwise to the reaction system, giving a red suspension**.** Finally, the reaction was carried out at 80 °C for 1 h**.** After the reaction ended, the temperature of the reaction system was first lowered to RT. Then the reaction flask was placed in ice with NH$_4$Cl for 1 hour to allow the reactants to fully precipitate. Finally, the product of *trans*-Ni(PBu$_3$)$_2$Cl$_2$ was obtained as a red powder after suction filtration. ^{1}H NMR (400 MHz, Chloroform-*d*): δ ppm 1.98–1.76 (m, 12H), 1.61–1.40 (m, 24H), 0.95 (t, *J* = 7.2 Hz, 18H). ^{31}P NMR (400 MHz, Chloroform-*d*): δ ppm 0 (s, 2P)

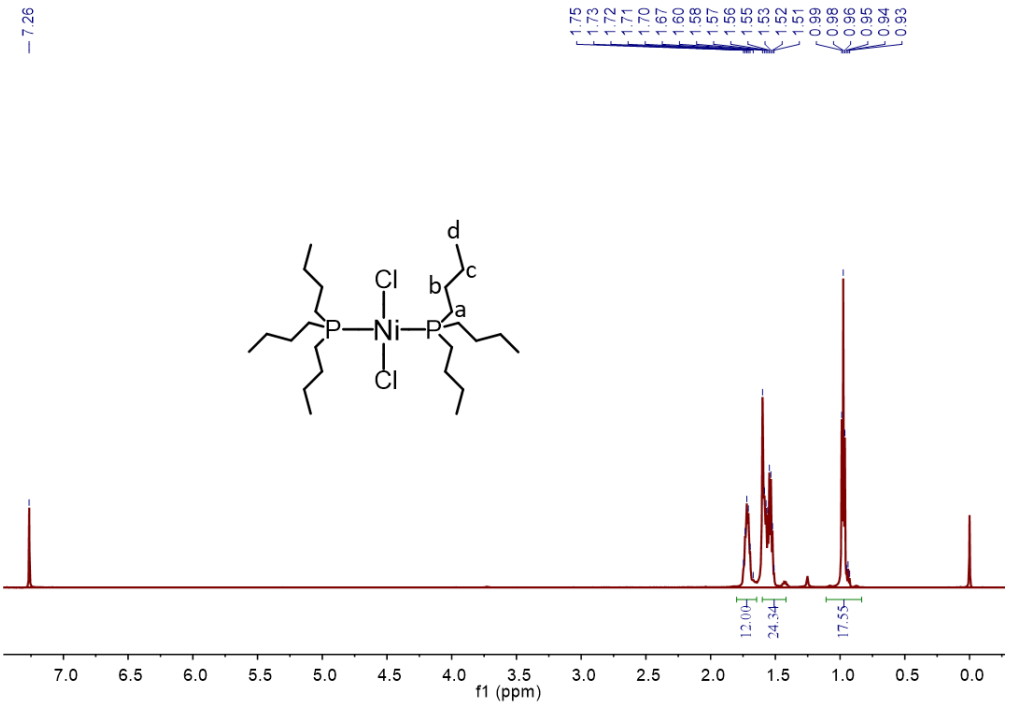

Figure 20 ^{1}H-NMR spectrum of *trans*-Ni(PBu$_3$)$_2$Cl$_2$.

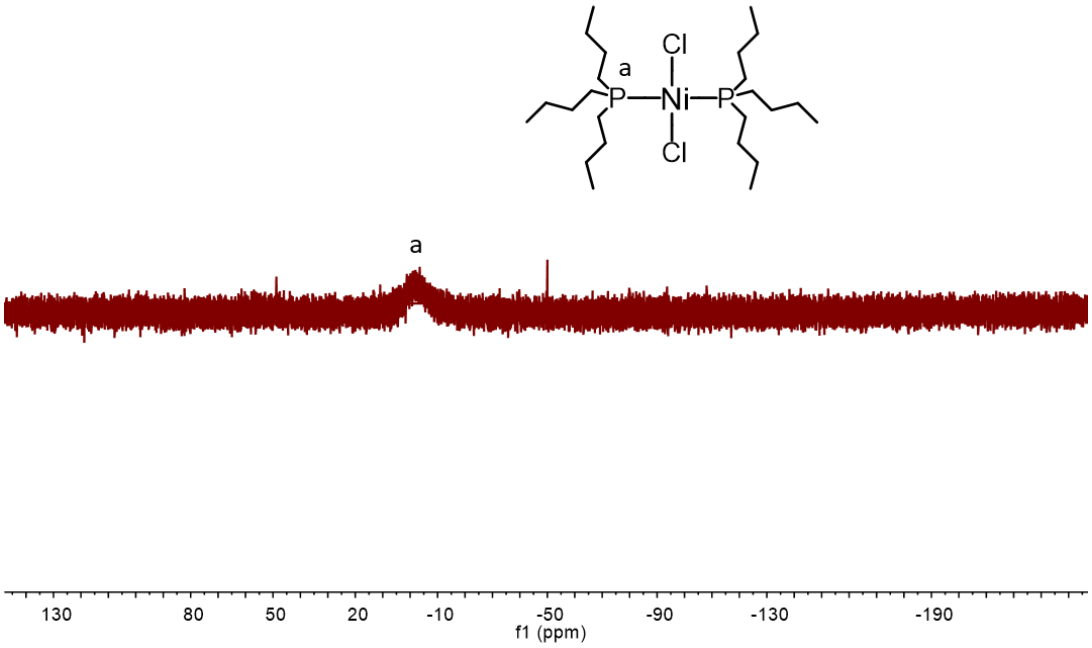

Figure 21 ^{31}P-NMR spectrum of *trans*-Ni(PBu$_3$)$_2$Cl$_2$.

Synthesis of TEPB-Hg-GY:

TEPB-Hg-GY was synthesized via the bottom-up method in the solvent of DCM and MA at RT under a nitrogen atmosphere. To the reactant of $HgCl_2$ in a round bottom flask, 1,3,5-triethynyltriphenylbenzene was added. The mixture was treated by vacuum-nitrogen cycle three times. Then, the mixture was added DCM and MeOH, and then stirred to dissolve the compounds. To this suspension, Et_3N was injected and the reaction the mixture was stirred for 72 h at RT, giving a yellow powder. After the reaction ended, the obtained product was washed by the Soxhlet extractor method with the solvents of DCM, MeOH and THF to remove the unreacted reactants and oligomers. After dring under a reduced pressure, **TEPB-Hg-GY** bulk was obtained as a white powder.

Synthesis of TEPT-Hg-GY:

To the reactant of $HgCl_2$ in a round bottom flask, 2,4,6-tris(4-ethynylphenyl)-1,3,5-triazine was added. Then, DCM and MeOH were added to dissolve the reactants with stirring. To this suspension, Et_3N was injected and the reaction was stirred for 72 h at RT, giving a yellow powder. After the reaction ended, the obtained product was washed by the Soxhlet extractor method with the solvents of DCM, MeOH and THF to remove the unreacted reactants and oligomers. After dring under a reduced pressure, **TEPT-Hg-GY** bulk was obtained as a light-yellow powder.

Synthesis of NH_2-Hg-GY:

To the reactant of $HgCl_2$ in a round bottom flask, 2,4,6-triethynylbenzenamine was added. The mixture was treated by vacuum-nitrogen cycle three times. Then, DCM and MeOH were added to dissolve the reactants with stirring. To this suspension, Et_3N was injected to the mixture and the reaction was stirred for 72 h at RT, giving a yellow powder. After the reaction ended, the liquid was washed with DCM and filtered. Then, the obtained product was washed by the Soxhlet extractor method with the solvents of DCM, MeOH and THF to remove the unreacted reactants and oligomers. After dring under reduced pressure, **NH_2-Hg-GY** bulk was obtained as a yellow powder.

Synthesis of F-Hg-GY:

To the reactant of $HgCl_2$ in a round bottom flask, 1,3,5-triethynyl-2,4,6-trifluoro-benzene was added. The mixture was treated by vacuum-nitrogen cycle three times. Then, DCM and MeOH were added to dissolve the reactants with stirring. To this

suspension was injected Et_3N and the reaction was stirred for 72 h at RT, giving a yellow powder. After the reaction ended, the liquid was washed with DCM and filtered. Then, the obtained product was washed by the Soxhlet extractor method with the solvents of DCM, MeOH and THF to remove the unreacted reactants and oligomers. After dried by a reduced pressure, **F-Hg-GY** bulk was obtained as a white powder.

Synthesis of TEPB-Pt-GY:

TEPB-Pt-GY was synthesized from the ligand of 1,3,5-triethynyltriphenylbenzene via the base-catalyzed dehydrohalogenation reaction. To the reactant of *trans*-$Pt(PBu_3)_2Cl_2$ and CuI in a round bottom flask, 1,3,5-triethynyltriphenylbenzene was added. The mixture was treated by vacuum-nitrogen cycle three times. Then, THF was added to the mixture which was stirred to dissolve the reactants. Et_3N was injected, and the reaction was stirred for 72 h at 40 ℃, giving a yellow powder. After the reaction ended, the powder was washed with DCM three times and filtered. Then the bulk was washed with ACN and THF in a Soxhlet extractor for 24 h, respectively to remove the remaining CuI, Pt-complex, the unreacted ligands, and oligomers totally. After drying under a reduced pressure, **TEPB-Pt-GY** with yield of 90% was obtained.

Synthesis of TEPT-Pt-GY:

TEPT-Pt-GY was synthesized from the ligand of 2,4,6-tris(4-ethynylphenyl)-1,3,5-triazine via the base-catalyzed dehydrohalogenation reaction. To the reactant of *trans*-$Pt(PBu_3)_2Cl_2$ and CuI in a round bottom flask, 2,4,6-tris(4-ethynylphenyl)-1,3,5-triazine was added. The mixture was treated by vacuum-nitrogen cycle three times.

Then, THF was added to the mixture which was stirred to dissolve the reactants. Et_3N was injected, and the reaction was stirred for 72 h at RT, giving a yellow powder. After the reaction ended, the powder was washed with DCM three times and filtered. Then the bulk was washed with ACN and THF in a Soxhlet extractor for 24 h, respectively to remove the remaining CuI, Pt-complex, the unreacted ligands, and oligomers totally. After drying under a reduced pressure, **TEPT-Pt-GY** with yield of 95% was obtained.

Synthesis of F-Pt-GY:

F-Pt-GY was synthesized from the ligands of 1,3,5-triethynyl-2,4,6-trifluoro-benzene via the base-catalyzed dehydrohalogenation reaction. To the reactant of *trans*-$Pt(PBu_3)_2Cl_2$ and CuI in a round bottom flask, 1,3,5-triethynyl-2,4,6-trifluoro-benzene was added. The mixture was treated by vacuum-nitrogen cycle three times. Then, THF was added to the mixture which was stirred to dissolve the reactants. Et_3N was injected, and the reaction was stirred for 72 h at 40 ℃, giving a white powder. After the reaction ended, the powder was washed with DCM three times and filtered. Then the bulk was washed with ACN and THF in a Soxhlet extractor for 24 h, respectively to remove the remaining CuI, Pt-complex, the unreacted ligands, and oligomers totally. After drying under reduced pressure, **F-Pt-GY** with yield of 80% was obtained.

Synthesis of TEPB-Ni-GY:

TEPB-Ni-GY was synthesized from the ligand of 1,3,5-triethynyltriphenylbenzene via the base-catalyzed dehydrohalogenation reaction. To the reactant of *trans*-$Ni(PBu_3)_2Cl_2$ and CuI in a round bottom flask, 1,3,5-triethynyltriphenylbenzene was added. The

mixture was treated by vacuum-nitrogen cycle three times. Then, THF was added to the mixture which was stirred to dissolve the reactants. Et_3N was injected, and the reaction was stirred for 72 h at 40℃, giving a yellow powder. After the reaction ended, the powder was washed with DCM three times and filtered. Then the bulk was washed with ACN and THF in a Soxhlet extractor for 24 h, respectively to remove the remaining CuI, Ni-complex, the unreacted ligands, and oligomers totally. After drying under a reduced pressure, **TEPB-Ni-GY** with yield of 85% was obtained.

Synthesis of TEPT-Ni-GY:

TEPT-Ni-GY was synthesized from the ligand of 2,4,6-tris(4-ethynylphenyl)-1,3,5-triazine via the base-catalyzed dehydrohalogenation reaction. To the reactant of *trans*-$Ni(PBu_3)_2Cl_2$ and CuI in a round bottom flask, 2,4,6-tris(4-ethynylphenyl)-1,3,5-triazine was added. The mixture was treated by vacuum-nitrogen cycle three times. Then, THF was added to the mixture which was stirred to dissolve the reactants. Et_3N was injected, and the reaction was stirred for 72 h at room temperature, giving a brown powder. After the reaction ended, the powder was washed with DCM three times and filtered. Then the bulk was washed with ACN and THF in a Soxhlet extractor for 24 h, respectively to remove the remaining CuI, Pt-complex, the unreacted ligands, and oligomers totally. After drying under a reduced pressure, **TEPT-Ni-GY** with yield of 90% was obtained.

Synthesis of NH_2-Ni-GY:

NH_2-Ni-GY was synthesized from the ligand of 2,4,6-triethynylbenzenamine via the

base-catalyzed dehydrohalogenation reaction. To the reactant of *trans*-$Ni(PBu_3)_2Cl_2$ and CuI in a round bottom flask, 2,4,6-triethynylbenzenamine was added. The mixture was treated by vacuum-nitrogen cycle three times. Then, THF was added to the mixture which was stirred to dissolve the reactants. Et_3N was injected, and the reaction was stirred for 72 h at 40℃, giving a reddish-brown powder. After the reaction ended, the powder was washed with DCM three times and filtered. Then the bulk was washed with ACN and THF in a Soxhlet extractor for 24 h, respectively to remove the remaining CuI, Pt-complex, the unreacted ligands, and oligomers totally. After drying under a reduced pressure, **NH_2-Ni-GY** with yield of 50% was obtained.

Synthesis of F-Ni-GY:

F-Ni-GY was synthesized from the ligand of1,3,5-triethynyl-2,4,6-trifluoro-benzene via the base-catalyzed dehydrohalogenation reaction. To the reactant of *trans*-$Ni(PBu_3)_2Cl_2$ and CuI in a round bottom flask, 1,3,5-triethynyl-2,4,6-trifluoro-benzene was added. The mixture was treated by vacuum-nitrogen cycle three times. Then, THF was added to the mixture which was stirred to dissolve the reactants. Et_3N was injected, and the reaction was stirred for 72 h at 40℃, giving a yellow powder. After the reaction ended, the powder was washed with DCM three times and filtered. Then the bulk was washed with ACN and THF in a Soxhlet extractor for 24 h, respectively to remove the remaining CuI, Pt-complex, the unreacted ligands, and oligomers totally. After drying under a reduced pressure, **F-Ni-GY** with yield of 80% was obtained.

Transient-photocurrent-response (TPR) and electrochemical impedance

spectroscopy (EIS) measurements:

All electrochemical measurements were conducted on a CHI 760E workstation (CH Instruments, Shanghai, China) using the standard three-electrode system, in which sample-modified glass carbon electrode, saturated calomel electrode, and carbon electrode were used as working electrode, reference electrode, and counter electrode respectively. The photo-response performance was obtained at open circuit potential (OCP) in 0.1 M sodium sulfate (Na_2SO_4), where a 300 W Xe-lamp with a 420 nm filter was the light source. Electrochemical impedance spectra (EIS) measurements were carried out in ultrapure water at open circuit potential with a 10^{-2}–10^{6} Hz frequency range.

Mott–Schottky (M–S) plots measurement:

The sample was deposited on the ITO glass substrate by drop-casting. The slurry was prepared by mixing catalyst (1 mg), isopropyl alcohol (0.75 mL), H_2O (0.2 mL), and Nafion solution (50 μL) under ultrasonication. The impedance-potential values for M–S plots were measured in N_2-saturated 0.1 M Na_2SO_4 with Ag/AgCl as the reference electrode and Pt as the counter electrode. The data was collected in the voltage range of –0.8 V to +1.8 V at the frequency of 3, 4, and 5 kHz, respectively.

Determination of apparent quantum yield (AQY):

The apparent quantum efficiency can be evaluated from equation (1):

$$\mathrm{AQY} = \frac{2 \times n_{H_2O_2} \times N_A}{N} \qquad (1)$$

$n_{\mathrm{H_2O_2}}$ is the number of evolved H_2O_2 molecules, N_A is Avogadro number (6.02×10^{23})

and N represents the number of incident photons, which can be calculated from equation (2):

$$N = \frac{\text{light intensity}\left(\text{W cm}^{-2}\right) \times \text{illumination area}\left(cm^2\right)}{\frac{hc}{\lambda}} \quad (2)$$

where h is the Planck constant (6.626×10^{-34} J·s = 4.136×10^{-15} eV·s), c is the speed of light (3.0×10^{8} m·s^{-1}), and λ is the wavelength of light (365, 420, 500, 590 and 660 nm, respectively).

Electron paramagnetic resonance (EPR) measurements:

Spin trapping-EPR tests were recorded using a Bruker EMX plus model spectrometer operating at the X-band frequency (9.4 GHz). 5,5-Dimethyl-1-pyrroline N-oxide (DMPO) was used as a spin-trapping reagent to detect the radicals of •OH or $•O_2^-$. The measurements were conducted as follows: 5 mg of powder was dispersed in 5 ml of DI H_2O or MeOH (DI H_2O for •OH radicals, MeOH for $•O_2^-$ radicals) by ultrasonication for 5 min. A 200 μL of 100 mM DMPO solution was added to 200 μL of the mixture and then thoroughly shaken. After that, the samples were packed into capillaries and put into the sample tubes for testing under dark or light conditions with a time interval of 2, 4, and 6 min, respectively. A Xe lamp ($\lambda > 420$ nm) was used as the light source.

***In-situ* DRIFTS measurements:**

In-situ DRIFTS measurements were performed to confirm active sites using a Nicolet IS50 Fourier transform spectrometer equipped with an integrating sphere. Each spectrum was recorded by averaging 128 scans with 8 cm^{-1} spectral resolution. The samples were held in a photocatalytic diffuse reflectance *in-situ* cell which was

specifically designed for examining highly scattering powder samples. For the ORR pathway, **NH_2-Hg-GY** was illuminated with white light for 30 min after passing O_2 into the reaction cell with deuterated water vapor for 30 min, and IR spectra were collected at 0, 10, 20, and 30 min, respectively during this period. Similarly, for the WOR pathway, the catalyst was illuminated with white light for 30 min after passing argon into the reaction cell with deionized water vapor for 30 min, and IR spectra were collected at 0, 10, 20, and 30 min, respectively during this period.

Femtosecond transient absorption spectroscopy measurement:

Full-spectral-range transient absorption spectroscopy was performed using a custom-built pump-probe setup with a Ti:Sapphire regenerative amplifier (Coherent Legend Elite) seeded by a mode-locked Ti:Sapphire oscillator (Coherent Mira 900) as the light source. The 800-nm, 1 kHz output from the amplifier was divided into two beams: the first, more intense beam, was directed into an optical parametric amplifier (Coherent Opera Solo), generating a tunable photon energy pump beam; the remaining laser power was used for a supercontinuum probe generation. The probe beam traversed a mechanical translation stage, enabling a time delay of up to 2 ns between pump and probe pulses, and then was focused on a crystal plate. A calcium fluoride (CaF_2) plate was used for UV−Vis range supercontinuum (350−700 nm) generation, with the residual fundamental laser line filtered by a 700- nm short-pass filter (Edmund Optics, #69−206). A Vis-NIR supercontinuum (500−1300 nm) was generated by a yttrium aluminium garnet (YAG) plate, with the fundamental laser line filtered by an 800-nm

notch filter (Edmund Optics, #86−127) featuring a 40-nm bandwidth.

Shot-by-shot probe beam transmission in the range of 350−1000 nm was recorded by an Acton Spectrapro 275 spectrometer equipped with a 150 ln mm^{-1} grating and a silicon line CCD (Hamamatsu S8380); a 100 ln mm^{-1} grating and an InGaAs line CCD (Hamamatsu G11620) were used for measurements in the range of 900−1300 nm. The sufficient spectral overlap between CaF_2- and YAG-generated supercontinuum allowed for the stitching of TA spectra in the range of 550−650 nm. The probe beam was focused on a sample at a normal incident angle using a 150 mm lens; The spot size, measured by an optics-free CCD, was 150 μm. The pump beam hit the sample at a 10° incident angle (from the normal); To ensure sufficient spatial overlap with the probe beam, its diameter was limited to 1.5 mm via a pinhole. The differential transmission spectrum of the probe pulse ($\Delta T/T$) was calculated as $((T_{pump\ ON} - T_{pump\ OFF})/T_{pump\ OFF})$. The instrumental response function is 120 fs. Measurements were conducted with the water dispersions of photocatalysts at an excitation flux of 35 μJ cm^{-2}, being a compromise between excitation flux and signal-to-noise ratio. Within the measured excitation wavelength range (320−550 nm), the excited carrier density was approximately 10^{15} cm^{-3}, supporting the assumption of a negligible contribution from multi-excitonic recombination in the collected data.

Photocatalytic H_2O_2 production performance:

The photocatalytic activity of the photocatalysts was assessed by a multichannel photochemical reaction system (PCX-50B, Beijing perfect-light Co., Ltd, China)

equipped with a visible light source (λ ≥ 420 nm). In a typical reaction, 10 mg photocatalyst was dispersed in 15 mL ultrapure water to form a homogeneous suspension. After that, the suspension was irradiated for 4 h under continuous stirring (150 r.p.m.). The time dependence curves of H_2O_2 production were tested under light for 2, 4, 6, 8, 10, 12, and 24 h, respectively. The resulting H_2 was detected by a Gas chromatograph (GC-4000A). The concentration of the produced H_2O_2 was determined by a commercial Hydrogen Peroxide Assay Kit (Titanium sulfate microplate method, Shanghai Yuanye Bio-Technology Co., Ltd).

Fabrication of Pt/PMMA+Pt-GYs/ITO memory device:

First, the sample was dispersed in chlorobenzene, sonicated for 48 h, and mixed evenly with PMMA. The mixture was then spin-coated on the ITO bottom electrode to form a film. Finally, the Pt top electrode was prepared by sputtering.

Photocatalytic CO_2RR:

The photocatalytic activity of the Ni-GYs was conducted with a visible light source (λ ≥ 420 nm). In a typical reaction, 1 mg photocatalyst was dispersed in 5 mL ACN and 1 mL ultrapure water with photosensitizer (PS) of ruthenium terpyridine and electron donor of TEOA to form a homogeneous suspension. After that, the suspension was sonicated for 4 h. The time dependence curves of CO production rate were tested under light for 1, 2, 3, 4, and 5 h, respectively. The resulting CO and H_2 were detected by a Gas chromatograph (GC-4000A).

DFT calculations:

The first-principles calculations were conducted by DFT using the Vienna ab initio simulation package (VASP)[1,2]. The wave functions are constructed as projected augmented wave (PAW) pseudopotentials[3], while the exchange-correlation energies were evaluated by the Perdew-Burke-Ernzerhof (PBE) with generalized gradient approximation (GGA)[4]. The cut-off energy was set to 400 eV, and a self-consistent field (SCF) convergence criterion was set as 10^{-4} eV, which was more than enough for the convergence of the calculations. The DOS calculations were performed by setting ICHARG tag and Monkhorst-Pack K-meshes of 1 × 1 × 1, the analysis of the DOS plots is conducted with the help of vaspkit software[5], where the partial DOS (or projected DOS) plots are computed by projecting each wave function on a specific angular momentum around a specific atom or element.

The slab models with 1 × 1 × 1 supercell were created for the three materials, while a vacuum gap of 15 Å was set in the slab model to prevent its interaction with the periodic conditions. The atoms from 2D materials were set to be free to move in all directions. A K-meshing of 1 × 1 × 1 with the type of centered gamma was used in the calculation of the free energy diagrams of the ORR and WOR steps. The adsorption energy was calculated as the the following equation:

$$E_{ads} = E_{slab+absorbate} - E_{slab} - E_{absorbate} \quad (1)$$

where H_{slab} and $E_{absorbate}$ represent the total energy (enthalpy) of the constructed slab model and absorbate before being absorbed, while the $E_{slab+absorbate}$ is the total energy of the slab model with adsorbate on the surface. Based on this definition, the more

negative value of E_{ads} represents a higher thermodynamic stability of the system. However, the difference of Gibbs free energy would demonstrate the tendency of a reaction more evidentially, which could be acquired by the following equation:

$$\Delta G = E_{ads} - \Delta ZPE - T \bullet \Delta S \qquad (2)$$

where ΔG is the difference of Gibbs free energy, ΔZPE is the difference of zero-point energy, which can be obtained from the vibration frequency calculations, T is the temperature with the unit of the Kelvin unit, and ΔS is the entropy change. The more negative value of ΔG indicates a higher possibility for the reaction to happen.

The geometric structure for the unit of these built models were optimized by DFT at the PBE0/def2SVP level. The electronic density differences between the excited state and the ground state of the unit were calculated using the TD-DFT method under the same level.

References

1. Botana, A. S. & Norman, M. R. Electronic Structure and Magnetism of Transition Metal Dihalides: Bulk to Monolayer. *Phys. Rev. Mater.* **3,** 044001 (2019).
2. Kresse, G. & Furthmu¨ller, J. Efficient Iterative Schemes for ab Initio Total-Energy Calculations using a Plane-Wave Basis Set. *Phys. Rev. B* **54**, 11169–11186 (1996).
3. Chaput, L., Pécheur, P. & Scherrer, H. Thermopower, Hall Tensor, and Relaxation Time Approximation for Elemental Zinc. *Phys. Rev. B* **75,** 045116 (2007).
4. Perdew, J. P., Ruzsinszky, A., Csonka, G. I., Vydrov, O. A., Scuseria, G. E., Constantin, L. A. & Burke, K. Restoring the Density-Gradient Expansion for Exchange in Solids and Surfaces. *Phys. Rev. Lett.* **100**, 136406 (2008).
5. Wang, V., Xu, N., Liu, J., Tang, G. & Geng, W. VASPKIT: A User-Friendly Interface Facilitating High-Throughput Computing and Analysis using VASP Code. *Comput. Phys. Commun.* **267,** 108033 (2021).